

2006-01-04

A Fringe Projection System for Measurement of Condensing Fluid Films in Reduced Gravity

Deepti Tulsiani
Worcester Polytechnic Institute

Follow this and additional works at: <https://digitalcommons.wpi.edu/etd-theses>

Repository Citation

Tulsiani, Deepti, "A Fringe Projection System for Measurement of Condensing Fluid Films in Reduced Gravity" (2006). *Masters Theses (All Theses, All Years)*. 5.
<https://digitalcommons.wpi.edu/etd-theses/5>

This thesis is brought to you for free and open access by Digital WPI. It has been accepted for inclusion in Masters Theses (All Theses, All Years) by an authorized administrator of Digital WPI. For more information, please contact wpi-etd@wpi.edu.

**A Fringe Projection System for Measurement of
Condensing Fluid Films in Reduced Gravity**

by

Deepti Tulsiani

A Thesis

submitted to the faculty of

Worcester Polytechnic Institute

in partial fulfillment of the requirements for the

Degree of Master of Science

in

Electrical Engineering

November 22, 2005

APPROVED:

Prof. Peder C. Pedersen, Advisor

Prof. Brian King, Committee Member

Prof. Fred J. Looft III, Committee Member

Abstract

The thesis describes the design of a fringe projection system to study the dynamics of condensation with potential application in a reduced gravity environment. The desired properties of the system are its simplicity, portability, compact size and robustness to vibration, making it suitable for use in spaceflights. The concept is that an optical system for imaging the condensation layer enables extraction of valuable data from the image because of the ability of the optical system to image the perturbations in the condensation films. By acquiring a sequence of images of the deformed fringe pattern, the change in the surface topology can be observed over time, giving greater understanding of condensation dynamics in reduced gravity.

The principle behind the system is fringe projection, which is a simple way of optically mapping a surface in which fringes are projected onto the object under test in one direction and are viewed from another direction. The projected fringe pattern gets changed in accordance with the surface topology of the object. This change manifests itself in the form of angular and spatial frequency carrier shift in the Fourier domain. Thus the extraction of surface topology of the object becomes a matter of linear frequency domain filtering. The deformed fringe pattern is thus analyzed by a Fourier transform based fringe analysis technique followed by phase unwrapping.

The system hardware setup was developed, and a series of experiments were performed which validate the working of the system. A condensation

chamber was developed and integrated with the system to allow study of condensation. The process of condensation was implemented by cooling the reference copper block by circulating ice cold water through it and by passing water vapor over it in a controlled manner.

The fringe projection system was implemented using laser light, which involved the generation of fringes with the use of a beam splitter and two reference mirrors. The results obtained were promising except for the presence of excessive amount of speckle noise in the images. As an alternative, fringe projection was also implemented using a white light source and a Ronchi ruling. It was found that the fringes obtained from the white light source were of low intensity and contrast and the camera was not sensitive enough to capture images good enough for further analysis. Suggestions have been provided for further improvement of these images as further work.

Acknowledgements

First and foremost, I would like to express my extreme gratitude towards my research advisor Dr. Peder Pedersen, who has been a very encouraging, motivating and understanding advisor. His zeal for excellence and perfection is highly infectious and has helped me bring the project to this level of completion. I would also like to thank Dr. Brian King, who was always around to give technical guidance, point me to helpful resources and help me troubleshoot. I would also like to thank Dr. Cosme Furlong for his continued guidance throughout the project. I am also thankful to Dr. Fred Looft and the Electrical and Computer Engineering department for the help, encouragement and financial support provided to me in pursuit of this research.

I would like to thank Adam Klempler, for helping me with the mechanical design aspects during the initial stages of the project. I would also like to thank Jack Coyne, whose efforts in developing the condensation cell and MATLAB scripts for the controlling the image and temperature capture systems were invaluable and are greatly appreciated. I am also grateful to Ervin Kolenovic for his help with the use of FringeProcessor software and other valuable suggestions.

This project would not have been possible without the ever present support and encouragement from my husband, Bharat. He has been extremely patient, understanding, and loving throughout my numerous research and

thesis writing times. I would also like to thank Aditya, Dalys, Ruben and Carsten for making our lab such a great place to work. Last and certainly not the least, I wish to thank my family for their love and guidance and my friends for always being there. I would like to dedicate this thesis to the loving memory of my father who would have been very proud to see me reach this goal.

TABLE OF CONTENTS

ABSTRACT	II
ACKNOWLEDGEMENTS	IV
TABLE OF CONTENTS	VI
TABLE OF FIGURES	IX
TABLE OF TABLES	XII
CHAPTER 1: INTRODUCTION	1
1.1 BACKGROUND FOR CONDENSATION.....	1
1.2 CONDENSATION MEASUREMENT TECHNIQUES.....	2
1.3 SUMMARY OF ULTRASOUND TECHNIQUE.....	3
1.4 DEVELOPMENT STAGES OF THE PROPOSED MEASUREMENT SYSTEM.....	7
1.5 KC135 FLIGHT EXPERIMENT REQUIREMENTS.....	8
1.6 THESIS GOALS	9
1.7 THESIS OUTLINE.....	9
CHAPTER 2: OPTICAL METROLOGY THEORY	11
2.1 INTRODUCTION.....	11
2.2 THEORY OF OPTICAL INTERFERENCE	12
2.3 INTERFERENCE BASED MEASUREMENT TECHNIQUES	18
2.3.1 Phase Shifting Interferometry	18
2.3.2 Moiré Interferometry.....	21
2.4 PROJECTION BASED MEASUREMENT TECHNIQUES.....	25
2.4.1 Fringe Projection with Coherent Light.....	25
2.4.2 Fringe Projection with Incoherent Light.....	30

2.5 SELECTION OF TECHNIQUE	32
2.6 THEORETICAL ANALYSIS PROCEDURE	32
CHAPTER 3: HARDWARE SYSTEM SETUP	40
3.1 OVERALL SYSTEM DESCRIPTION	40
3.2 HARDWARE COMPONENTS	41
3.2.1 Coherent Light Fringe Projection System	43
i. Laser.....	47
ii. Collimator	49
iii. Michelson Interferometer	50
iv. Beam expander arrangement.....	53
v. Beam steering mirrors	55
vi. Camera.....	58
vii. Camera lens	64
viii. Frame Grabber	68
3.2.2 Incoherent Light Fringe Projection System	71
i. White light source	72
ii. Ronchi ruling.....	75
iii. Beam expander	76
iv. Beam steering mirrors	76
v. Camera.....	76
vi. Camera lens	76
vii. Frame grabber.....	76
3.3 CONDENSATION CELL.....	76
CHAPTER 4: SOFTWARE.....	82
4.1 DATA CAPTURE SOFTWARE	82
4.1.1 Main Control script.....	85
4.1.2 Temperature Sensor Interface	88
4.1.3 Frame Capture Script.....	89

4.1.4 Frame Grabber Interface	90
4.2 ANALYSIS SOFTWARE	91
4.2.1 Signal Processing Steps	91
4.2.2 FringeProcessor.....	93
CHAPTER 5: EXPERIMENTAL WORK AND RESULTS	97
5.1 NON-FLUID EXPERIMENTS	97
5.2 STATIONARY FLUID EXPERIMENTS	110
5.3 CONDENSATION EXPERIMENTS	116
CHAPTER 6: CONCLUSION	120
6.1 FRINGE PROJECTION BASED MEASUREMENT SYSTEM.....	120
6.2 SUGGESTIONS AND FURTHER WORK.....	120
REFERENCES	123
BIBLIOGRAPHY	125
APPENDIX A: INTERFERENCE EQUATIONS	127
APPENDIX B: ASSEMBLY OF THE SYSTEM.....	131
APPENDIX C: MATLAB CODE	141

TABLE OF FIGURES

FIGURE 1-1: A BLOCK DIAGRAM OF THE ULTRASONIC THICKNESS MEASUREMENT SYSTEM	4
FIGURE 2-1: YOUNG'S DOUBLE SLIT EXPERIMENT	15
FIGURE 2-2: BASIC PRINCIPLE OF MICHELSON AND TWYMAN INTERFEROMETERS	16
FIGURE 2-3: MICHELSON INTERFEROMETER WITH AN EXTENDED SOURCE.....	17
FIGURE 2-4: THE TWYMAN-GREEN INTERFEROMETER, AS USED TO TEST A PRISM.....	18
FIGURE 2-5: PHASE SHIFTING INTERFEROMETER USING A MOVING MIRROR.....	19
FIGURE 2-6: SUPERPOSITION OF PERIODIC BLACK AND WHITE IMAGES	22
FIGURE 2-7: ANALYSIS OF FRINGES WITH FRINGE SPACING P PROJECTED AT AN ANGLE α ON THE SURFACE UNDER TEST.....	27
FIGURE 2-8: FRINGE PROJECTION USING A COHERENT LIGHT SOURCE.....	28
FIGURE 2-9: FRINGE PROJECTION USING AN INCOHERENT LIGHT SOURCE.....	30
FIGURE 2-10: RONCHI RULING	31
FIGURE 2-11: (A) THROUGH (I) - FILTERING AND WINDOWING PROCESS.....	38
FIGURE 3-1: FRINGE PROJECTION SYSTEM SETUP	41
FIGURE 3-2: BASIC FRINGE PROJECTION SYSTEM BLOCK DIAGRAM.....	42
FIGURE 3-3: BLOCK DIAGRAM OF COHERENT LIGHT FRINGE PROJECTION SYSTEM	44
FIGURE 3-4: COHERENT LIGHT FRINGE PROJECTION SYSTEM SETUP	46
FIGURE 3-5: 4F IMAGING SOLUTION	54
FIGURE 3-6: SPECIFICATIONS OF ANGLE MOUNT FOR BEAM STEERING MIRROR	57
FIGURE 3-7: PICTURE OF ANGLE MOUNT FOR BEAM STEERING MIRROR.....	58
FIGURE 3-8: RIGHT ANGLE ANALOG CCD CAMERA (COURTESY SONY)	59
FIGURE 3-9: SPECIFICATIONS OF THE CAMERA MOUNT	61
FIGURE 3-10: CUSTOM DESIGNED CAMERA MOUNT	62

FIGURE 3-11: REAR PANEL OF DC 700 ADAPTER (COURTESY SONY)	63
FIGURE 3-12: 12-PIN CAMERA CONNECTOR (COURTESY SONY)	64
FIGURE 3-13: SENSOR SIZE OF A 1/2" CCD.....	65
FIGURE 3-14: CAMERA LENS AND SPACER PLACEMENT	66
FIGURE 3-15: PCMCIA FRAME GRABBER (COURTESY IMPERX).....	69
FIGURE 3-16: INCOHERENT LIGHT FRINGE PROJECTION SYSTEM	71
FIGURE 3-17: LED BASED WHITE LIGHT SOURCE.....	73
FIGURE 3-18: CONDENSATION CHAMBER.....	78
FIGURE 3-19: SCHEMATIC OF THE CONDENSATION CELL.....	80
FIGURE 3-20: INTEGRATION OF THE CONDENSATION CELL WITH THE OPTICAL SYSTEM.....	81
FIGURE 4-1: BLOCK DIAGRAM OF DATA CAPTURE SOFTWARE	84
FIGURE 4-2: GRAPHICAL USER INTERFACE DISPLAYED BY THE CONTROL SCRIPT	85
FIGURE 4-3: FLOWCHART OF THE MATLAB SCRIPT <i>FCAP.M</i>	86
FIGURE 4-4: APPLICATION INTERFACE OF THE FRINGEPROCESSOR	95
FIGURE 5-1: FRINGE PATTERN ON REFERENCE COPPER SURFACE.....	98
FIGURE 5-2: DEFORMED FRINGE PATTERN WITH A METAL WASHER ON THE COPPER SURFACE ...	98
FIGURE 5-3: DEFORMED FRINGE PATTERN WITH A PENNY ON THE COPPER SURFACE.....	99
FIGURE 5-4: DEFORMED FRINGE PATTERN WITH A GLASS SLIDE ON THE COPPER SURFACE	99
FIGURE 5-5: WRAPPED PHASE FOR REFERENCE COPPER SURFACE.....	100
FIGURE 5-6: WRAPPED PHASE FOR THE METAL WASHER ON THE COPPER SURFACE	101
FIGURE 5-7: WRAPPED PHASE FOR THE PENNY ON THE COPPER SURFACE	102
FIGURE 5-8: WRAPPED PHASE FOR THE GLASS SLIDE ON THE COPPER SURFACE	103
FIGURE 5-9: UNWRAPPED PHASE FOR THE METAL WASHER ON THE COPPER SURFACE	104
FIGURE 5-10: SURFACE TOPOLOGY OF THE METAL WASHER ON THE COPPER SURFACE.....	105
FIGURE 5-11: CLOSE-UP VIEW OF SURFACE TOPOLOGY OF THE METAL WASHER	105
FIGURE 5-12: UNWRAPPED PHASE FOR THE PENNY ON THE COPPER SURFACE	106

FIGURE 5-13: SURFACE TOPOLOGY OF THE PENNY ON THE COPPER SURFACE	107
FIGURE 5-14: CLOSE-UP VIEW OF SURFACE TOPOLOGY OF THE PENNY.....	107
FIGURE 5-15: UNWRAPPED PHASE FOR THE GLASS SLIDE ON THE COPPER SURFACE	108
FIGURE 5-16: SURFACE TOPOLOGY OF THE GLASS SLIDE ON THE COPPER SURFACE	109
FIGURE 5-17: CLOSE-UP VIEW OF SURFACE TOPOLOGY OF THE GLASS SLIDE.....	109
FIGURE 5-18: FRINGE PATTERN ON REFERENCE COPPER SURFACE.....	110
FIGURE 5-19: DEFORMED FRINGE PATTERN WITH A WATER DROPLET ON COPPER SURFACE	111
FIGURE 5-20: WRAPPED PHASE FOR REFERENCE COPPER SURFACE.....	112
FIGURE 5-21: WRAPPED PHASE FOR THE WATER DROPLET ON THE COPPER SURFACE	113
FIGURE 5-22: UNWRAPPED PHASE FOR THE WATER DROPLET ON THE COPPER SURFACE	114
FIGURE 5-23: SURFACE TOPOLOGY OF THE WATER DROPLET ON THE COPPER SURFACE	115
FIGURE 5-24: CLOSE-UP VIEW OF SURFACE TOPOLOGY OF THE WATER DROPLET.....	115
FIGURE 5-25: DISTORTION IN FRINGE PATTERN DUE TO CONDENSATION CELL.....	116
FIGURE 5-26: CONDENSATION ON WALLS AND CEILING OF THE CHAMBER	118
FIGURE 5-27: INITIAL SNAPSHOT OF PROGRESSING CONDENSATION.....	119
FIGURE 5-28: SNAPSHOT OF CONDENSING FILM AT A LATER STAGE	119

TABLE OF TABLES

TABLE 3-1: SPECIFICATIONS OF THE LASER	49
TABLE 3-2: SPECIFICATIONS OF THE COLLIMATOR	50
TABLE 3-3: SPECIFICATIONS OF THE BEAM SPLITTER	52
TABLE 3-4: SPECIFICATIONS OF THE REFERENCE MIRRORS	53
TABLE 3-5: SPECIFICATIONS OF THE BEAM EXPANSION LENSES.....	55
TABLE 3-6: SPECIFICATIONS OF THE BEAM STEERING MIRRORS	56
TABLE 3-7: SPECIFICATIONS OF THE CAMERA	60
TABLE 3-8: SPECIFICATIONS OF THE CAMERA ADAPTER	63
TABLE 3-9: SPECIFICATIONS OF THE CAMERA LENS	68
TABLE 3-10: SPECIFICATIONS OF THE FRAME GRABBER.....	70
TABLE 3-11: SPECIFICATIONS OF THE LUXEON LED.....	74
TABLE 3-12: SPECIFICATIONS OF THE RONCHI RULING	75

Chapter 1: Introduction

1.1 Background for condensation

The subject of this thesis is an optical measurement system for characterizing the dynamics of condensation in reduced gravity. Thus, we begin with a description of the process of condensation.

Condensation is the physical process of converting vapor to a liquid. In the process, molecules give up some energy in the form of heat. The reverse happens with evaporation, where the molecules take away heat when they evaporate. At a liquid-vapor interface, molecules are constantly entering the liquid state from the vapor and others are going from the liquid to the vapor. When there is greater number of molecules going from the vapor to liquid state, rather than the reverse, then condensation is said to be occurring [1]. For example, when water vapor from the air condenses onto a glass of cold water, heat is transmitted due to the phase change, through the glass into cold water.

The need for development of techniques to measure condensation in low gravity environments arises from the fact that the phenomenon of condensation on a cooled metal surface is a complex one, with different behavior in the case of reduced gravity. Condensation is affected by parameters such as temperature and pressure of the vapor, the condensing surface, and the

viscosity and thermal conductivity of the condensate etc. The mechanisms of conduction and convection also play a role in the condensation process, of which convection is a gravity driven process. Thus, in reduced gravity environments, condensation rates would be significantly altered.

1.2 Condensation Measurement Techniques

Several techniques for measurement of condensation are possible, and the ones most appropriate for the current project are briefly described here.

One technique for measuring condensation is in the form of an ultrasonic system. The ultrasound system, implemented previously as part of this project, and described in a M.S. thesis by Michael Shear, uses several transducers in pulse-echo mode, to determine the thickness of the fluid film at discrete locations opposite each transducer [1]. The next section explains this technique in more detail. This system was found to yield thickness and growth rate information, but only limited topographic information about the condensing fluid film. This limitation is due to the fact that information about the condensate is available only at discrete points.

A second approach to condensation measurement utilizes heat flux measurements; if the temperature of the vapor is known, and the temperature of the block onto which the vapor is condensing is known, the amount of fluid condensing can be calculated from the total heat flux of the system. This

measures the condensation rate, but provides no information about the topology of the fluid film or about the film thickness at any given time.

Another simple approach can be to simply capture the growth and spatial distribution of the condensing fluid film as a video stream. However, this would yield only qualitative rather than quantitative information.

The fourth measurement approach for monitoring the progress of condensation is an optical system, in which the condensate layer is illuminated with a fringe pattern and the reflections off of the fluid layer are recorded with a CCD camera. This system measures the topology of the fluid layer as well as its thickness and growth rate, over the entire area of interest. This measurement approach is the one we chose to implement, and will be described in greater detail in later chapters.

1.3 Summary of Ultrasound technique

The pulse-echo ultrasonic system measured the thickness of a condensing film in real time, as well as processed the data to determine wave velocity and wavelength data for perturbations within the condensing film. This was done using several ultrasound transducers mounted on the outside surface of the condensation chamber [1].

This research was conducted using a condensation test cell. A similar condensation cell has been utilized for the current research, designed specifically for use with the optical system. The condensation cell used in the

ultrasonic system consisted of a cylindrical shell constructed of relatively insulating plastic, with fittings for introducing vapor into the test cell. The cell was made of copper with cooling channels piped through it. Following is a description of the ultrasonic system from Michael Shear's Master of Science thesis [1] along with a block diagram of the system.

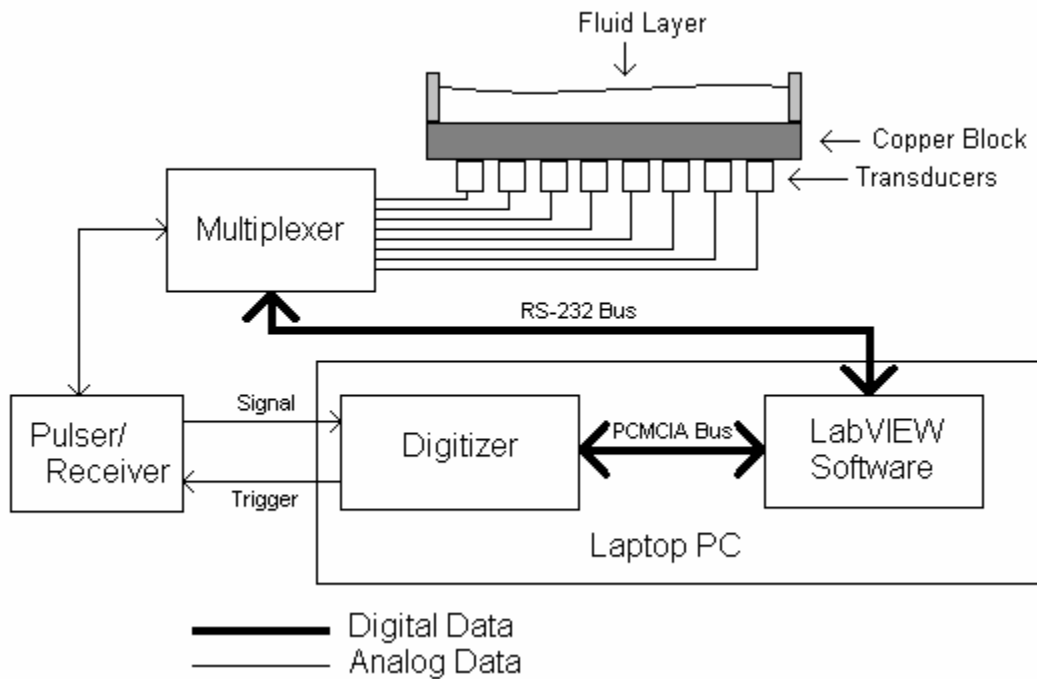


Figure 1-1: A block diagram of the ultrasonic thickness measurement system

“Eight ultrasonic transducers were connected through a multiplexer to a pulser-receiver (P/R) unit, which was connected to a computer-based oscilloscope. The oscilloscope hardware was contained within a single Type II PCMCIA card. The oscilloscope was controlled through a control program which performed all processing as well as all control of the multiplexer. The data from the P/R unit was processed through several signal-processing steps,

and the thickness estimate was extracted from this data. This process was repeated for each of the active transducers and could be continuously repeated to generate a thickness vs. time record.

Condensate layers, which are thin relative to the wavelength of the ultrasonic signal, have the frequency response of a “comb filter”; in other words, the reflected energy due to a broadband ultrasound pulse falls in certain narrowband frequency ranges. The center frequencies of the passbands of the comb filter fulfill the equation $(2n+1) f_0$ where n is an integer greater than or equal to zero and:

$$f_0 = \frac{c}{4d} \quad (1.1)$$

or, equivalently,

$$d = \frac{c}{4f_0} \quad (1.2)$$

where d is the thickness of the fluid layer in meters and c is the speed of sound in the fluid in meters/second.

The f_0 value was extracted through Fourier analysis of the signals acquired by the system. If the fluid layer was of an appropriate thickness for this technique to work (approximately 50-2000 microns) the FFT obtained clear peaks at odd multiples of f_0 ($f_0, 3 f_0, 5 f_0, 7 f_0$, etc.) and the locations of these

peaks were extracted using a peak-detection algorithm which produced an estimated f_0 and through Eqn. 1.2, the estimated layer thickness was obtained.

For thicker layers, a more conventional echo-delay method was used. In this method, the interval between the arrival time of the echo from the copper-fluid interface and the arrival time of the echo from the fluid-vapor interface was measured which yielded a thickness estimate using Eqn. 1.3.

$$d = \frac{c * t}{2} \quad (1.3)$$

This method worked for layers, which were at least one or two wavelengths thick. For the 5MHz center frequency transducers used, this meant that the method was more useful for fluid layers with a thickness of about 0.5mm or greater. The system used the thick-film algorithm first, and if an invalid result or results less than 750 microns were generated, the thin-film algorithm was then run with the same data.”

To overcome the limitations of the ultrasonic system in measuring full field data about condensation and its inability to provide any surface topology information, the proposed optical measurement system was envisioned and developed.

1.4 Development Stages of the Proposed Measurement System

The system developed for the current project is intended to be used for condensation studies in spaceflight experiments. The system needs to be in a form suitable for performing condensation research on NASA's KC-135 aircraft which provides approximately 25 second periods of reduced gravity environment through parabolic trajectory maneuvers.

To monitor condensation in these reduced gravity environments, the proposed optical measurement system with the condensation test cell must be developed. This process was started with the development of the optical measurement system. The system was initially based on the principle of interferometry and fringe skeletonization [2], but later changed to the principle of fringe projection and Fourier transform based fringe analysis. This change became necessary as the maximum thickness of fluid film that can be measured with interferometry and fringe skeletonization was found to be limited to the range of few micrometers. The fringe projection system allows measurement of fluid layers up to many millimeters. This system was initially tested with objects of known dimensions. This helped us validate the working of the system while also bringing out some minor flaws. After making corrective improvements, the experiments were then repeated with static fluid films. The results of these tests showed excessive amount of noise in the reconstructed surface information. This led to investigation of an alternate implementation of the fringe projection system with an incoherent light source. This differed from

the coherent light system in the choice of light source (an LED) and in the mechanism of generation of fringes, which was done using a Ronchi ruling. However, it was found that the fringes obtained from the white light source were of low intensity and contrast and the camera was not sensitive enough to capture images good enough for further analysis.

Soon after the development of the optical system, the condensation test cell was developed and was integrated with the system to perform bench top condensation experiments. The system was found to be successful in reproducing the process of condensation in the cell. However, some problems discussed in detail in the following chapters prevented us from obtaining useful optical data in this process.

1.5 KC135 Flight Experiment Requirements

Since the proposed optical system is intended for use in KC-135 aircrafts, it was important that the system be portable, lightweight and able to withstand vibration. In addition, care was taken to keep the dimensions of the system minimal, which will be useful while packaging the system for the flight experiments. The development of the system was done with these basic criteria always in mind. This had an important influence on the choice of technique for surface metrology. This is explained in greater detail in Chapter 2. Additionally, the individual components used to assemble the final system were selected to

be lightweight, yet capable of being secured firmly in place to minimize effects of vibration.

1.6 Thesis Goals

The goal of this research is the development of an optical system for dynamic measurement and monitoring of condensation film thickness and surface profile. The ultimate goal is to develop a system which can be used to study the process of condensation in reduced gravity environments. The current status of the project is that the system has been implemented and tested with static fluid films. Research was done to improve the quality of results by identifying and minimizing the major sources of noise. An alternate implementation was also proposed and investigated to remove the biggest source of noise, by switching to incoherent light. Testing has been done with quantifiable non-fluid objects and static fluid films of varying thicknesses and profiles. Tests with the condensation test cell were attempted, but were not able to yield useful data due to equipment problems listed further in the thesis.

1.7 Thesis Outline

The structure of the thesis is as follows:

Chapter 1 presents a brief introduction to this thesis and the research project of which it is a part. A background of the theory of condensation and the

motivation for this project is described. A summary of the previous work done as part of this research project is also presented.

Chapter 2 delves into the fundamental optical metrology theory relevant to the understanding of this thesis. Contemporary techniques in the field of surface measurement have been discussed and the reasoning behind the selection of the technique is explained.

In Chapter 3, the complete description of the hardware comprising the system is presented. This includes the optical equipment as well as the construction of the condensation cell.

Chapter 4 begins with an explanation of the signal processing steps involved in the analysis, followed by the available software solutions meeting the requirements. The chapter ends with the evaluation of the selected software.

Detailed descriptions of various experiments performed and results obtained with the setup are provided in Chapter 5. This includes non-fluid, stationary fluid as well as condensation experiments.

Finally, Chapter 6 concludes the thesis with a discussion of the goals achieved and provides direction for further research.

Chapter 2: Optical Metrology Theory

2.1 Introduction

In the field of non-destructive testing and analysis, optical metrology plays a very important role. Optical inspection techniques make it possible to obtain important visual information under difficult conditions such as boilers or in sensitive environments [3]. These techniques can be categorized into two main areas on the basis of the type of measurement. The first category includes techniques, which provide information on the shape or structure of the test object while the other category includes techniques that analyze properties of the object other than its shape [3]. Some examples of applications in the first category are surface roughness measurements, inspection and measurement of wafer surface during VLSI manufacturing and shape recognition. The second category supports applications that go beyond plain visual inspection, such as material characterization, coating evaluation, detection of overheated components [3].

Further sections in this chapter will cover some of the techniques used for surface inspection. Techniques such as phase shifting interferometry, moiré methods, and fringe projection are some of the techniques widely used in

optical metrology. Before explaining these techniques in detail, a review of the theory of optical interference will be covered.

2.2 Theory of Optical Interference

Principle of Coherence: If light originating from a source is divided into two beams, then the inherent fluctuations in the two beams are in general correlated, and the beams are said to be completely or partially coherent depending on whether full or partial correlation exists. In light beams from two independent sources, the phase functions are usually uncorrelated and such beams are called incoherent beams. When coherent waves superpose, they produce visible interference effects because their amplitudes can combine, whereas for the incoherent waves, their intensities combine. Interference produced by incoherent waves varies too rapidly in time to be practically observed.

When two mutually coherent beams pass through a point, we can observe the phenomena of interference between the wavefronts. The medium at that point is subjected to the total effect of the superposition of the two vibrations, and under certain conditions, this superposition results in stationary waves, known as interference fringes.

Consider the superposition of two monochromatic plane waves $U_1(\vec{r})$ and $U_2(\vec{r})$ of the same frequency and with different complex amplitudes. The result is

a monochromatic wave of the same frequency and the complex amplitude is the sum of the individual amplitudes, i.e.

$$U(\vec{r}) = U_1(\vec{r}) + U_2(\vec{r}) \quad (2.1)$$

Expressing the plane waves in terms of their intensities, we get

$$I_1 = |U_1|^2 \quad (2.2)$$

$$I_2 = |U_2|^2 \quad (2.3)$$

Thus, we have,

$$I = |U|^2 = |U_1 + U_2|^2 = |U_1|^2 + |U_2|^2 + U_1 U_2^* + U_1^* U_2 \quad (2.4)$$

where the asterisk denotes complex conjugation.

If

$$U_1 = \sqrt{I_1} e^{j\varphi_1} \quad (2.5)$$

$$U_2 = \sqrt{I_2} e^{j\varphi_2} \quad (2.6)$$

then,

$$I = I_1 + I_2 + 2\sqrt{I_1 I_2} \cos \varphi \quad (2.7)$$

where

$$\varphi = \varphi_1 - \varphi_2 \quad (2.8)$$

Eqn. 2.7 is known as the interference equation, and the term $2\sqrt{I_1 I_2} \cos \varphi$ is known as the interference term. At different points in space, the resultant irradiance can be greater, less than or equal to $I_1 + I_2$, depending on the value of the interference term, i.e. depending on φ . Irradiance maxima occur for $\varphi = 2\pi m$ and minima occur for $\varphi = (2m + 1)\pi$. The dark and light zones that would be seen on a screen placed in the region of interference are known as interference fringes.

An interferometer is, in the broadest sense, a device that generates interference fringes. Interferometers can basically be classified into two types: wavefront splitting interferometers and amplitude splitting interferometers.

Wavefront splitting interferometers recombine two different parts of a wavefront to produce fringes. The earliest experimental arrangement for demonstrating the interference of light was Young's experiment, which employed a double slit to obtain two sources of light. The principle of double slit experiment is illustrated in Figure 2-1.

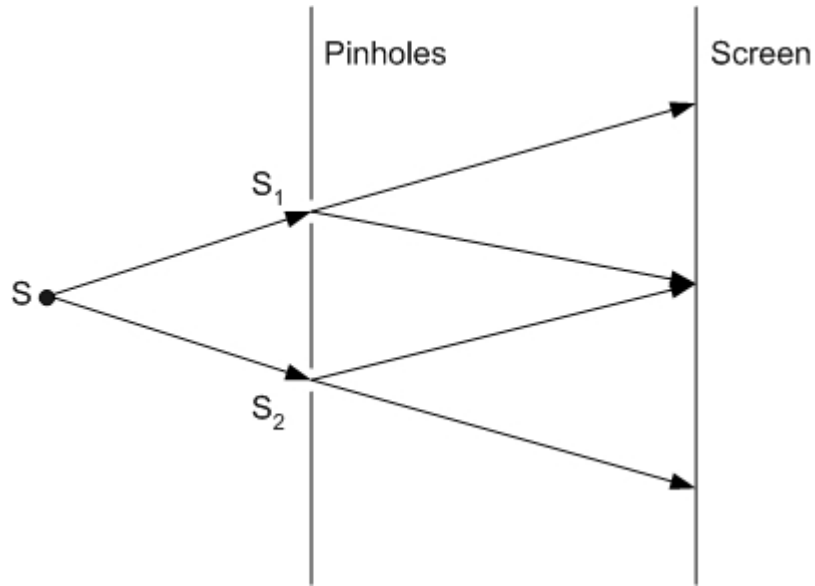


Figure 2-1: Young's double slit Experiment

The light from a monochromatic source S falls on the two pinholes S_1 and S_2 , which are close together and equidistant from S . The pinholes act as secondary monochromatic sources, which are in phase when $SS_1=SS_2$, and the beams from these sources are superposed in the region beyond the pinholes. An interference pattern can be observed on the screen.

Amplitude-splitting interferometers, on the other hand, divide a wavefront into two beams (splitting the amplitude), which propagate through separate paths and are then recombined. Typically, beam splitters are used for splitting and recombining wavefront amplitudes.

One of the most important interferometers based on amplitude-splitting technique is the Michelson's interferometer. Its basic arrangement is shown in Figure 2-2.

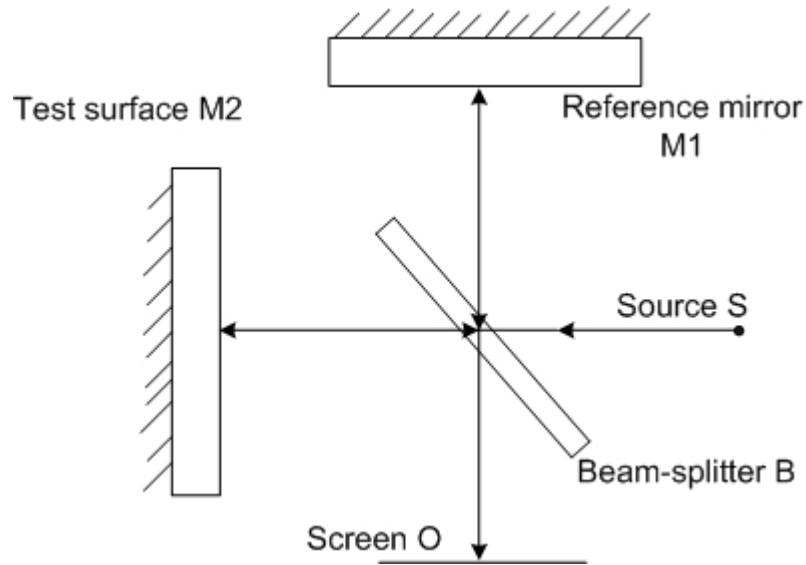


Figure 2-2: Basic Principle of Michelson and Twyman Interferometers

It consists of a partially silvered mirror B, which acts as a beam splitter, dividing the incident beam coming from S into two beams of equal intensity, one reflected and the other transmitted. These beams strike the reference mirror M1 and the test surface M2 at normal incidence and are reflected back and meet at the beam splitter and combine to create interference patterns, which can be seen at the point of observation O.

In Figure 2-2, the interferometer is set up with a point source, which would illuminate only a small part of the field of view. Hence this configuration is used only after further modification. If an extended source (a source with uniform surface brightness) is used in Michelson's mirror arrangement, the form is as shown in Figure 2-3. In this arrangement utilizing an extended source, the rays, which reach the point of observation, leave the mirrors at various angles.

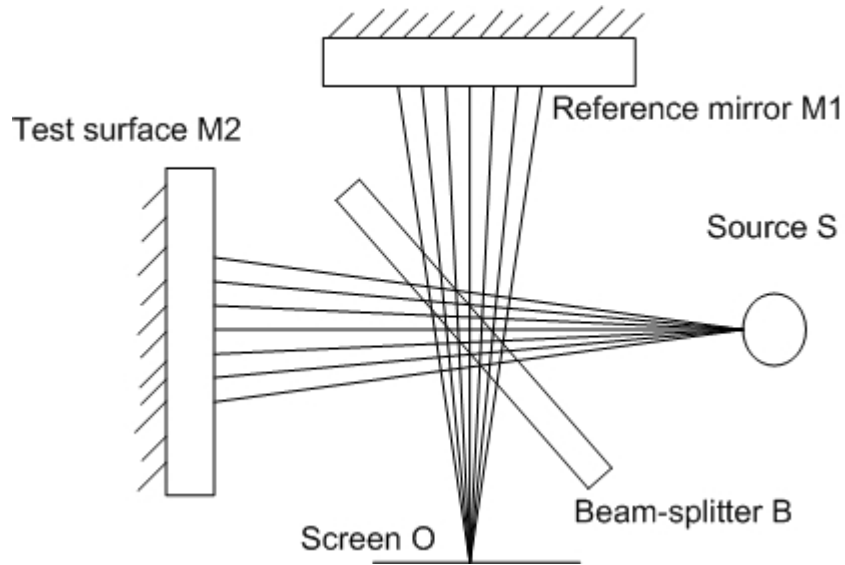


Figure 2-3: Michelson interferometer with an extended source

A Michelson's interferometer modified to work in collimated light is a Twyman-Green interferometer. In the Twyman-Green interferometer, a point source is placed at the focus of a high quality lens so that a plane wave front traverses the mirror system. On reaching the second lens, the wave front is again made spherical and converges on the observation screen. The Twyman-Green interferometer is shown in Figure 2-4. In its simplest form, it can be used to test plane mirrors, plane-parallel windows, or prisms. Figure 2-4 illustrates its use in testing of a prism.

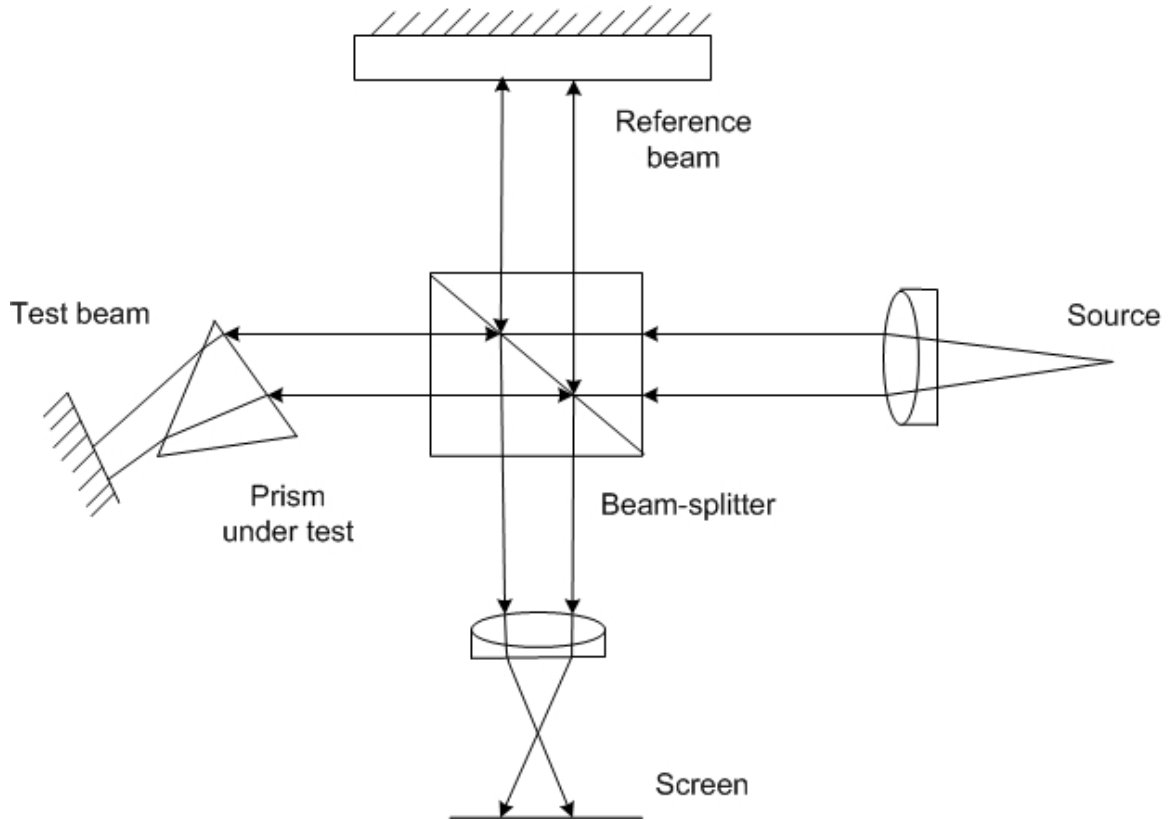


Figure 2-4: The Twyman-Green interferometer, as used to test a prism

2.3 Interference based Measurement Techniques

2.3.1 Phase Shifting Interferometry

The various interferometers discussed above essentially consist of one reference mirror and a second surface, which is the surface under test. The reflections from both these surfaces interfere to generate fringes, which are analyzed to extract information about the surface under test.

The key concept of phase shifting interferometry is that a relative phase shift is introduced between the object and reference beams, typically by varying

the path length, to perform the measurement. By measuring the interferogram intensity while changing the phase between the two beams, the phase of the test wavefront can be determined [4]. Figure 2-5 shows a common setup used in phase shifting interferometry. In this interferometer, a piezo-electric element has been attached to the reference mirror. When the element receives an electric signal from the controller, it is converted to corresponding movement of the element and hence the reference mirror. This induces a phase shift between the two paths. A phase shift can be induced in an interferometer by moving a mirror, tilting a glass plate, moving a grating, rotating a half-wave plate or using a Zeeman laser. These methods effectively shift the frequency of one beam in the interferometer with respect to the other, which introduces a phase difference between the two beams [4].

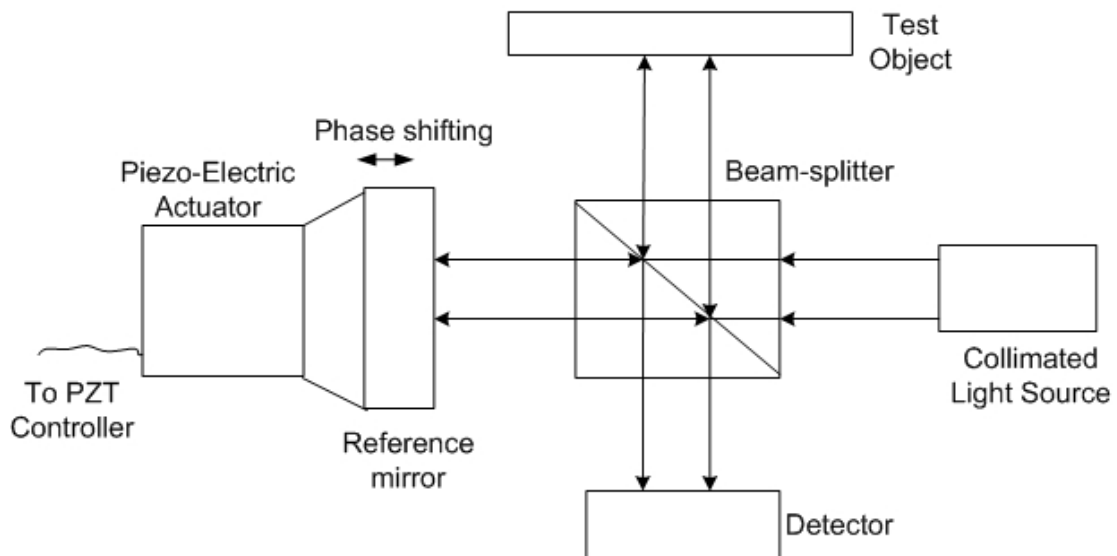


Figure 2-5: Phase shifting interferometer using a moving mirror

Many different algorithms are based on the concept of phase-shifting interferometry. Some of the popular algorithms are the three-step method, four-step method and Carré technique [5]. From Eqn. 2.7, we can say that minimum three sets of recorded fringe data are needed to reconstruct the test wavefront and solve for the three unknowns. In the three-step technique, three intensity measurements are taken with phase shifts of $\frac{\pi}{2}$ between each exposure.

These three measurements at a single point in the interferogram are as below:

$$I_A = I_1 + I_2 + 2\sqrt{I_1 I_2} \cos\left(\varphi + \frac{\pi}{4}\right) \quad (2.9)$$

$$I_B = I_1 + I_2 + 2\sqrt{I_1 I_2} \cos\left(\varphi + \frac{3\pi}{4}\right) \quad (2.10)$$

$$I_C = I_1 + I_2 + 2\sqrt{I_1 I_2} \cos\left(\varphi + \frac{5\pi}{4}\right) \quad (2.11)$$

The phase at each such point can then be found as

$$\phi = \tan^{-1}\left(\frac{I_C - I_B}{I_A - I_B}\right) \quad (2.12)$$

Similarly, the four-step technique works on four phase shift measurements. The Carré technique differs from these two techniques in that the amount of phase shift does not need to be calibrated.

Phase shifting interferometry is one of the most widely used techniques in optical metrology because of its numerous advantages. This technique provides high measurement accuracy and good results even in case of low contrast fringes. However, the biggest disadvantage of this technique is its high susceptibility to vibration, as vibration can cause incorrect phase shifts between

data sets. Also, the presence of the PZT controller increases the cost of this solution significantly.

2.3.2 Moiré Interferometry

The basic concept behind Moiré interferometry is the Moiré effect. Moiré effect is the phenomenon that occurs when periodic structures are superposed or viewed against each other [6]. It consists of a new pattern of alternating dark and bright areas. This effect occurs due to an interaction between the overlaid structures. It results from the geometric distribution of dark and bright areas in the superposition.

Among the various mathematical approaches to study the Moiré phenomenon, one of the best is the spectral approach, which is based on Fourier theory. This approach enables us to analyze properties not only in the original layers and in their superposition, but also in their spectral representations.

We present here analysis of Moiré effect between monochrome, black and white images. Each monochrome image can be represented in the image domain by a reflectance function, which assigns to any point (x, y) of the image a value between 0 and 1, representing its light reflectance (0 for black and 1 for white). A superposition of such images can be obtained by means of overprinting, which simply means to intentionally print one layer of ink on top of another. Since the superposition of black and any other shade always gives

black, this suggests a multiplicative model for the superposition of monochrome images [6].

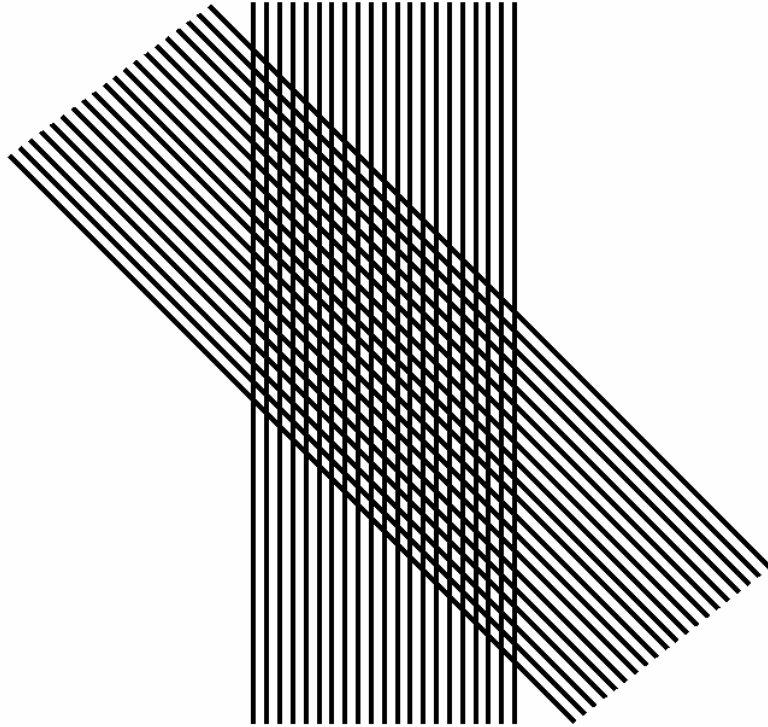


Figure 2-6: Superposition of periodic black and white images

Figure 2-6 presents an example of overprinting which reaffirms the concept of a multiplicative model for superposition. Thus, when m monochrome images are superposed, the reflectance of the resulting image is

$$r(x, y) = r_1(x, y)r_2(x, y)\dots\dots r_m(x, y) \quad (2.13)$$

Thus in the spectral Fourier domain,

$$R(u, v) = R_1(u, v) ** R_2(u, v)\dots\dots ** R_m(u, v) \quad (2.14)$$

where the Fourier transform of each function is represented by the respective capital letter and $**$ denotes two-dimensional convolution operation.

In Moiré interferometry, we mainly deal with periodic images. Thus the spectrum of the image consists of impulses, which represents the frequencies in the Fourier series decomposition of the image. A strong impulse in the spectrum indicates a dominant periodic component in the original image at the frequency of that impulse. The impulse at origin represents zero frequency, which corresponds in the image domain to the constant component of the image and its amplitude represents the intensity of this component image. Consider the case of periodic images, which are centered symmetrically about the origin. The images and their superposition are real valued and symmetric and so are their spectra. Thus each image in the spectrum is always accompanied by a twin impulse, symmetrically located at the other side of the origin (except an impulse at DC).

The most fundamental case of images is that of gratings with a co-sinusoidal profile. A grating is essentially a system of close equidistant and parallel lines or bars. As reflectance functions take value from 0 to 1, while cosines vary from -1 to 1 , the co-sinusoidal reflectance function actually has the form of a raised cosine wave as in Eqn. 2.7

$$r_1(x, y) = \frac{1}{2} \cos(2\pi f_1 x) + \frac{1}{2} \quad (2.15)$$

This is periodic with a spatial period $D_1 = 1/f_1$

Consider a second grating with frequency f_2 rotated by angle θ_2

$$r_2(x, y) = \frac{1}{2} \cos[2\pi f_2(x \cos \theta_2 + y \sin \theta_2)] + \frac{1}{2} \quad (2.16)$$

Two-dimensional Fourier transform of both of these reflectance functions yields three impulses, two symmetric impulses of amplitude 0.25, located at a distance of f_i from the origin in the direction θ_i and an impulse of amplitude 0.5, at the origin. The spectrum of the superposition is the convolution of these two spectra and thus consists of nine impulses. The geometric location of the impulses in the convolution can be found simply by placing on top of each impulse of $R_1(u, v)$, a centered copy of $R_2(u, v)$ or vice versa. We get all the impulse pairs of previous spectra and two new impulse pairs $(f_1 + f_2) \leftrightarrow -(f_1 + f_2)$ and $(f_1 - f_2) \leftrightarrow -(f_1 - f_2)$

These new impulse pairs suggest the presence of two new periodic components in the superposition image, which do not exist in the original spectrum. The first periodic component is more visible than the other since its frequency is lower. $f_1 - f_2$ may even be significantly smaller than the individual frequencies and thus much more visible than the cosines of the original image. This prominent periodic component is the moiré effect that is seen in the superposition of the two original images.

Moiré interferometry combines the concepts and techniques of geometrical moiré and optical interferometry. It is capable of measuring in-plane displacements with a very high sensitivity. In this method a diffraction grating is

produced on the specimen, so that when a stress is applied to the specimen the grating exactly follows its deformations. Two beams of coherent light illuminate the specimen grating obliquely at angles α and $-\alpha$, generating constructive and destructive interferences, which play the role of a virtual reference grating. The deformed specimen grating and the virtual reference grating generate together a moiré effect, which reveals the strain pattern of the deformations.

2.4 Projection based Measurement Techniques

Fringe projection is a simple way of contouring in which interference fringes are projected onto the object under test at a given angle and are viewed from a different angle. It is a convenient technique for contouring objects with too great a height variation to be measured with standard interferometry. Two variants of fringe projection technique, namely *fringe projection with coherent light* and *fringe projection with incoherent light* can be implemented, based on the type of illumination and fringe generation technique. These are explained in detail in the following sections.

2.4.1 Fringe Projection with Coherent Light

When a sinusoidal intensity distribution is projected on a surface, the mathematical representation of the deformed grating image intensity distribution is similar to that obtained in conventional interferometry. The surface height

distribution can be translated to a phase distribution, which can be obtained by means of Fourier transform analysis.

A sinusoidal intensity distribution can be projected on the surface of interest by generating an interference pattern between two coherent plane wave fronts. In coherent light fringe projection, a laser source in conjunction with an interferometer such as a Michelson interferometer is used to generate the interference fringes to be projected. The fringe spacing p is given by

$$p = \frac{\lambda}{2 \sin \theta} \quad (2.17)$$

Here λ is the wavelength of illumination and 2θ is the angle between the two interfering beams, as shown in Figure 2-7. From Eqn. 2.17, we can see that simply by tilting one beam with respect to another, the fringe period can be changed. The larger the angle between the two beams, the smaller will be the fringe period.

For geometrical analysis of a fringe projection system [7], consider two plane waves with propagation vectors \vec{n}_1 and \vec{n}_2 incident on a surface S_1 whose height distribution is to be determined. This results in an interference fringe pattern being projected on the surface. Let the surface height be described by a function $z_1=f_1(x, y)$. This is shown in Figure 2-7.

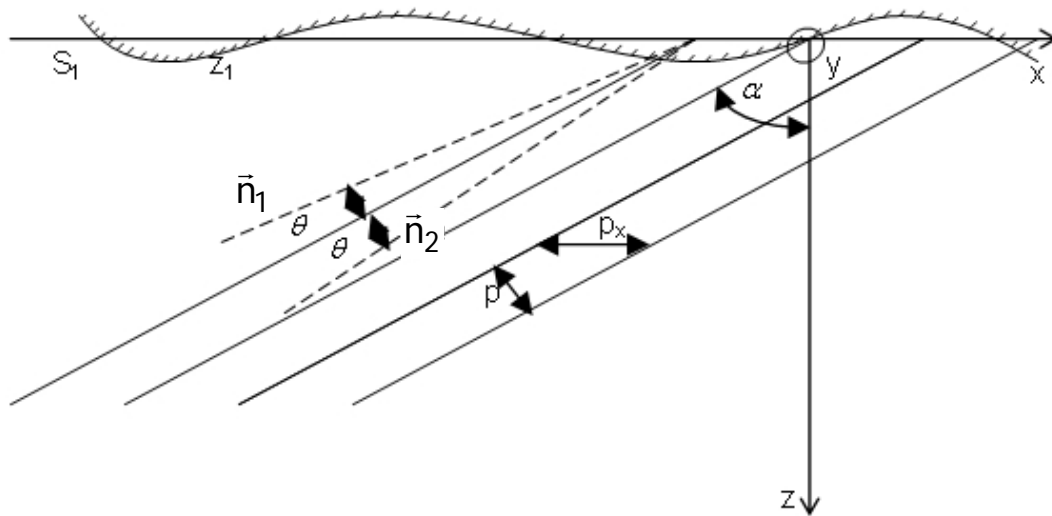


Figure 2-7: Analysis of fringes with fringe spacing p projected at an angle α on the surface under test

The two waves in the directions \vec{n}_1 and \vec{n}_2 lie in the xz -plane making an angle 2θ to each other and the line bisecting 2θ makes an angle α to the z axis. The two incident waves have equal intensity I_0 . The intensity distribution across the surface is found as

$$I_1(x, y) = 2I_0(x, y) \left[1 + \cos \frac{2\pi}{p} (x \cos \alpha + z_1 \sin \alpha) \right] \quad (2.18)$$

where the distance p between the fringes is as defined in Eqn. 2.17. Eqn. 2.18 can be obtained easily from the basic interference equation. Appendix A outlines the steps to obtain the above equation, as shown in Eqn. A.6.

For moderately curved surfaces, Eqn. 2.18 can be regarded as a phase-modulated sinusoidal grating with the spatial period

$$p_x = \frac{p}{\cos \alpha} \quad (2.19)$$

which corresponds to the spatial frequency

$$f_{cx} = \frac{1}{p_x} = \frac{\cos \alpha}{p} \quad (2.20)$$

and the spatial phase modulation function

$$\psi_1(x, y) = z_1 \sin \frac{\alpha}{p} = f_1(x, y) \sin \frac{\alpha}{p} \quad (2.21)$$

where $z_1=f_1(x, y)$ describes the surface.

Hence, Eqn. 2.18 changes to

$$I_1(x, y) = 2I_0(x, y) \left\{ 1 + \cos 2\pi \left[\frac{x}{p_x} + \psi_1(x, y) \right] \right\} \quad (2.22)$$

A practical way of applying this method is sketched in Figure 2-8 where the two plane waves are formed in a Michelson interferometer with a small tilt of one of the mirrors.

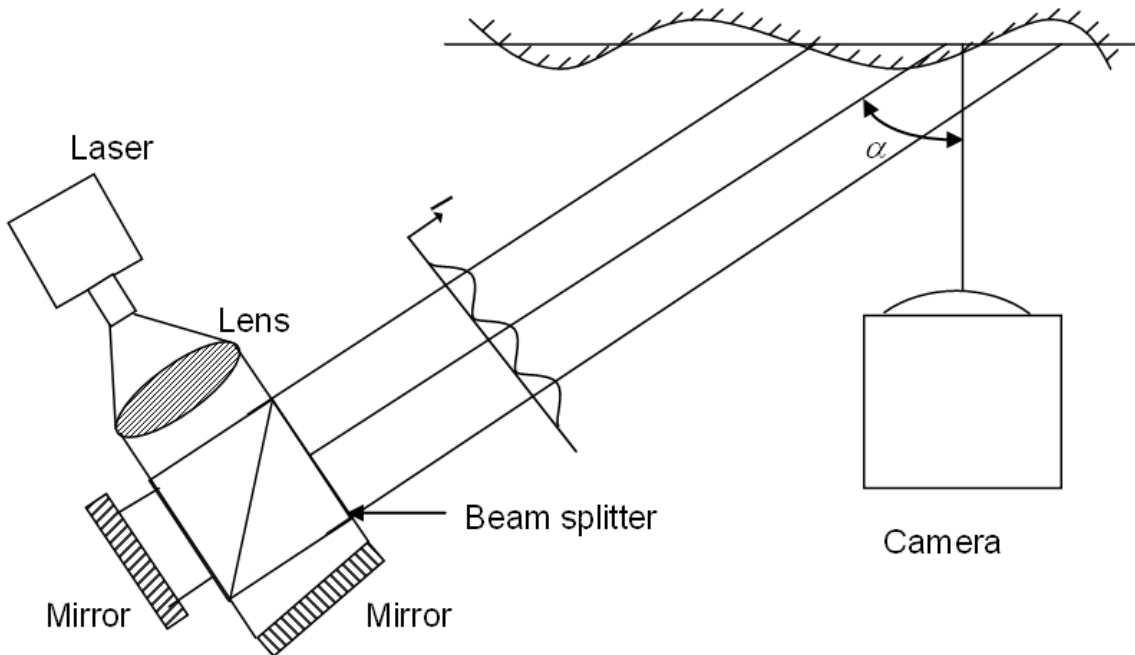


Figure 2-8: Fringe projection using a coherent light source

The camera placed along the z-axis captures the surface with the projected fringe pattern. The resulting intensity I_1 captured by the camera is given by Eqn. 2.22. The surface then undergoes a change (with progress of condensation in our case), after which it is described by the function $z_2 = f_2(x, y)$. The intensity captured by the camera then changes to I_2 .

$$I_2(x, y) = 2I_0(x, y) \left\{ 1 + \cos 2\pi \left[\frac{x}{p_x} + \psi_2(x, y) \right] \right\} \quad (2.23)$$

where

$$\psi_2(x, y) = \frac{z_2 \sin \alpha}{p} \quad (2.24)$$

Thus, any change in the surface topology manifests itself in the form of change in the phase term. The phase $\phi(x, y)$ which contains the surface change information equals the difference of arguments of the cosine terms in Equations 2.23 and 2.22 such that

$$\phi(x, y) = \psi_2(x, y) - \psi_1(x, y) \quad (2.25)$$

This phase information can be obtained from spatial Fourier transform analysis of the image, as described in section 2.6 and can be further be used to obtain the height information $h(x, y)$ as below [8]:

$$h(x, y) = \frac{\lambda}{4\pi} \phi(x, y) \quad (2.26)$$

2.4.2 Fringe Projection with Incoherent Light

In the case of incoherent light fringe projection, the light source is changed to a white light source. White light is the term used to describe the low coherence nature of the light sources, such as LEDs, used in such a technique. Since it is much more difficult to observe interference between waves generated from such sources, the fringe generation technique is modified. A structured light pattern is projected onto the copper surface by the use of a Ronchi ruling. The schematic diagram is as shown below in Figure 2-9.

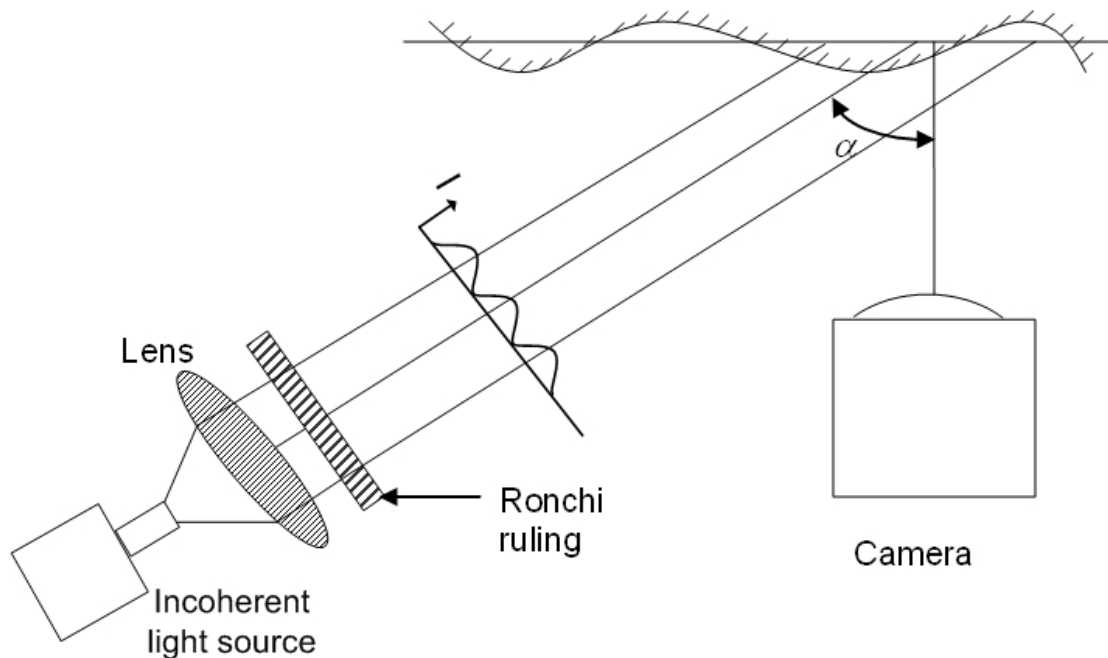


Figure 2-9: Fringe projection using an incoherent light source

A Ronchi ruling has a square wave profile with light and dark strips of equal size.

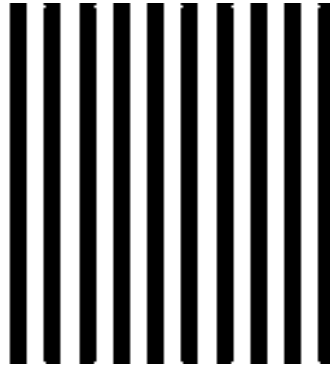


Figure 2-10: Ronchi ruling

The intensity transmittance function [9] of the ruling can be expressed in terms of the Fourier series in Eqn. 2.27

$$I_1(x, y) = a_1 + \sum_{n=1}^{\infty} b_{1n} \cos[n\phi_1(x, y)] \quad (2.27)$$

where $\phi_1(x, y)$ is the function describing the basic shape of the grating lines. For the fundamental frequency, $\phi_1(x, y)$ equals $2\pi m$ at the center of each bright line and $2\pi(m + 1)$ at the center of each dark line where m is a positive integer. The b coefficients determine the profile of the grating lines, such as sinusoidal, square wave etc. In case of a sinusoidal grating, only the b_{11} coefficient is non-zero and the equation is similar to Eqn. 2.18, for the case of coherent light fringe projection.

The two main differences between incoherent and coherent light fringe projection are in the type of light source and as a consequence, the type of fringe generation mechanism. The projection mechanism remains unchanged and the analysis procedure also remains the same except for some adjustment

in the filtering parameters. This will be explained in further detail in section 2.6 of this chapter covering the theoretical analysis procedure.

2.5 Selection of Technique

The choice of the most appropriate technique for the system was based on our requirement for a system suitable for experiments in spaceflights. Thus, it was important for the technique to be such that it leads to a system which is compact, portable and robust to vibration. Another important requirement was the need to measure large height variations in the condensation film (0.5-5mm). Standard interferometry is able to detect surface height variations on the order of a few wavelengths of the laser used for measurement. For surfaces, which have much larger height variations, the classical interferometry techniques fail to perform well, and we need to utilize other techniques such as fringe projection, moiré interferometry etc. Among these two, we selected the fringe projection technique for its ease of implementation especially in the case of measurement of fluid film profile.

2.6 Theoretical Analysis Procedure

The Fourier transform method for fringe pattern analysis requires an added high spatial carrier frequency. In the coherent light fringe projection system, the straight and equally spaced sinusoidal fringes are the carriers. In

case of incoherent light fringe projection, we use a Ronchi ruling with a square wave profile to produce the carrier. Hence, we have a base carrier frequency and higher harmonics of the same frequency. Proper selection of the spatial carrier frequency enables the generation of the contour using Fourier transform and phase unwrapping techniques. The biggest advantage of this method is the requirement of only a single fringe pattern for processing.

We explain below the analysis procedure [10] which remains same for both coherent and incoherent light fringe projection system. As our system involves the carrier fringes generated parallel to the y axis, i.e. the carrier frequency involves only the x-component; thus the carrier modulated fringe pattern can be described by

$$I(x, y) = a(x, y) + b(x, y) \cos[2\pi f_{cx} x + \psi(x, y)] \quad (2.28)$$

where $a(x, y)$ and $b(x, y)$ are the unwanted background and modulation terms, respectively, f_{cx} is the spatial carrier frequency given by Eqn. 2.20 and $\psi(x, y)$ contains the desired phase information. Eqn. 2.28 is essentially the same as Eqn. 2.7 using slightly different conventions for ease of Fourier analysis. It can be further modified to

$$I(x, y) = a(x, y) + c(x, y)e^{j2\pi f_{cx} x} + c^*(x, y)e^{-j2\pi f_{cx} x} \quad (2.29)$$

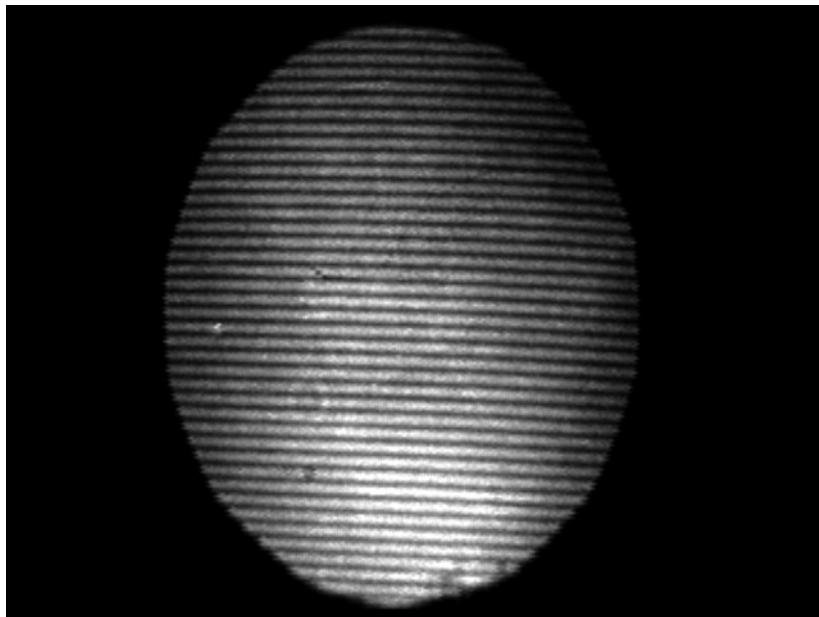
where

$$c(x, y) = \frac{1}{2} b(x, y) \exp[i\psi(x, y)] \quad (2.30)$$

The two dimensional Fourier transform of the intensity distribution in Eqn. 2.29 yields

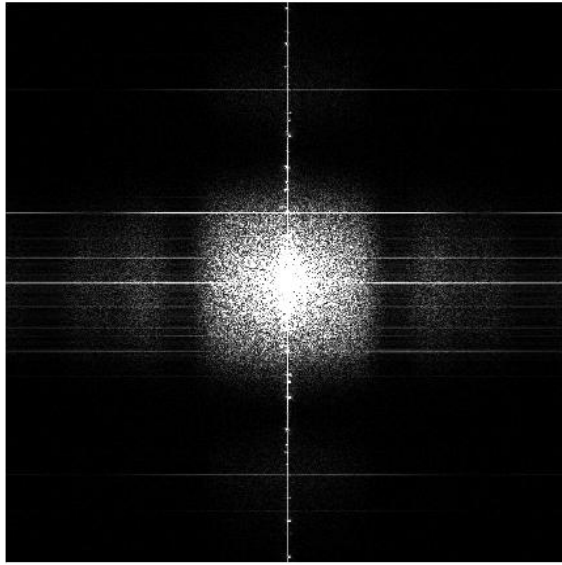
$$I(f_x, f_y) = A(f_x, f_y) + C(f_x - f_{cx}, f_y) + C^*(f_x + f_{cx}, f_y) \quad (2.31)$$

Since in most cases, $a(x, y)$, $b(x, y)$ and $\psi(x, y)$ vary slowly as compared to f_{cx} , all the spectra are separated from each other by the carrier frequency f_{cx} . One of the side lobes is weighted down by the Hanning window and translated by f_{cx} toward the origin to obtain $C(f_x, f_y)$. The central lobe and either of the two side lobes are filtered out by the above translation. Figure 2-11 (a) through (i) illustrates this process graphically. Here we present the Fourier transform of one of the reference fringe pattern images from our experiments (Figure 2-11(a)) and walk through the processing aspects:

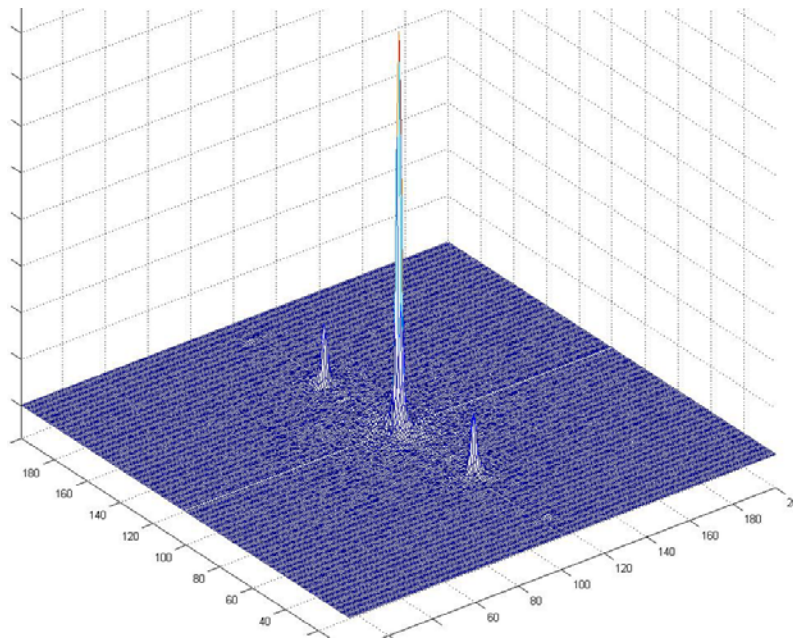


(a) Reference image on copper surface

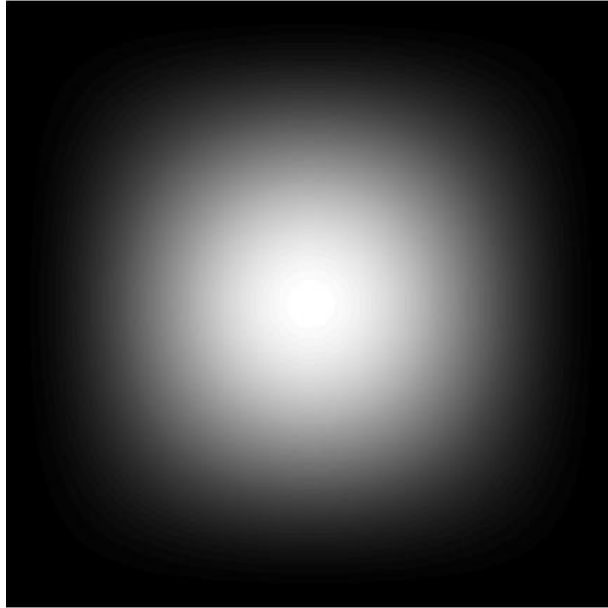
Note that the data range of the FFT image (Figure 2-11(b)) is on the order of $10E7$. As a result, even the zoomed-in 3-D view (Figure 2-11(c)) of the FFT image fails to show all the details as the 2D view.



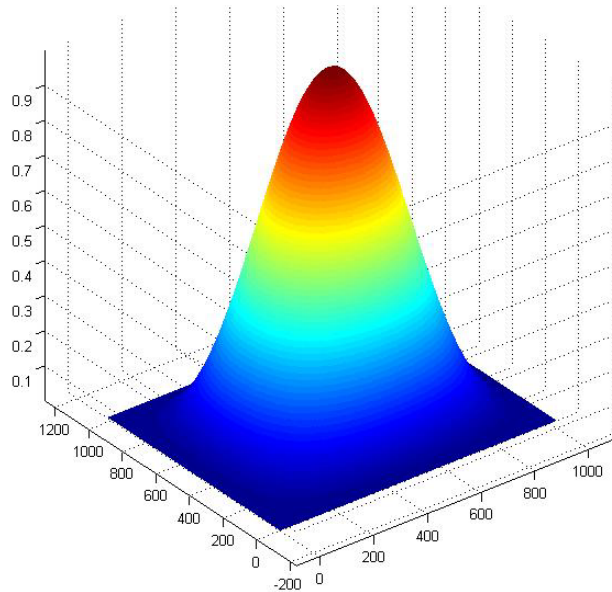
(b) Unfiltered Fourier transformed image (2-D view)



(c) Unfiltered Fourier transformed image (zoomed in 3-D view)



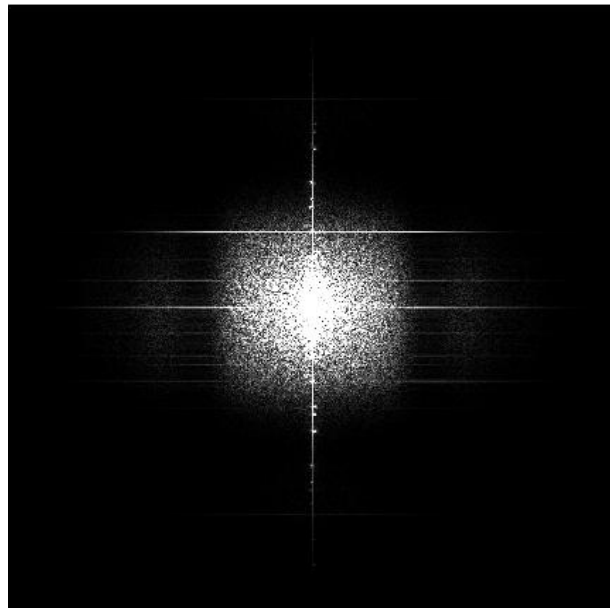
(d) 2-D Hanning Window in the spatial frequency domain having the same size as the image (2-D view)



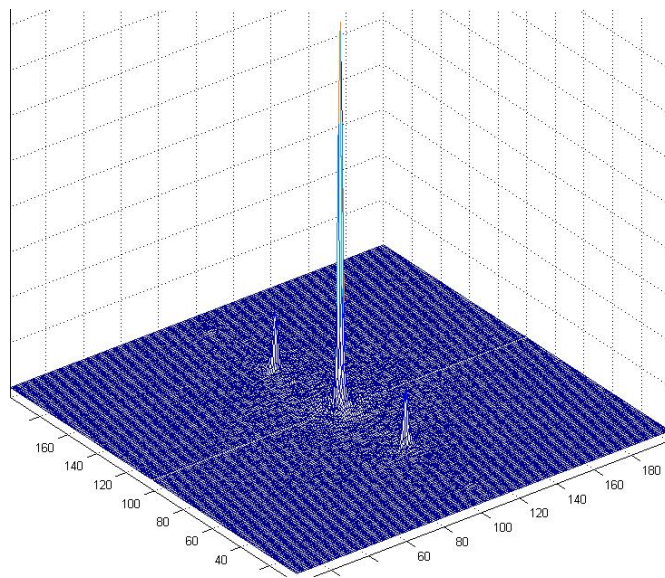
(e) 2-D Hanning Window of the same size as the image (3-D view)

When the 2-D Hanning window (Figure 2-11(d)) is multiplied with the 2-D FFT image (Figure 2-11(b)), the resultant image is Figure 2-11(f). The difference between the images in 2-11(b) and (f) can be seen only in the

peripheral regions of the image (due to the nature of the Hanning window). The central part remains unchanged. This is also the reason why Figure 2-11(g), which is a zoomed-in 3-D view of the central part of the windowed image, appears same as Figure 2-11(c), which is the equivalent non-windowed image.

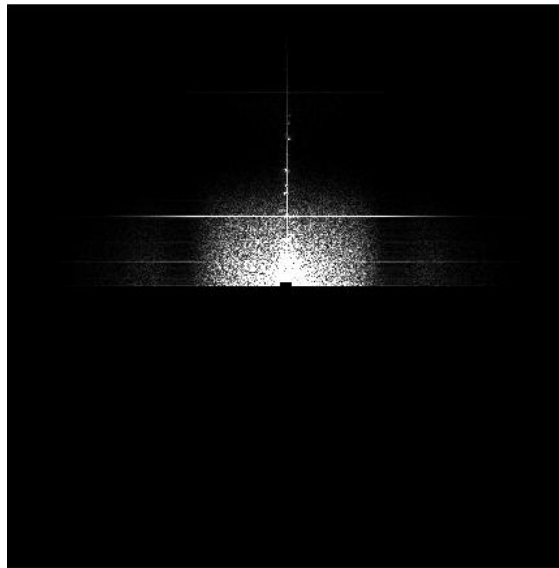


(f) Windowed image (2-D view)

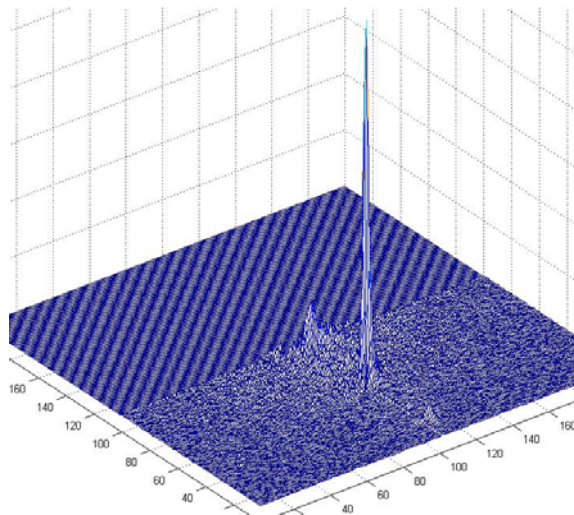


(g) Windowed image (3-D view)

Figure 2-11(h) shows the filtering out of the negative spatial frequency. Note that these negative frequencies are only being removed along f_x and not f_y , in accordance with the discussion following Eqn 2.31 (Note: The spatial carrier frequency introduced by the fringes is f_x).



(h) Windowed image after filtering (2-D view)



(i) Windowed image after filtering (3-D view)

Figure 2-11: (a) through (i) - Filtering and Windowing process

Taking two dimensional inverse Fourier transform of $C(f_x, f_y)$ yields $c(x, y)$.

The phase distribution may then be calculated point-wise using

$$\psi(x, y) = \arctan\left(\frac{\text{Im}[c(x, y)]}{\text{Re}[c(x, y)]}\right) \quad (2.32)$$

where $\text{Im}[c(x, y)]$ and $\text{Re}[c(x, y)]$ denote the imaginary and real parts of $c(x, y)$, respectively. As this phase calculation yields values ranging from $-\pi$ to $+\pi$, the phase distribution is said to be wrapped around this range and has phase discontinuities. These can be corrected using phase unwrapping process. Using unwrapped values of $\psi_1(x, y)$ and $\psi_2(x, y)$, we can obtain $\phi(x, y)$ using Eqn. 2.25 and finally obtain the height information for the surface film from Eqn. 2.26.

In case of incoherent light fringe projection, the above described technique remains the same. Since the Ronchi ruling has a square wave profile, there exist higher harmonics of the carrier frequency, which correspond to smaller side lobes. Thus, to extract the $c(x, y)$ term, these smaller side lobes also need to be filtered out. Hence, in case of incoherent light fringe projection, there is only a small change in the area to be filtered out.

Chapter 3: Hardware System Setup

3.1 Overall System Description

The basic concept behind the surface mapping of the fluid film is the principle of fringe projection. The optical system has been implemented on an optical base plate of size 12" x 12", consisting of a solid aluminum plate, anodized black and tapped with ¼-20 holes. The key optical and imaging components of the system are mounted on this base plate. The other important part of the system is the computer system in the form of a laptop containing the frame grabber and the optical fringe analysis software. In addition to these main parts, the system requires many other accessories such as power supply adapters for the light source, camera adapter and optionally the ultrasonic instrumentation. Figure 3-1 shows a photo of the test setup.

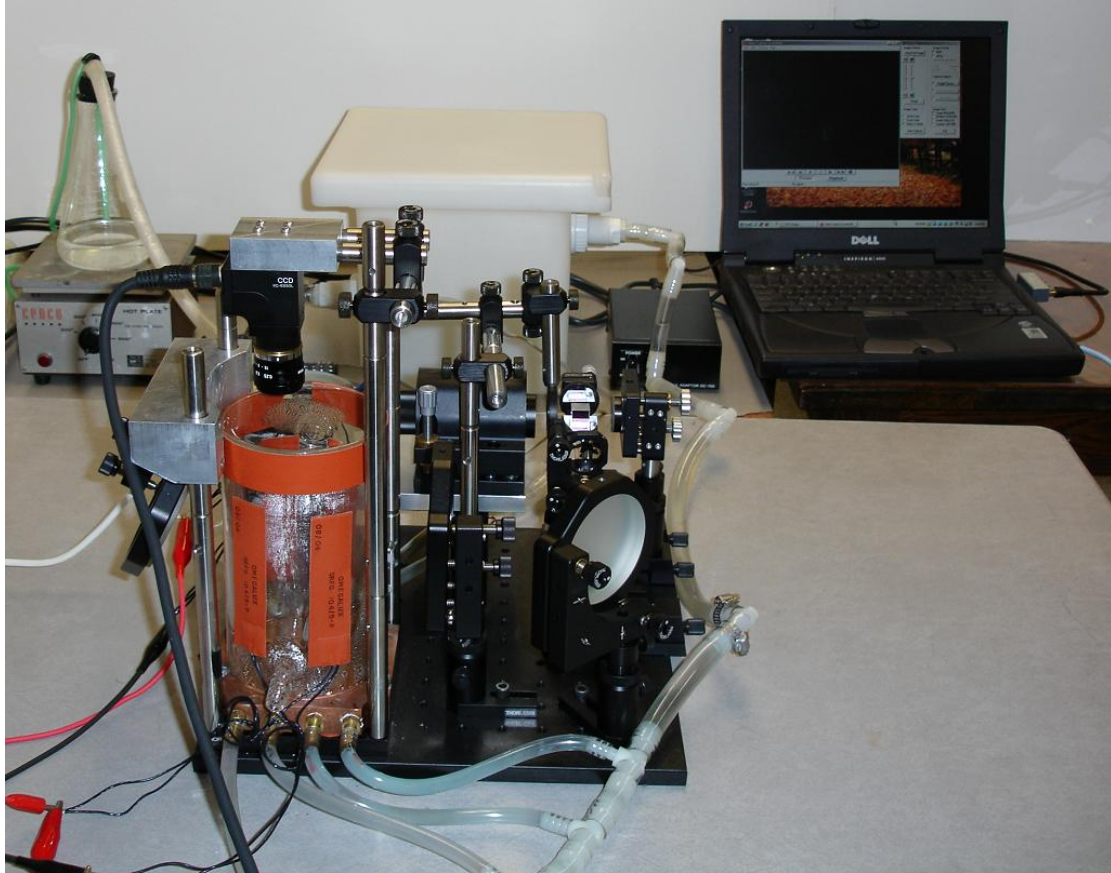


Figure 3-1: Fringe projection system setup

3.2 Hardware Components

We have considered two different implementations of fringe projection, one using coherent light and the other using incoherent light. The coherent light system was first implemented, which was found to give promising results. However, there was a significant amount of noise, as a consequence of the speckles present in coherent imaging systems. The resultant images consisting of the noise are presented in Chapter 5 with additional details regarding the experiments. An alternative approach in the form of incoherent light fringe

projection was then investigated. Many of the components are common in each of the techniques. We begin by describing the basic setup of a fringe projection system, followed by a description of both the coherent and incoherent light fringe projection systems.

Figure 3-2 below shows the block diagram for the setup of a basic fringe projection system:

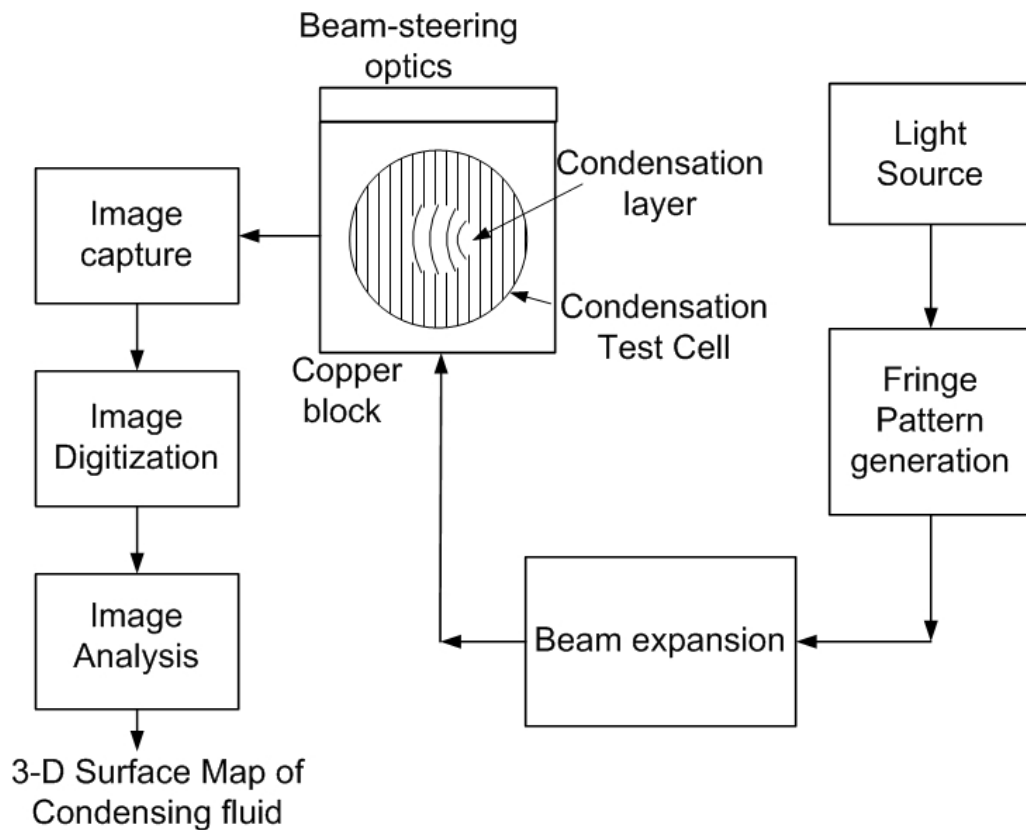


Figure 3-2: Basic fringe projection system block diagram

In any fringe projection system, the essential functional blocks include

1. A light source
2. A system for the generation of fringes
3. Fringe projection optics

4. Image capture and analysis system

The light generated from the light source goes into the fringe generation system. The fringe patterned obtained from this block is passed through some form of a beam expander which ensures that the beam is sufficiently big to cover the region of interest. Through the use of beam steering optics, the beam is projected onto the test surface which introduces deformation in the fringe pattern in accordance with the surface topology of the surface. Finally, the deformed pattern is captured, digitized and sent for analysis.

Depending on the light source and accordingly the fringe generation technique, the system can be categorized as a coherent light fringe projection system and an incoherent light fringe projection system. We now explain each of these systems in detail.

3.2.1 Coherent Light Fringe Projection System

The system can be logically divided into two subsystems, one responsible for the projection of fringes and the other responsible for imaging of the deformed fringe pattern. The projection subsystem consists of the light source, which in this case is a laser. The other components in this subsystem are the collimator, the interferometer for the generation of fringes and the optics for beam expansion and beam steering. The imaging subsystem consists of the camera, camera lens and the frame grabber. Figure 3-3 shows the block diagram for coherent light fringe projection.

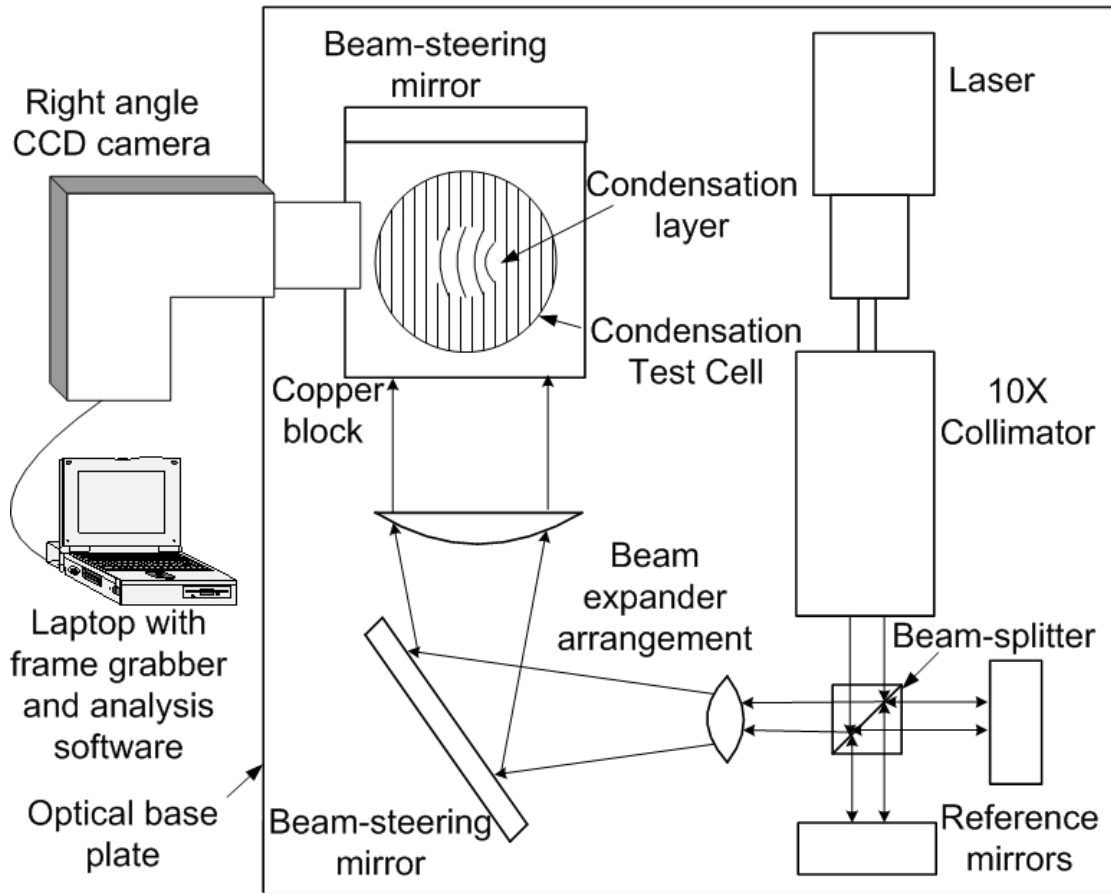


Figure 3-3: Block diagram of coherent light fringe projection system

The system utilizes an Nd:YVO₄ (Neodymium Doped Yttrium Orthvanadate crystal) frequency doubled laser as the monochromatic continuous wave light source. This is a diode pumped solid-state green laser with center wavelength 532nm. This laser provides an extremely well collimated beam along with a long coherence length, which is ideal for interferometry applications.

The laser light is then passed through the collimator assembly where the beam diameter is expanded by a factor of 10. This is necessary for uniformly illuminating a greater area of the surface to be imaged.

The collimated beam of laser light falls upon the beam splitter. An ideal partially reflecting beam splitter would transmit one half and reflect one half of the incident light with constant phase change, irrespective of the polarization of the light. However, practically all reflecting surfaces used at angles other than normal incidence have properties that vary with the polarization of the radiation. Thus to avoid these complications, we have chosen our laser source to have linear polarization. Also, the beam splitter chosen is not a plate beam splitter but a cube beam splitter. This ensures that the beam splitter does not exhibit ghost reflections nor does it displace the transmitted beam as plate beam splitters do. It does not introduce any path difference in the system and being a non-polarizing beam splitter, it provides true 50/50 beam splitting without altering the beam polarization.

The two beams of equal intensity, one reflected and the other transmitted, strike the reference mirrors at normal incidence and are reflected back and meet at the beam splitter and combine to create interference patterns, known as fringes.

These fringes are further sent to a beam expander arrangement, formed by using a set of convex and plano-convex lenses, which expands the diameter of the fringe pattern that will illuminate the condensing fluid film.

The expanded beam is then projected on the copper block using a mirror. The camera, which looks down on the copper block captures the fringes deformed in accordance with the shape of fluid film on the copper surface.

Figure 3-4 shows a picture of the coherent light fringe projection system highlighting its key components.

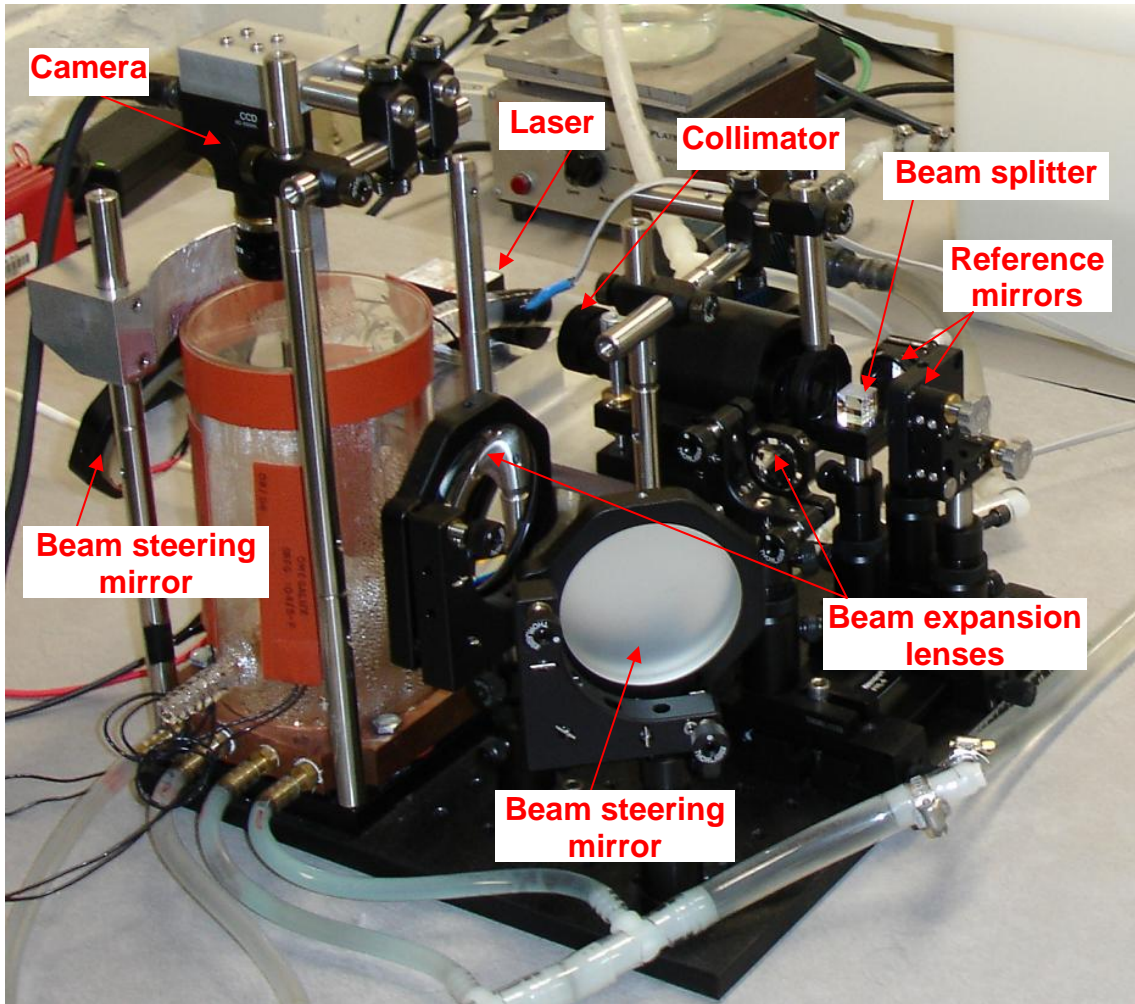


Figure 3-4: Coherent light fringe projection system setup

The camera is powered using the camera adapter. The output from the camera adapter is transferred to the laptop computer via the frame grabber. A frame grabber is a digital image acquisition board, which controls the camera and acquires the images from the camera. The most common frame grabbers

connect on the PCI slots of the computer. However to maintain the portability of the system, we have selected a PCMCIA type frame grabber.

The images on the computer are analyzed by the fringe analysis software on the laptop to obtain the surface map of the condensation film.

We now present the detailed specifications of each of the components of the system.

i. Laser

The BWT-5E laser from B&W Tek Inc. is a self-contained, thermoelectrically cooled, diode pumped, frequency doubled Nd:YVO₄ laser (532 nm). Nd:YVO₄ is one of the most efficient laser host crystal currently existing for diode laser-pumped solid-state lasers. The thermoelectric cooling modules are advantageous as they have no moving parts and therefore they are inherently reliable and virtually maintenance free. They can be operated in any orientation and are ideal for cooling devices that may be sensitive to mechanical vibration. Their compact size also makes them ideal for applications that are size or weight limited. The laser produces a stable 5mW output over 0 to 40°C. The excellent beam mode quality and low divergence makes the laser suitable for beam focusing and long distance beam positioning. The compact size, long life and excellent beam quality of the laser were some of the important factors for the choice of this laser.

Another important characteristic of a laser is its polarization. We discuss here the basic concept of polarization.

Polarization is a phenomenon observed in transverse waves, i.e., waves that vibrate in a direction perpendicular to their direction of propagation. Light is a transverse electromagnetic wave. A light wave traveling forward can consist of an electric field oscillating up and down (in the vertical plane), oscillating from side to side (in the horizontal plane), or oscillating in an intermediate direction. Ordinarily a ray of light consists of a mixture of waves oscillating in all the directions perpendicular to its line of propagation. If for some reason the vibration remains constant in direction, the light is said to be polarized. Thus, polarized light waves are light waves in which the oscillations occur in a single plane. The polarization of light is determined by the time course of the direction of the electric field vector [11].

Precise control of polarization behavior is necessary to obtain optimal performance from optical components and systems. Characteristics such as reflectivity and beam splitter ratios are be different for different polarizations. We have chosen all of our optical components optimized according to the linear polarization of our laser.

The laser is powered through the adapter provided with the laser, which takes in an input ranging from 100V-240V AC and gives a DC output of 5V at 4A. Table 3-1 lists detailed specifications of the laser.

<u>Specification</u>	<u>Detail</u>
Power output	> 5mW
Wavelength	532nm

Mode	TEM ₀₀
Power stability	< +/- 15%
Spectral linewidth	<01.nm
Beam divergence	<1.2mrad
Operating temperature	0-40°C
Polarization	> Linear 50:1 (45°, in reference to base plate)
Beam size	$\phi < 1\text{mm}$
Warm up time	15 min
Input power	100-240VAC/50-60Hz
Laser head dimension	30 x 30 x 66mm
Power supply adapter dimension	55mm H x 105mm W x 170mm L

Table 3-1: Specifications of the laser

ii. Collimator

The model LC-075 from Newport Corporation is a 10x laser collimator optimized specifically for low wavefront distortion and diffraction limited performance at infinity focus in the visible wavelength region. It is a Galilean optical system, antireflection coated with visible MgF₂ for maximum transmission. The design principle of an optical system may be Galilean or based on Kepler's principle. With Galilean principle, the beam of light first passes through a negative optical element which causes the beam to diverge and then it passes through a positive optical element which restores the beam to a parallel beam.

<u>Specification</u>	<u>Detail</u>
Expansion ratio	10X
Entrance aperture	1.9mm
Exit aperture	19mm
Wavelength	400–700 nm
Wavefront distortion	$\leq \lambda/10$ at infinity focus
Damage Threshold	100 W/cm ² CW, 2 J/cm ² with 10 nsec pulses, typical

Table 3-2: Specifications of the collimator

iii. Michelson Interferometer

As explained in Chapter 2, a Michelson interferometer consists of a beam splitter, which divides the incident beam coming from the coherent light source into two beams of equal intensity, with one reflected and the other transmitted. These beams strike the two reference mirrors at normal incidence and are reflected back and meet at the beam splitter and combine to create interference patterns. Figure 2-2 in Chapter 2 illustrates the basic setup of a Michelson interferometer. The specifications of the beam splitter and the reference mirrors are presented in the following sections.

(1) Beam splitter: The model 05BC16NP.3 from Newport Corporation is a non-polarizing cube beam splitter. In this beam splitter, the incoming beam is both reflected and transmitted 50% with the s (component of electric field perpendicular to the plane of incidence) and p (component of electric field

parallel to the plane of incidence) components matched to within 3% of each other. It consists of a pair of precision right-angle prisms carefully cemented together to minimize wavefront distortion. The hypotenuse of one of the prisms is coated with a multilayer all-dielectric non-polarizing beam splitter coating optimized for the wavelength of 532nm. The four faces are antireflection coated with a multi layer dielectric coating to minimize surface reflection losses at this wavelength. Another important specification considered in selection of optics is the surface quality. Surface quality describes the number and size of defects typically scratches and pits (also known as digs). Scratch-dig is specified by two numbers. The first number relates to the apparent size of scratches and the second to the apparent size of digs. A number 10 scratch indicates a 1 μm wide scratch, while a number 1 dig is identical to a 0.01mm diameter standard pit.

The material used for the beam splitter and most other optics in our system is BK7. BK7 is a borosilicate crown glass that is used primarily for shaped optics such as lenses and prisms. BK7 is a hard glass with excellent homogeneity. It is relatively resistant to chemical attack and has a transmittance window of approximately 350-2200 nm. BK7 has an index of refraction of 1.51947 at 532 nm.

Detailed specifications of the beam splitter are listed in Table 3-3.

<u>Specification</u>	<u>Detail</u>
Dimension	12.7mm
Wavelength	532nm

Material	BK 7, grade A, fine annealed optical glass or equivalent
Wavefront Distortion	$\leq \lambda/4$ at 632.8 nm over the clear aperture
Clear Aperture	> central 80% of dimension
Surface Quality	20-10 scratch-dig
Transmission	$50 \pm 3\%$, independent of polarization
Reflection	$50 \pm 3\%$, independent of polarization
Polarization	s and p polarization components matched to within 3%, $ T_s - T_p \leq 3\%$, $ R_s - R_p \leq 3\%$
Transmitted Beam Deviation	≤ 5 arc min
Reflected Beam Deviation	$90^\circ \pm 5$ arc min
Angle of Incidence	$0^\circ \pm 2^\circ$
Dimension Tolerance	± 0.25 mm
Antireflection Coating	Multilayer coating, $R < 0.5\%$
Temperature Range	-50°C to 90°C
Damage Threshold	2 kW/cm^2 CW, 1 J/cm^2 with 10 nsec pulses, typical

Table 3-3: Specifications of the beam splitter

(2) Reference mirrors: The reference mirrors shown in Figures 3-3 and 3-4 are protected Aluminum mirrors (Model PF10-03-G01) from Thorlabs. For general broadband use, a protected aluminum coating offers the best option. A SiO coating is used to protect the delicate aluminum coating making it suitable for laboratory and industrial use. The protected aluminum coating gives a reflectivity that most closely matches the reflection of a bare aluminum coating.

The diameter of the mirror was chosen to be large enough to accommodate the collimated laser beam of diameter 9mm. The two closest choices available were 12.7mm and 25.4mm. It was decided to use the larger mirror so that the beam does not use more than 70% of the mirror area and is confined to central portion of the mirror which ensures reflection of the highest quality.

<u>Specification</u>	<u>Detail</u>
Diameter	25.4 mm
Reflectivity	>85% at 532 nm
Substrate Material	Fused silica
Surface flatness	$\lambda/10$ at 632.8 nm over the clear aperture
Clear Aperture	> central 90% of diameter
Surface Quality	10-5 scratch-dig
Protected silver coating	$R_{AVG} > 90\%$ for 400-10.0 μm
Damage Threshold	0.5 J/cm ² with 10 nsec pulse

Table 3-4: Specifications of the reference mirrors

iv. Beam expander arrangement

For expansion of the collimated laser beam, we use a technique known as “4f” or “Image Relay” solution. In this, we place two convex lenses as shown in Figure 3-5 at a distance $|f_1| + |f_2|$ apart where f_1 and f_2 are the focal lengths of the two lenses and d_1 and d_2 are the initial and final beam diameters respectively. Note that f_1 is a negative distance.

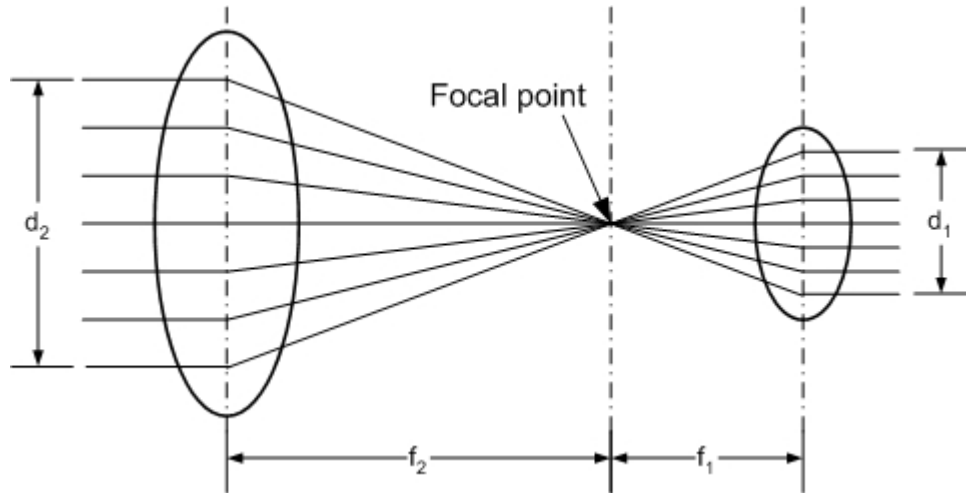


Figure 3-5: 4f imaging solution

It then holds that:

$$-\frac{f_2}{f_1} = \frac{d_2}{d_1} \quad (3.1)$$

We have the input beam diameter of 9mm and we require the output beam diameter around 50mm. We thus choose the lenses in the appropriate ratio of focal lengths.

We need

$$-\frac{f_2}{f_1} \geq \frac{50}{9} = 5.55 \quad (3.2)$$

We choose the following lenses. The smaller lens is KBX046AR.14, a bi-convex lens from Newport Corporation with focal length 25.4mm and diameter 25.4mm, while the larger lens is LA1353-A, a plano-convex lens from Thorlabs Inc. with focal length 200mm and diameter 75 mm.

This gives

$$-\frac{f_2}{f_1} = \frac{d_2}{d_1} = 7.87 \quad (3.3)$$

This will give an output beam diameter of about 70mm, when the input beam diameter is 9mm. Both the lenses are coated with antireflection coating to minimize reflections over the visible wavelength range. The specifications of the lenses are as listed in Table 3-5.

<u>Specification</u>	<u>Detail</u>
Diameter	KBX046AR.14: 25.4mm LA1353-A : 75mm
Effective focal length	KBX046AR.14: 25.4mm LA1353-A: 200mm
Focal Length tolerance	±1%
Material	BK 7
Clear Aperture	> central 90% of dimension
Surface Quality	40-20 scratch-dig
Diameter Tolerance	+0/-0.1 mm
Center Thickness (Tc) Tolerance	KBX046AR.14: ±0.1 mm LA1353-A : ±1 mm
Antireflection Coating	Broadband antireflection coating

Table 3-5: Specifications of the beam expansion lenses

v. Beam steering mirrors

The two beam steering mirrors shown in Figure 3-3 are broadband dielectric mirrors, which have R_s and R_p (reflectivity of the s and p components) greater than 99%. The model 30D10 from Newport Corporation is a 3-inch

(76.2mm) Pyrex lens, which has good surface flatness $\lambda/5$ and excellent surface quality expressed in terms of scratch dig parameter of 20-10. The detailed specifications are as below:

<u>Specification</u>	<u>Detail</u>
Diameter	76.2 mm
Angle of incidence	0-45°
Reflectivity	Rs, Rp >99%
S ₂ Surface	Ground
Clear Aperture	> central 80% of diameter
Surface Quality	20-10 scratch-dig
Diameter Tolerance	+0/-0.13 mm
Thickness Tolerance	±0.25 mm
Wedge	≤3 arc min
Chamfers	0.38–1.14 mm face width x 45° ±15°
Damage Threshold	1000 W/cm ² CW, 10 mJ/cm ² with 10 nsec pulses within the wavelength range, typical

Table 3-6: Specifications of the beam steering mirrors

We use the mirror with BD.1 coating that reflects all visible laser lines in the range 488–694 nm with greater than 99% efficiency for any polarization at 0–45° angle of incidence. This is important because our laser has the wavelength 632.8nm. Also we use the first beam steering mirror (in the beam expansion setup) at an angle of 45° while the second mirror which is used to project the expanded beam on the copper surface is at an angle of 28.5°. A special mount was constructed to hold this second mirror at an angle of 28.5°.

The design of this mount involved the criterion that the center of the beam should hit the center of the reference copper surface. Figure 3-6 below shows the detailed specification provided to construct this angle mount. Figure 3-7 shows a picture of the actual mount after construction.

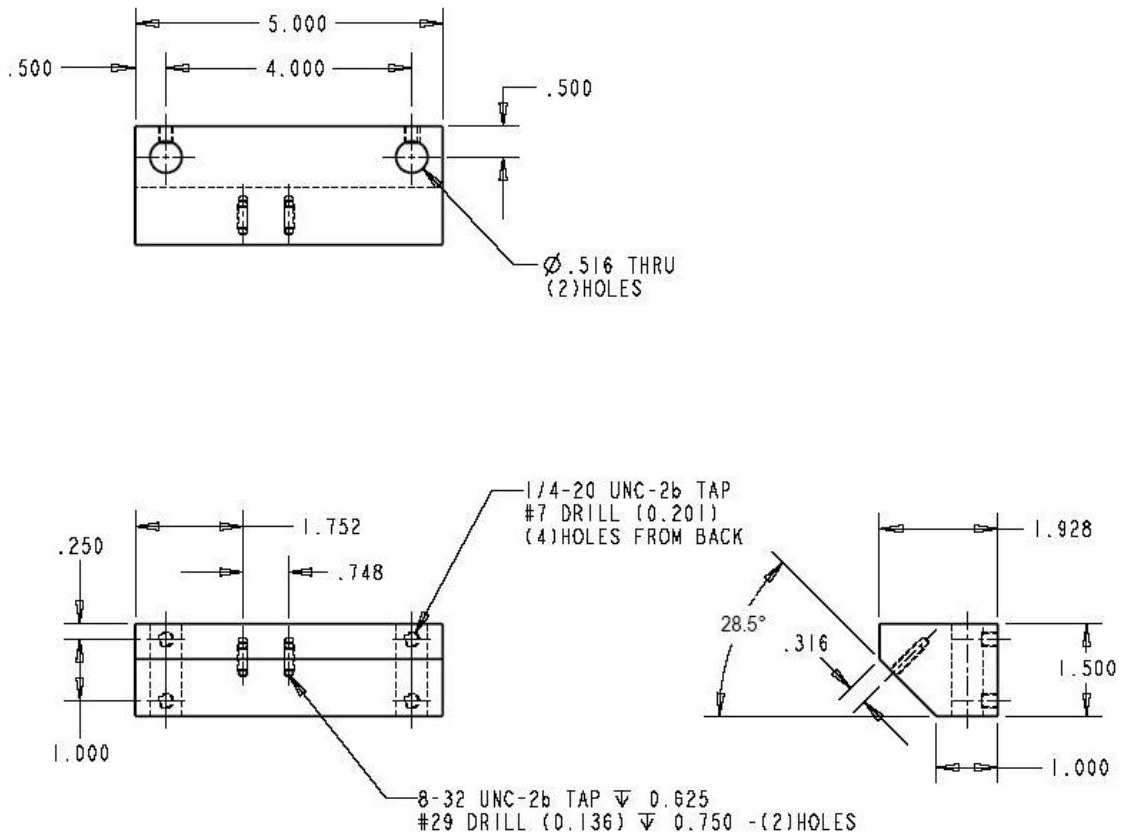


Figure 3-6: Specifications of angle mount for beam steering mirror



Figure 3-7: Picture of angle mount for beam steering mirror

vi. Camera

The XC-ES50L camera from Sony is a right angle version of the popular XC-ES50 camera. The new XC-ES50L camera incorporates a 1/2" CCD providing 768(H) x 494(V) effective picture elements and features a C-mount type lens mount. A 1/2" type CCD essentially means that the image sensor is of size 6.4mm x 4.8mm. The unique L shape compact body makes the XC-ES50L easy to install in narrow spaces and can be built-in with a turn capability of approximately 180 degrees. Figure 3-8 shows a picture the camera.



Figure 3-8: Right angle analog CCD camera (courtesy Sony)

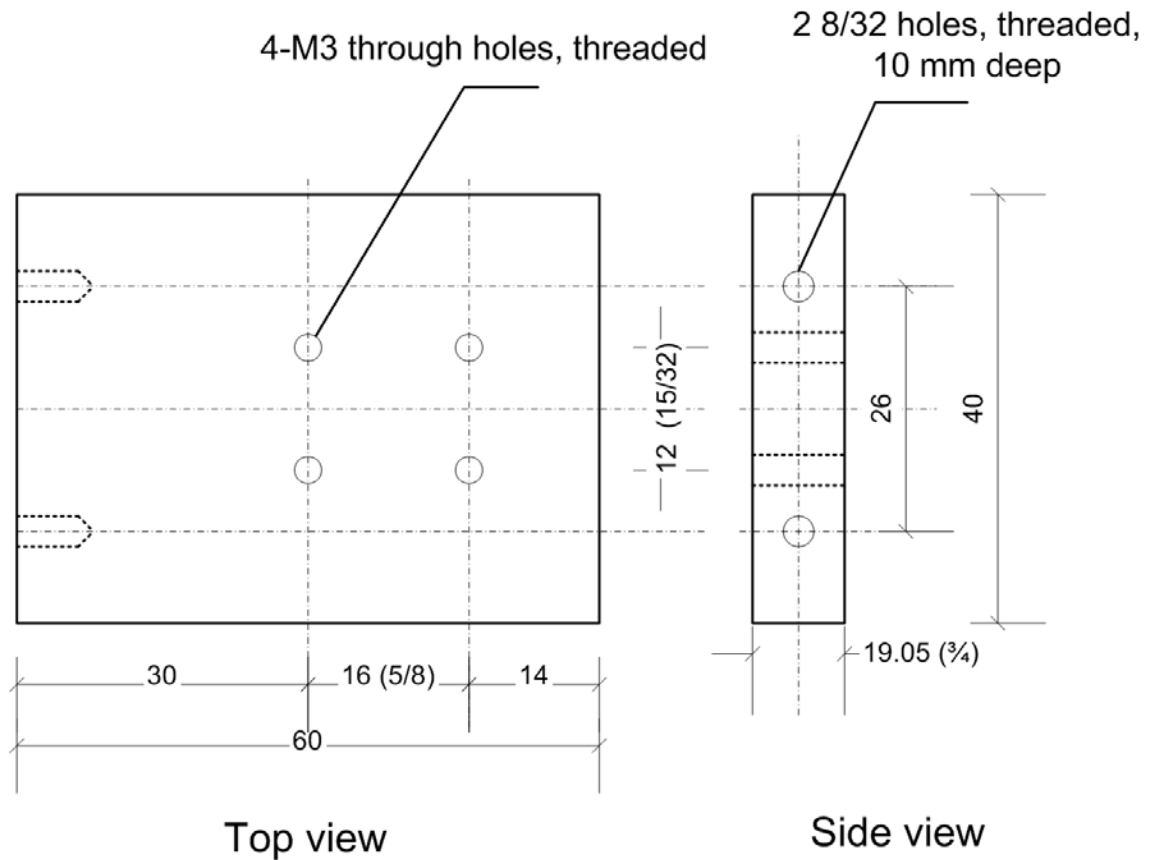
The XC-ES50L camera is an analog camera, ideal for machine vision and factory automation applications. Detailed specifications of the camera are presented in Table 3-7.

<u>Specification</u>	<u>Detail</u>
Image Device	½" Interline Transfer CCD
Signal System	EIA Standard
Effective Picture Elements	768 (H) x 494 (V)
Horizontal Frequency	15.734 kHz
Vertical Frequency	59.94 Hz
Cell Size	8.4 x 9.8 µm
Lens Mount	C Mount
Flange Back	17.526 mm
Sync System	Internal/External (auto)
External Sync System	HD / VD (2~5 Vp-p)
External Sync Frequency	+ / - 1%
Jitter	Less than + / - 50 nsec
Scanning System	2:1 Interlaced
Video Output	1.0 V p-p, negative, 75ohms

	unbalanced
Horizontal Resolution	570 TV Lines
Minimum Illumination	0.3 lx
S/N Ratio	60 dB
Gain	AGC (0-18 dB) / Manual (0-18 dB) selectable
Gamma	ON / OFF
External Trigger Shutter	¼ ~ 1/10,000s
Normal Shutter	1/100 ~ 1/10,000s
Power Requirements	DC-12V (+9 ~ 16V)
Power Consumption	1.6W
Dimensions	29 (W) x 42.5(H) x 43.8 (D)
Mass	110g
Operation Temperature/Moisture	-10 ~ +50° C / 20 ~ 80%
Vibration	10 G (20 ~ 200 Hz)
Shock Resistance	70 G

Table 3-7: Specifications of the camera

The camera is attached to the entire system using a custom-designed camera mount. This mount was constructed in accordance with the dimensions of the camera and the mounting holes provided on top of the camera. Care was taken to ensure that the mounting should not obstruct the light path or image capture path in any way. Figure 3-9 presents the specifications used to construct the camera mount and Figure 3-10 shows a picture of the mount as used to hold the camera in the system.



Units: mm (inches)

Figure 3-9: Specifications of the camera mount

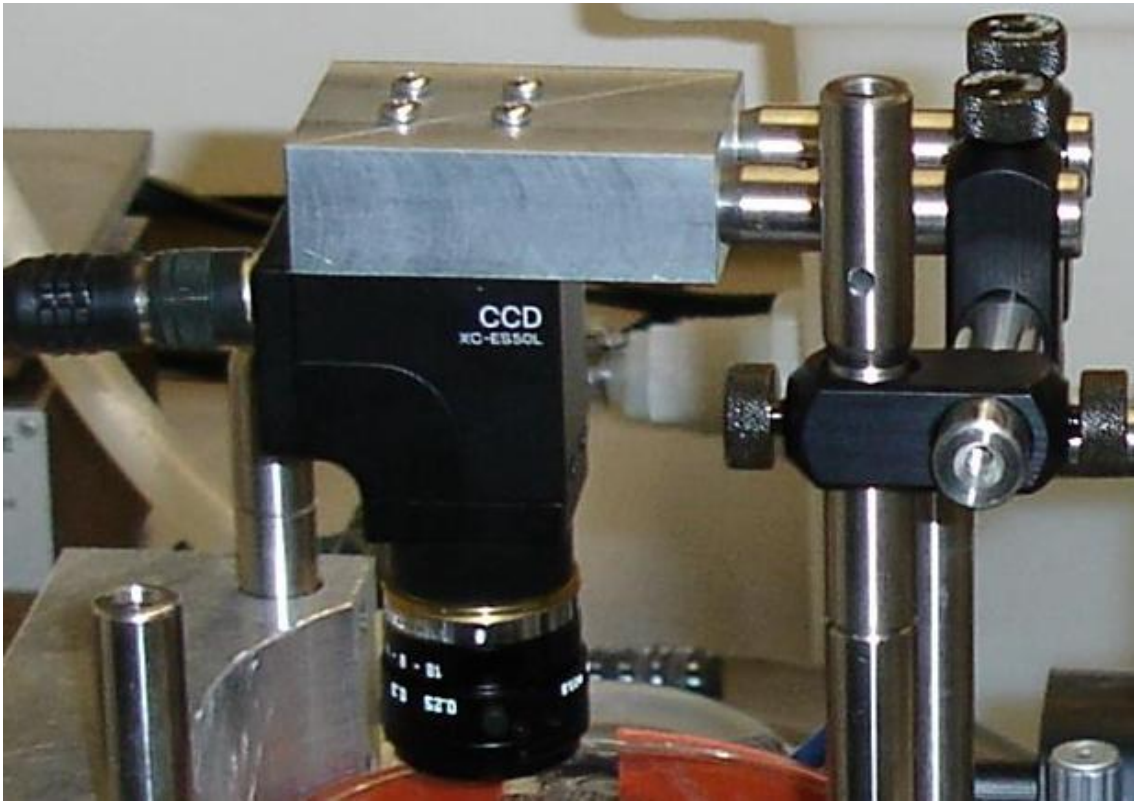


Figure 3-10: Custom designed camera mount

The DC-700/700CE from Sony is a camera adapter for all current DC operated XC cameras. The DC700/700CE supplies 13V, 1.3A. It is small, light and useful in space-limited applications. The DC-700/700CE adopts the new pin assignment of 12pin connector, which is based upon EIAJ.

It takes input from the camera through the camera cable and provides video output, which can be taken from the adapter using video cable. The trigger, horizontal drive and vertical drive signals can also be given through this adapter to the camera.

<u>Specification</u>	<u>Detail</u>
Power requirements	120V AC, 50/60 Hz

DC output	DC 13V, 1.3A
Input/Output connectors	WEN connector (BNC type) TRIG connector (BNC type) HD connector (BNC type) VD/SYBC connector (BNC type) VIDEO OUT 1 connector (BNC type) VIDEO OUT 2 connector (BNC type) CAMERA connector (BNC type)
Mass	700 g (1 lb, 8 oz)
Dimensions	110 (W) x 53 (H) x 160 (D) mm

Table 3-8: Specifications of the camera adapter

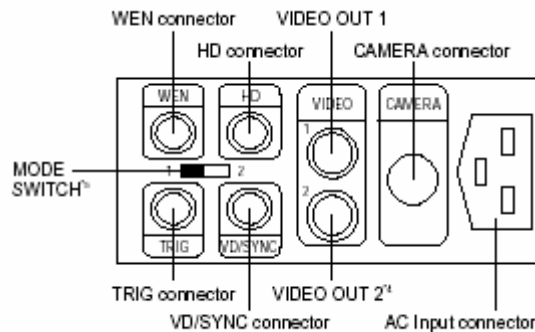


Figure 3-11: Rear panel of DC 700 adapter (courtesy Sony)

The CCXC12P02N is a 2 m long camera cable, which is used to connect the camera to the adapter. The cable has a 12-pin connector on both ends. Figure 3-12 shows the 12-pin camera connector of the cable used to connect the camera and the adapter

- #1 GND
- #2 +13V
- #3 GND
- #4 VIDEO 1
- #5 GND
- #6 HD
- #7 VD/SYNC
- #8 GND
- #9 VIDEO 2
- #10 WEN
- #11 TRIG
- #12 GND

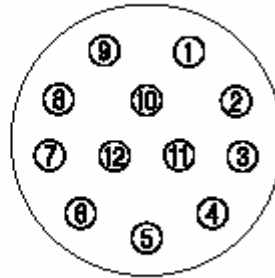


Figure 3-12: 12-pin camera connector (courtesy Sony)

vii. Camera lens

We first present the calculations performed to aid the selection of the appropriate camera lens for our requirements, before looking into the specifications of the selected lens.

The two important specifications, which play a role in the lens selection, are the desired magnification of the image and the working distance, i.e. the distance between the image and the object.

We want to obtain an image of diameter approximately 50.8mm on the condensation cell. The size of our CCD is ½". The dimensions of the sensor in a ½" CCD are shown in Figure 3-13.

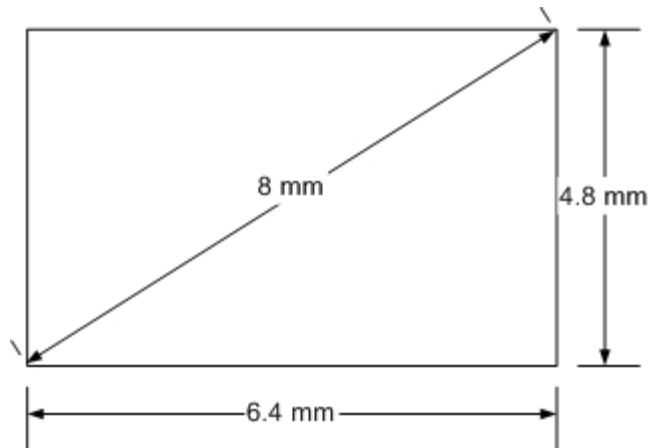


Figure 3-13: Sensor size of a ½" CCD

Consider obtaining an image of diameter 8mm corresponding to the 50.8mm diameter surface being inspected. This implies inscribing the CCD completely inside the circle without losing much information. Thus the required magnification can be calculated as explained further.

$$M = \frac{\text{Image_size}}{\text{Object_size}} = \frac{8}{50.8} = 0.157 \quad (3.4)$$

Thus, if the magnification is 0.157, then for a circle of diameter 50.8mm (2") on the condensation cell, we will obtain an image of size 8mm so as to utilize maximum CCD area.

Further, for selection of C Mount lens and spacer, we analyze the working distance of the some lenses with the available space in our system.

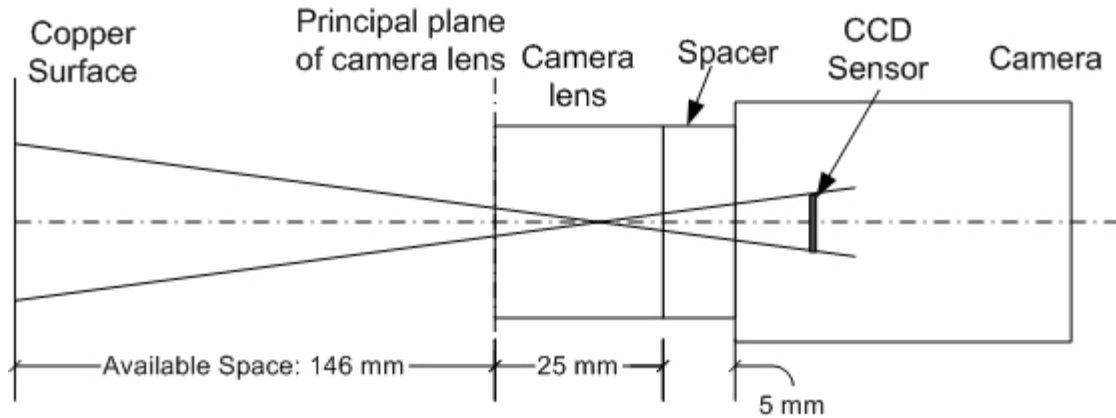


Figure 3-14: Camera lens and spacer placement

a) Let us select a lens of focal length 16mm, having a length of 25mm, and a spacer of 5mm.

The specifications of this combination are:

Working distance = 90-340mm

Horizontal field of view = 40-130mm

It is noted that the horizontal field of view is adequate for the largest image size of 50.8mm.

Magnification obtained can be calculated using Eqn. 3.5:

$$M = \frac{\text{Image_distance}}{\text{Object_distance}} \quad (3.5)$$

Thus, $M = 30/150 = 0.2$ which is a little over 0.157 and hence acceptable.

b) Now we examine a lens of focal length 25mm, having a length of 25.5mm, and a spacer of 3mm.

This specification cannot be met by any available combination of lens and spacer. However, looking at the specifications for two other spacers in combination with this lens, we conclude that the results with a spacer width lying somewhere in between these two would be most appropriate.

i) With a spacer of 1mm, the specifications are

Working distance = 250-650mm

Horizontal field of view = 62-165mm

ii) With a spacer of 5mm, the specifications are

Working distance = 88-118mm

Horizontal field of view = 24-31mm

Thus it is expected that in a range between 1mm and 5mm, say 3mm, we will be able to achieve the required working distance of 150mm and a horizontal field of view of 50.8mm.

Magnification obtained can again be calculated using Eqn. 3.5. Thus, $M = 28.5/150 = 0.19$ which is a little over 0.157 and hence acceptable. Hence, we concluded that the combination of 25mm focal length lens and 3mm spacer is most appropriate for our requirement.

The F56-529 from Edmund Industrial Optics is a C mount lens of focal length 25mm. A C mount lens is a lens in which the flange distance, which is the distance between the mechanical mount surface and the image sensor (in air), is 17.526mm. Table 3-9 presents detailed specifications of the lens.

<u>Specification</u>	<u>Detail</u>
Focal length	25mm
Aperture f/#	F1.6 -16C (C=closed)
Mount	C mount
Angular Field of View (FOV) -Horizontal	14.6°
Min. working distance	0.25mm
FOV at min. working distance	64mm
Outward dimensions	φ 30.5 x 25.5mm
Weight	40g

Table 3-9: Specifications of the camera lens

viii. Frame Grabber

The range of frame grabbers available was mostly PCI based. As the system is intended to be a portable system, we required a PCMCIA type frame grabber which can be used with the laptop used for data analysis. The two available frame grabbers of this type are MRT VideoPortProfesional and Imperx VCE-B501. Among these, the VCE-B501 from Imperx Inc. is available easily and is well supported by the manufacturer. It is required for obtaining the images captured by the camera onto the laptop. The frame grabber package includes the cable for connection to the camera adapter and also the driver software and a software development kit. Figure 3-15 shows a picture of the VCE-B501 frame grabber.



Figure 3-15: PCMCIA frame grabber (courtesy Imperx)

The salient features of the frame grabber are as below:

- PCMCIA 2.1/JEIDA 4.1 compliant
- Plug and play PCMCIA frame grabber
- Hot insertion and removal
- Two Composite and one S-Video inputs with anti-alias filters
- Adjustable image brightness, contrast, saturation and hue
- 24 bit RGB, 24 bit Grayscale or 8 bit Grayscale display options
- Image viewer with play, stop, pause, fast forward, reverse, step up, and step back options
 - Fast video capture with three standard, user selectable window sizes:
 - 640 x 480 pixels
 - 320 x 240 pixels
 - 160 x 120 pixels
 - PCMCIA frame grabber captures single frames, multiple frames and standard AVI clips:
 - Adjustable frame rates
 - Programmable capture delay up to 60 minutes
 - Programmable date and time recording

- BMP and adjustable compression JPEG file formats
- TWAIN driver
- Date and Time stamp options
- Text overlay options

The detailed specifications of the frame grabber are listed below:

<u>Specification</u>	<u>Detail</u>
Video source	Composite or S-Video Square pixel and CCIR601 resolution for NTSC, PAL and SECAM Auto NTSC/PAL format detection Automatic gain control 16 bit YcrCb (4:2:2) digital output
Operating System	Windows 95, 98, NT 4.0, ME, 2000 and XP compatible
Electrical characteristics	Operating voltage: 5V +/- 5% Operating current: 250mA Inrush current 750mA
Dimensions	PCMCIA Type II 86mm(L) x 54mm(W) x 5mm(H)
Mass	35g
Operating temperature	0° C to 65° C
Relative humidity	90% non-condensing

Table 3-10: Specifications of the frame grabber

3.2.2 Incoherent Light Fringe Projection System

As in the case of coherent light projection, the system can be logically divided into two subsystems, one responsible for the projection of fringes and the other responsible for imaging of the deformed fringe pattern. Here, the projection subsystem consists of the white light source and a Ronchi ruling. The other components in this subsystem are the optics for beam expansion and beam steering. The imaging subsystem consists of the camera, camera lens and the frame grabber as in the case of coherent light fringe projection. Figure 3-16 shows the block diagram for incoherent light fringe projection.

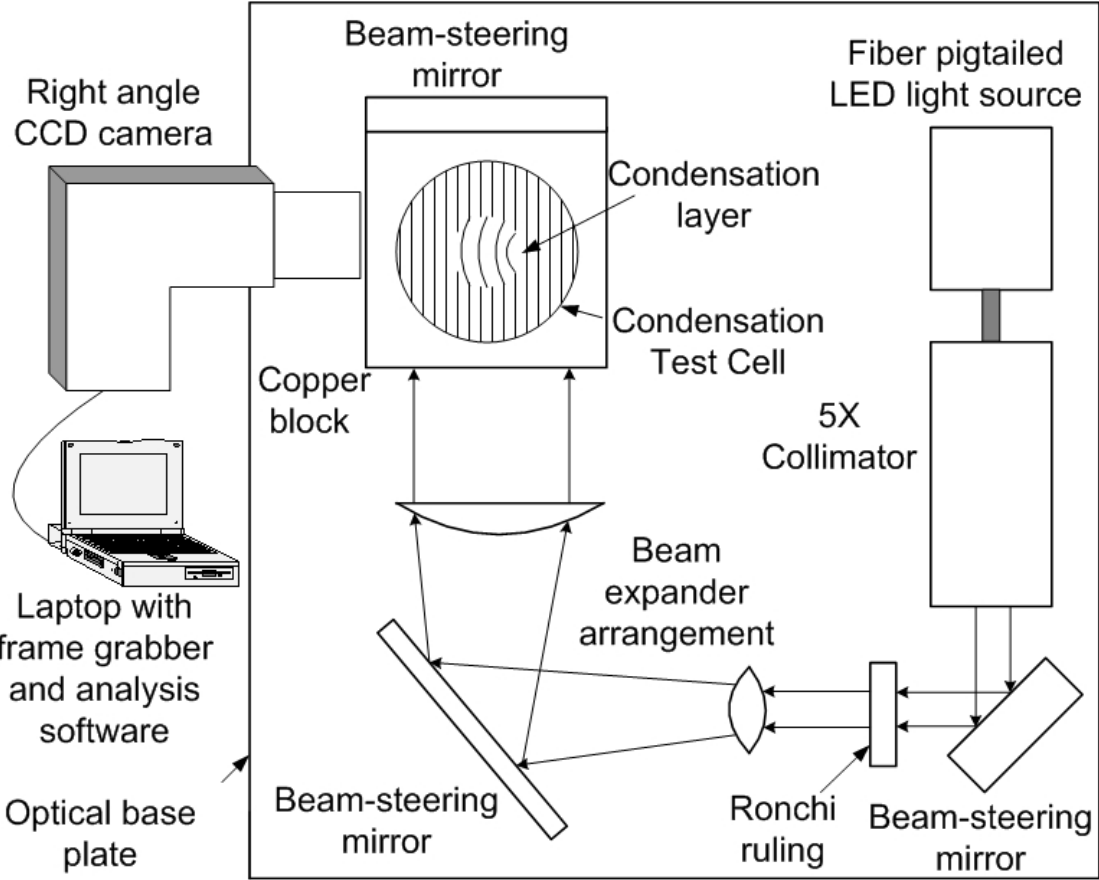


Figure 3-16: Incoherent light fringe projection system

The working of the white light based system differs from the coherent light system only in the source of light and as a consequence, in the mechanism of generation of fringes. Here, an incoherent white light source has been used for illumination. The coherent light system utilized the phenomenon of interference of the generation of fringes. Since interference produced by incoherent waves varies too rapidly in time to be practically observed, we use an alternate technique of fringe generation. In this technique, we use a commercially available Ronchi ruling that has a pattern of light and dark bands marked on it. We illuminate the ruling with the white light source and this causes the structured light pattern to be projected onto the beam expander. Beyond this step, the same process is repeated as in the case of coherent light system and eventually, the expanded pattern gets projected on the copper surface. We now explain the detailed specifications of the components of the white light fringe projection system.

i. White light source

The Fiber pigtailed Luxeon III Star single LED package from Doric Lenses Inc. is a custom made light emitting diode (LED) based light source. Many of the commercially available white light sources are devised for high power applications and thus were unsuitable for our system. Also, because of space and mounting constraints, we required a compact system, preferably with a fiber coupled output to allow easy interchange between coherent and

incoherent system. Thus, we specified our power, beam diameter, center wavelength requirements to Doric lenses and received the white light source most appropriate for the system. Figure 3-17 shows a picture of the white light source.

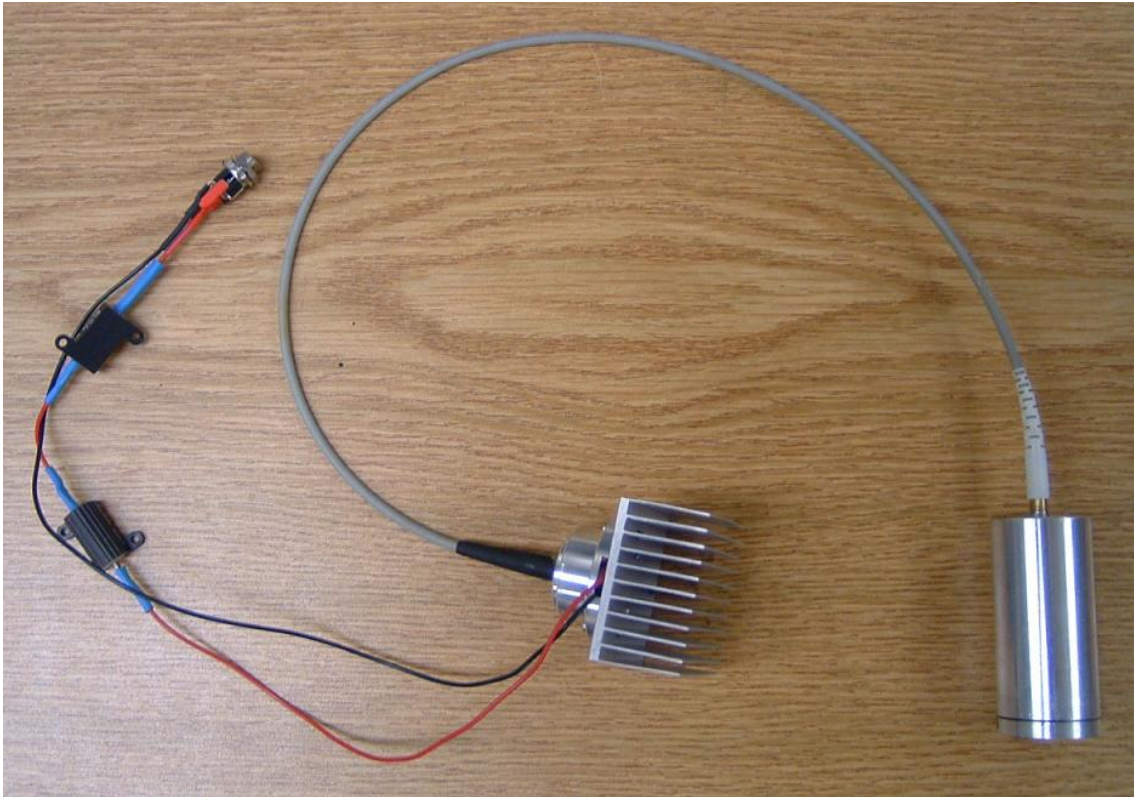


Figure 3-17: LED based white light source

The source consists of a Luxeon III star LED from Lumileds Lighting. Luxeon III is an energy efficient compact light source which combines the lifetime and reliability advantages of LEDs with the brightness of conventional lighting. The specifications of the LED are listed in Table 3-11. Lifetime for LEDs is typically defined in terms of lumen maintenance, which is the percentage of initial light output remaining after a specified period of time.

Lumileds projects that Luxeon III products will deliver, on average, 70% lumen maintenance at 50,000 hours of operation at a 700 mA forward current or 50% lumen maintenance at 20,000 hours of operation at a 1000 mA forward current.

<u>Specification</u>	<u>Detail</u>
Color	Cyan
Radiation pattern	Lambertian
Minimum radiometric power at 700mA	51.7 mW
Typical radiometric power at 700mA	64 mW
Dominant Wavelength (typical)	505 nm
Spectral half-width	30 nm
Forward voltage at 700mA (typical)	3.70 V
DC forward current (maximum)	1000 mA
Average forward current (maximum)	1000 mA
LED junction temperature (maximum)	135°C
Storage and operating temperature	- 40°C to 120°C

Table 3-11: Specifications of the Luxeon LED

The beam output from the fiber goes into a 5X collimator, also provided by Doric lenses. This gives a beam output diameter of 10mm as desired. To meet the voltage and current specifications of the LED, we chose a DC supply of 5V and connected it to the LED in series with two 1 Ω resistors. The resistors chosen are power resistors with a rating of 10W. With this arrangement, the voltage across the LED is 3.63V and current through it is 0.61A. It was found that even when the voltage and current across the LED were within specified limits, the heat dissipation across the LED was substantial. Aluminum housing

was designed to contain the resistor arrangement and also to act as a heat sink for the LED.

ii. Ronchi ruling

High precision Ronchi ruling glass targets are excellent for evaluating resolution, field distortion etc. In our application, we are using a Ronchi ruling to project a structured light pattern on the copper surface. We have selected model F56597 from Edmund Industrial Optics, which has 300 lines per inch. The number of lines per inch required was determined experimentally from the coherent light fringe projection system, based on which fringe density gave optimum results.

<u>Specification</u>	<u>Detail</u>
Substrate	Soda lime glass
Lines per inch	300
Thickness	1.5 mm
Dimensions	1"x1"
Coating	Vacuum deposited chrome OD>3.0
Surface flatness	1 wave per inch
Surface quality	60-40
Parallelism of pattern to substrate	$\pm 1^\circ$
Line to line parallelism	≤ 2 arc sec.
Dimensional tolerance	$\pm 0.02''$

Table 3-12: Specifications of the Ronchi ruling

iii. Beam expander

The beam expander arrangement remains same as in the coherent light fringe projection system. Refer to section 3.2.1(iv) of this chapter for details.

iv. Beam steering mirrors

The beam steering mirrors are the same as in the coherent light fringe projection system. Refer to section 3.2.1(v) of this chapter for details.

v. Camera

The camera and camera adapter are the same as in the coherent light fringe projection system. Refer to section 3.2.1(vi) of this chapter for details.

vi. Camera lens

The camera lens chosen is the same as in the coherent light fringe projection system. Refer to section 3.2.1(vii) of this chapter for details.

vii. Frame grabber

The frame grabber is the same as in the coherent light fringe projection system. Refer to section 3.2.1(viii) of this chapter for details.

3.3 Condensation Cell

To study the progress of condensation using our system, it was essential to create a cell where the phenomenon of condensation can be reproduced. This required the design of a chamber in which this process can be carried out,

in addition to equipment for generating vapor and cooling equipment for cooling down the copper surface.

The chamber of the condensation cell was custom made by G. Finkenbeiner Inc. It is a Pyrex cylinder, 170mm high, and 100mm in diameter. It has one open end (the bottom) and one closed end made from optically-flat glass plate which has been fused on. The chamber has two vapor ports, which accept 1/2 inch tubing. Figure 3-18 shows a schematic of the condensation cell.

To prevent condensation from forming on the inner walls of the chamber, and thus interrupting the optical path for measurement of condensation patterns on the condensation surface, strips of heating tape have been attached to the outside of the chamber. This allows the temperature of the Pyrex to be raised above the dew-point. The power applied to the heating elements is adjusted using a variable transformer to adjust the AC voltage between 0V and 120V. Typical voltage applied is around 80V.

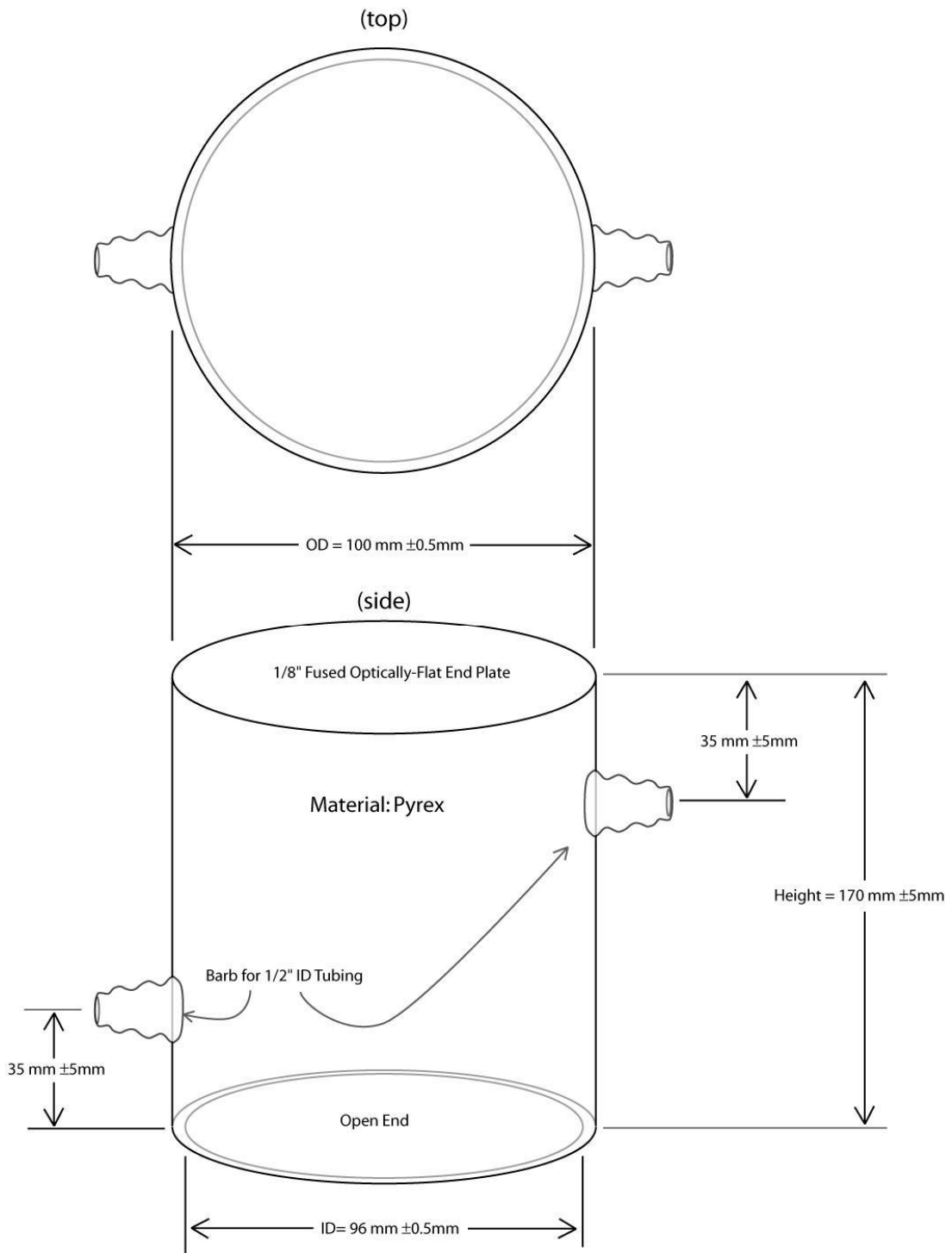


Figure 3-18: Condensation chamber

The surface on which the vapor condenses was chosen to be a copper block, due to its high thermal conductivity. To facilitate the condensation on this surface, 4 hollow channels were drilled through this block, which allow cold water to be circulated in order to cool the block. In addition, a circular groove was also machined out on the top surface of the block, which allows the condensation chamber to fit securely on the block. The ends of the cooling channels were fitted with brass fittings to allow 1/4 inch tubing to be connected to each port. Using a water pump (Model: Quiet One 1200 from Pentair Aquatics), ice water from a 3 gallon plastic tank is circulated through these channels via vinyl tubing, and fittings, which allow the flow from the pump to be split between the four channels.

Vapor is produced by heating water in a flask atop a hot-plate. The output of the flask is attached to the condensation chamber's upper vapor port. Flow of the vapor is aided by small air pump (Model: Tetrathec AP100), which pumps air into the flask at an adjustable rate. The vapor exits the condensation chamber via the lower vapor port, and a short length of hose.

Three temperature sensors monitor the state of the system. One is located underneath the copper block, and is thermally coupled to the block using thermally conductive silicon compound. The other two temperature sensors are located near the vapor inlet and outlet ports, to allow the temperature inside the chamber to be estimated.

Figure 3-19 shows a schematic of the entire condensation cell with the details of the condensation cell, the vapor production system, and the cooling infrastructure.

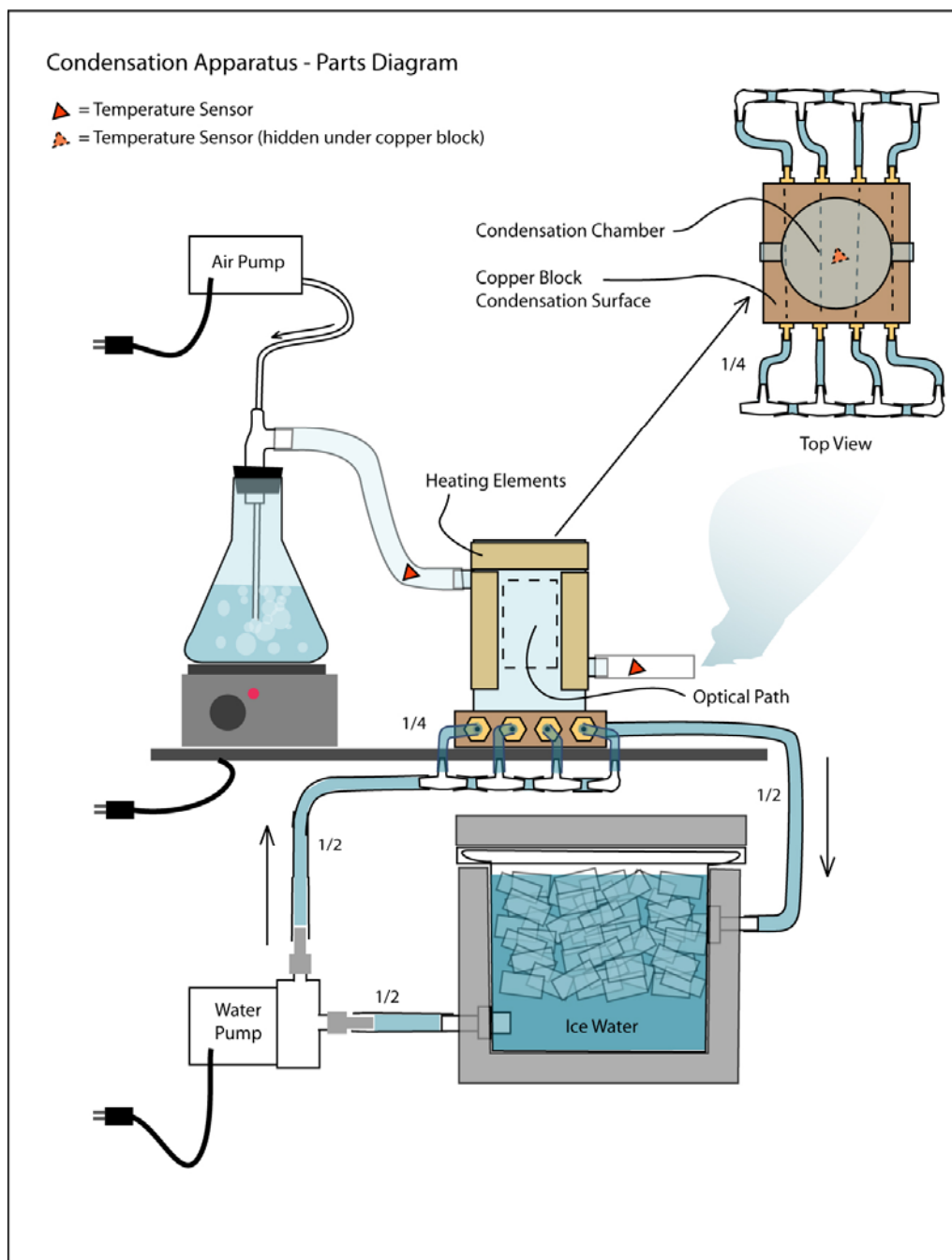


Figure 3-19: Schematic of the condensation cell

Figure 3-20 shows a photo of the current system highlighting the integration of the condensation cell in the entire system.

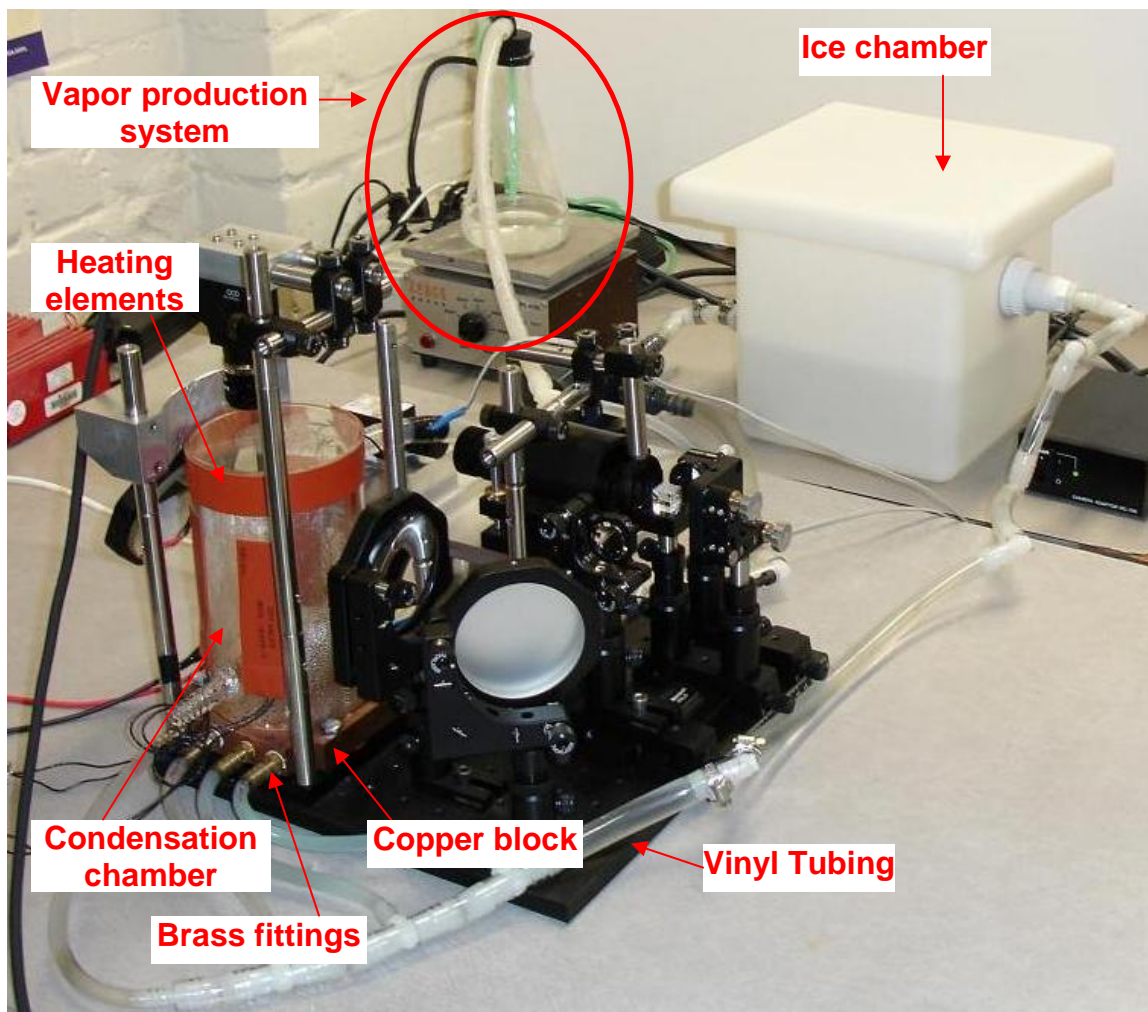


Figure 3-20: Integration of the condensation cell with the optical system

Chapter 4: Software

The software for the optical measurement system can be classified in two groups:

1. Data Capture software
2. Analysis software.

The following sections present the details of each of the two groups.

4.1 Data Capture Software

The data capture software performs two major functions:

1. Capturing the fringe pattern image data with careful control of the timing and duration of capture.
2. Capturing the temperature information from the vapor inlet port, copper block and vapor outlet port of the system.

Image data is captured from the frame grabber using a software interface for the frame grabber. This software interface has been built using the software development kit received with the frame grabber.

To track the temperatures of the condensing surface and the vapor in the system, three representative locations are monitored with three temperature sensors. These locations are: a) Vapor inlet port b) Center of the copper plate

and c) Vapor outlet port. Figure 3-19 in Chapter 3 illustrated these locations. Dallas Semiconductor/Maxim provides a technology called 1-Wire[®], that uses a single wire (plus ground) to accomplish both communication and power transmission. 1-Wire technology based temperature sensors (DS18S20) have been utilized at the three locations.

The DS18S20 digital thermometer provides 9-bit degree Celsius temperature measurements and has an alarm function with nonvolatile user-programmable upper and lower trigger points. It has an operating temperature range of -55°C to +125°C and is accurate to $\pm 0.5^\circ\text{C}$ over the range of -10°C to +85°C. In addition, the DS18S20 can derive power directly from the data line ("parasite power"), eliminating the need for an external power supply.

The 1-Wire network is a low-cost bus based on a PC or microcontroller communicating digitally over twisted-pair cable with 1-Wire components. A 1-Wire network-based system consists of three main elements:

1. A bus master (DS9490R in our case) with controlling software such as the TMEX[™] iButton[®] viewer. The iButton[®] viewer is a Windows program for communicating with 1-Wire Net compatible 1-Wire devices. It integrates most of the iButton-TMEX utilities in a single, user-friendly piece of software.
2. Wiring and associated connectors, and
3. 1-Wire devices (DS1820 in our system).

An important aspect of this technology is that every 1-Wire device has a globally unique digital address, also known as its 'ROM code'. This code can be

determined using the TMEX™ iButton® viewer, capable of controlling any 1-Wire device.

The data capture software has essentially been divided into several smaller modules which interact to perform the above two functions. Figure 4-1 presents a block diagram of the software modules showing their interaction to perform various functions, which is followed by details of all the major modules. Appendix C includes the code for the MATLAB scripts *FCap.m* and *UpdateMain.m*:

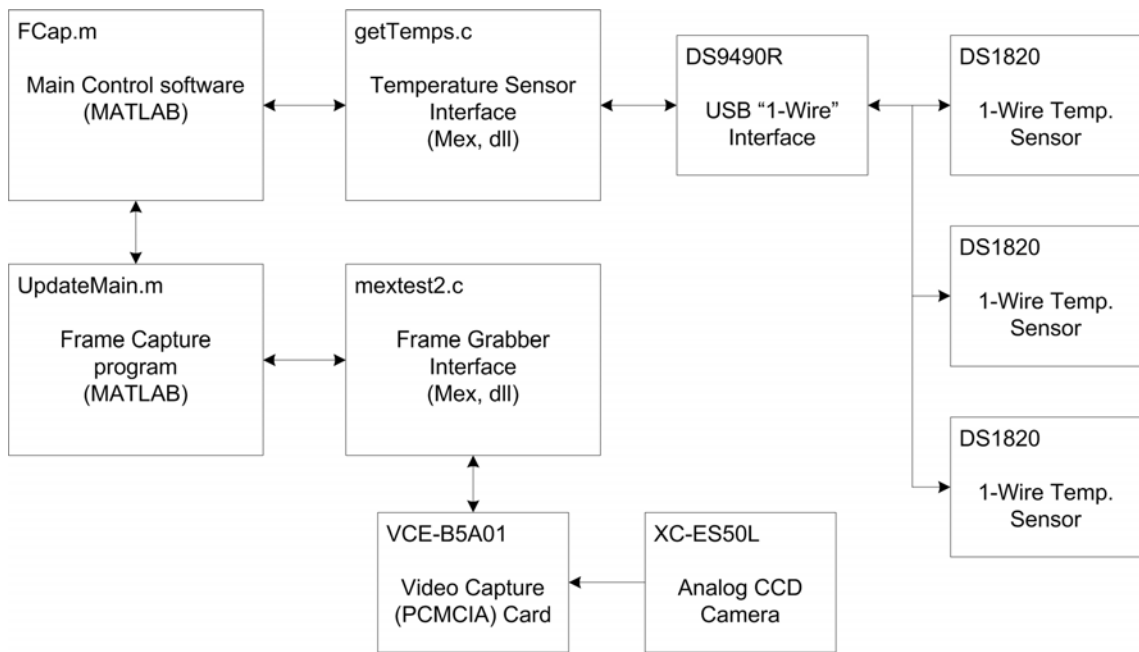


Figure 4-1: Block diagram of data capture software

4.1.1 Main Control script

The process of capturing the image frames and temperature data is controlled using a MATLAB script, *FCap.m*. This file essentially displays the graphical user interface, which consists of:

- a) An image display area
- b) Buttons for updating the image and adjusting the horizontal offset of the active CCD area (i.e. panning control),
- c) A button for starting a timed capture sequence (Movie) alongside an input text box for specifying the desired capture duration
- d) A plot of the gathered temperature data.

A screenshot of the user interface is shown in Figure 4-2:

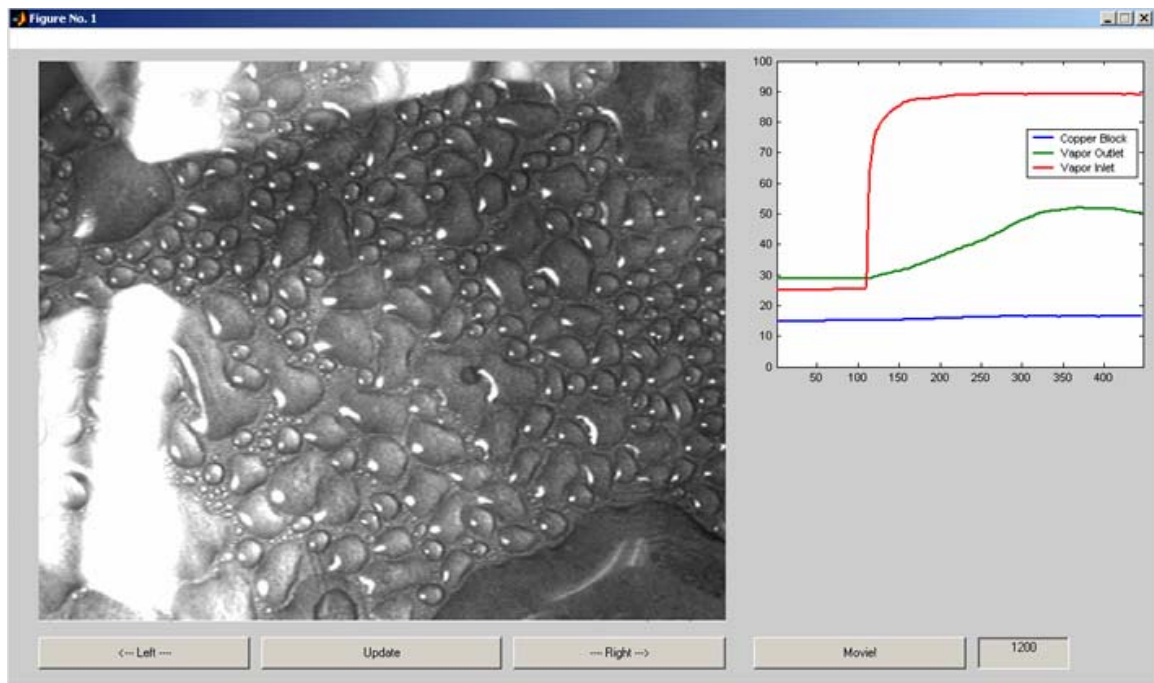


Figure 4-2: Graphical user interface displayed by the control script

Figure 4-3 presents a flowchart of the structure of the 'FCap.m' script.

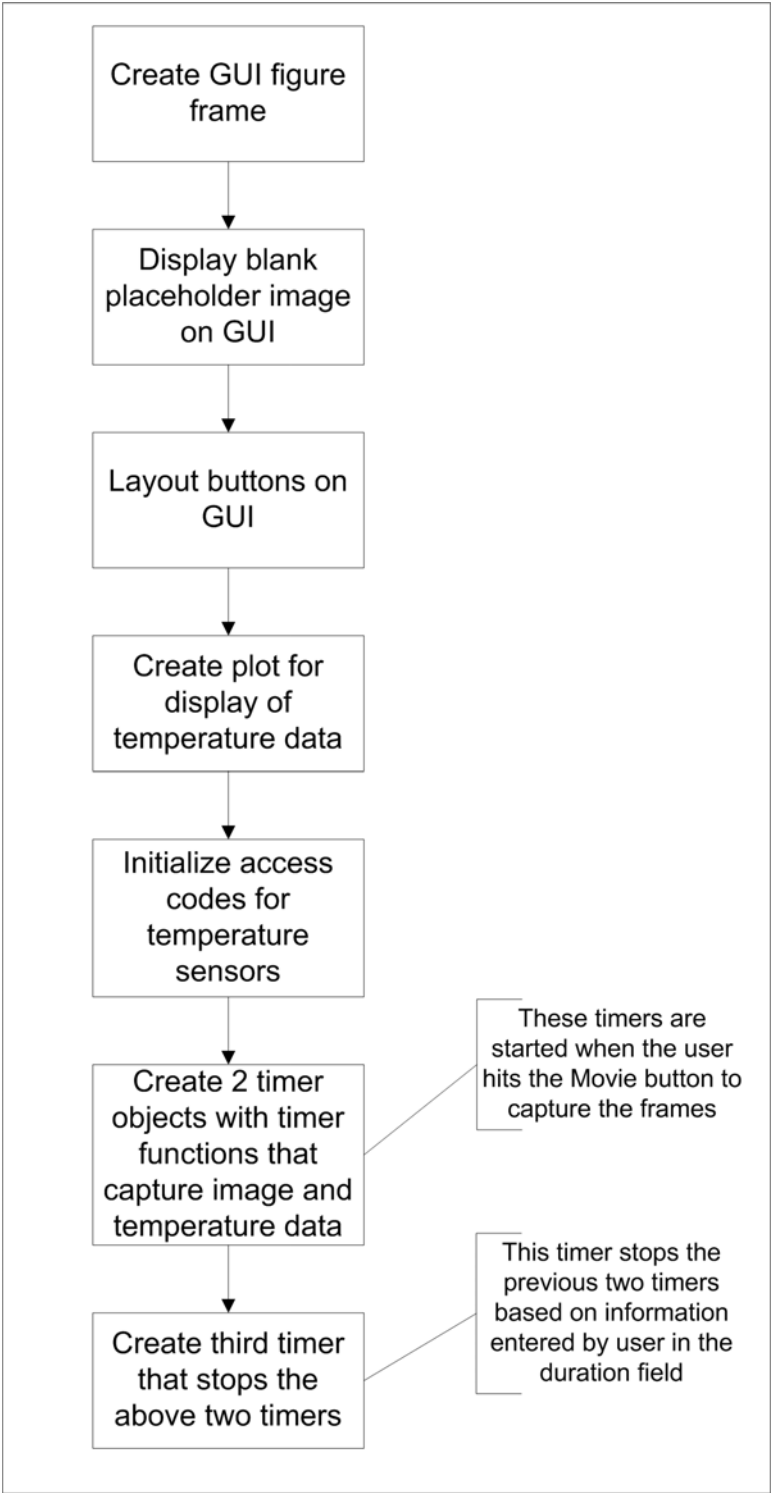


Figure 4-3: Flowchart of the MATLAB script *FCap.m*

The script passes control to the different sub-modules to perform individual functions, based on the inputs received from the graphical user interface.

The frame capture time for each frame is 1.5 seconds. Faster rates cause errors, because background frame grabber processes are interrupted mid-stream. As indicated in the flowchart, timer objects are utilized to coordinate the capture of sequential image frames and the corresponding temperature data and also for displaying the frames and for plotting the temperature data. The timer object represents the timer in MATLAB. The timer object supports properties that lets one specify the MATLAB commands that execute when a timer fires, and for other timer object events, such as starting, stopping, or when an error occurs. These are called callbacks. The timer object supports several execution modes that determine how it schedules the timer callback function (TimerFcn) for execution. The three timer objects used in the system are explained below:

- a) T_c : The timer for starting a temperature capture. This timer sends a signal to the temperature sensors through the *getTemps.c* program, and the 1-Wire interface. The signal sent through the program causes the temperature sensors to start their temperature capture process, which takes approximately 750ms.
- b) T_r : The timer for retrieving temperature data. This timer has the same period as T_c , but is offset by 750ms. It is responsible for

gathering the temperature data from the three sensors. This is also done through the *getTemps.c* program and the 1-Wire interface.

- c) *Ts*: The timer for stopping capture process. This timer uses the user-specified frame duration, to assert the length of the capture sequence. Its action is to stop the other two timers, *Tr* and *Tc*.

Image frames are automatically saved to the hard drive (in `.\frames` folder as they are collected). This is accomplished in the *UpdateMain.m* function. An additional utility called *compilemovie.m* has been developed and provided which can be used to create an AVI file from the collected frames. The compilation procedure is processor-intensive and can take quite a while, depending on the number of frames. Due to this reason, the decision of movie creation has been kept optional rather than being standardized.

4.1.2 Temperature Sensor Interface

The *getTemps* program uses the DS9490R 1-Wire interface to control the three temperature sensors. Each sensor's ROM code is hard-coded into the main control script, *FCap.m*.

The *getTemps* program is a C MEX file. MATLAB provides a way to call our own C subroutines from MATLAB as if they were built-in functions. MATLAB-callable C programs are referred to as MEX-files. MEX-files are dynamically linked subroutines that the MATLAB interpreter can automatically load and execute. Bottleneck computations (usually for-loops) that do not run

fast enough in MATLAB or special applications which have interfaces available through only limited programming languages (such as C in our case) can be coded in C as MEX-files for efficiency.

The *getTemps* program accepts two input parameters. The first is either a 1 or a 0. This parameter specifies the desired command. An input of 0, which stands for restart, causes the all of the temperature sensors to start a new capture process. A 1 input, which stands for read, allows the temperature of an individual sensor to be read. The second parameter allows the user to specify which device will be accessed (using the aforementioned ROM codes), given that the first parameter is 1. If the first parameter is 0, then the second parameter is not required and can be set to 0.

4.1.3 Frame Capture Script

The function *UpdateMain.m* is responsible for triggering a frame grab, updating the image display area, and saving the frame to the hard drive. It accepts the following parameters:

- i. *axMain* – the handle to the image display area axes
- ii. *xoff* – the x-offset of the CCD image capture area
- iii. *xact* – the width of the CCD image capture area
- iv. *yoff* – the y-offset of the CCD image capture area
- v. *yact* – the height of the CCD image capture area
- vi. *f* – the current frame number

The handle “axMain” is used to update the image axes with the last captured image frame. The parameters “xoff” and “yoff” are used to set the offset of the image display area from the left bottom corner of the graphical user interface. These two parameters are also controllable by the user by means of the push buttons labeled “left” and “right” on the GUI. Parameters “xact” and “yact” represent the x and y dimensions of the image captured. These parameters have been set to the maximum image size that can be captured using the frame grabber (“xact” equals 640, and “yact” equals 480). The parameter “f” is used to keep track of the current frame number being captured.

The function calls the *mextest2* program, which is also a C MEX file, to capture one frame. It then retrieves the image data and reshapes the frame as per the specifications (640x480) and displays the image on the image display axes. Finally, it writes the frame to the hard drive as a BMP (bitmap) file and returns to the calling program.

4.1.4 Frame Grabber Interface

This program is responsible for the actual frame capture from the frame grabber. Frame data is captured using this frame grabber interface that accesses the VCE-B5A01 PCMCIA video capture card. The software performs all the steps to configure the frame grabber as per the desired settings of frame dimensions and capture modes. It accesses the low level input output routines for the frame grabber to initialize the frame grabber and direct it to capture a frame from the camera. The program returns frame data in the form of a

1x614400 array, containing three 640x480 frames worth of pixels. Since the camera is grayscale, each of the three frames is identical.

4.2 Analysis Software

4.2.1 Signal Processing Steps

The deformed fringe patterns captured by the control software need to be analyzed to reconstruct surface information of the condensation film from the data. As mentioned in Chapter 2, Fourier transform based fringe analysis technique has been selected in the current research. The Fourier transformed and processed images are then subjected to phase unwrapping to yield the surface information. The algorithm for the complete Fourier transform analysis is as follows:

1. Compute Fourier transform of image
2. Perform filtering to isolate the upper side lobe (positive spatial frequency)
3. Take inverse Fourier transform of filtered image
4. Compute wrapped phase as $\arctan(\text{imaginary part}/\text{real part})$
5. $\text{Unwrap}(\text{Deformed wrapped phase} - \text{Reference wrapped phase})$
6. Calibrate recovered phase to obtain surface height information.

Steps one to three of this algorithm are equivalent to computing the analytic signal for the captured fringe pattern image. These steps were

explained analytically in section 2.6 and illustrated in detail in Figures 2-11 (a) through (h).

Steps one to four are simple and it was easily possible to implement these steps using MATLAB and/or C. However, the unwrapping process is extremely critical and frequently unstable and requires detailed understanding of the phase unwrapping algorithms. Thus, it was decided to purchase some reliable and well-tested software which can perform all analysis functions in a single package.

The available options for the analysis software that were investigated are listed below.

1. *FringeProcessor*: A software tool developed by BIAS, an institute for applied laser technology in Germany. This program has the capability of analyzing interferograms using a variety of techniques including the Fourier transform method. This is state-of-the-art software which has implemented industry standard algorithms for different analysis techniques.
2. *PXHolo*: A software tool developed by Dr. Cosme Furlong of the Mechanical Engineering Department of WPI. This software also has the required functionality of Fourier transform analysis and phase unwrapping. The tool is written in IDE, a language unfamiliar to the author of this thesis. Thus, it was concluded that this will be a hindrance to program further during the implementation of filtering of captured images.

3. *FRAN*: This Fringe analysis software developed at the University of Warwick is available free for non-commercial use. *FRAN* can separate the phase information from a single finite fringe interferogram, using the Fourier Transform method, or from three uniformly phase shifted finite or infinite fringe images using the phase stepping method. The resulting wrapped map can be unwrapped using either simple fringe counting or minimum spanning tree approach. In addition to this, externally produced wrapped phase maps can be unwrapped into a continuous surface. The main reason for not selecting this software was the lack of any technical support that might be required in the course of analysis. Another important criterion was the absence of information regarding the stability and reliability of its algorithms.

Thus, considering all the factors described above, it was concluded that *FringeProcessor* was clearly the best choice for our application. The following section presents additional details and highlights of the *FringeProcessor* software.

4.2.2 FringeProcessor

The Fringe Processor is a software tool for fringe evaluation and scientific image processing. It is developed by *Bremer Institut für Angewandte Strahltechnik* (BIAS), an institute for applied laser technology, located near the

University of Bremen in Germany. Some of the key features of this software are listed below:

- Windows 9x, NT 4, 2000, XP software for automatic processing of fringe patterns.
- Analysis of interferograms using Phase Shifting Interferometry, Fringe Tracking, Fourier Transform Method and Carrier Frequency Method.
- Simulation of interferograms.
- Integrated state of the art applications like Shearography, Digital Speckle Photography, Digital Holography and 3D Displacement Analysis.
- Other image-processing procedures for improvement, segmentation, analysis, basic mathematical operations and high-end visualization of images.
- Ability to add one's own image-processing algorithms to the system by using their software development kit (SDK).
- Integrated interpreter allows the recording and building of simple procedures.

The task to be solved in fringe analysis can be defined as the conversion of the fringe pattern into a continuous phase map taking into account the quasi sinusoidal character of the intensity distribution. The FringeProcessor is a Windows based software system with 32 bit performance. A main feature of FringeProcessor is that the exchange of results between the software and the

real world (e.g. frame grabber) works only offline via image and data files. This makes it easy to use the system in varying hardware environments without extensive adaptations. Figure 4-4 below shows a screenshot of the software interface in operation.

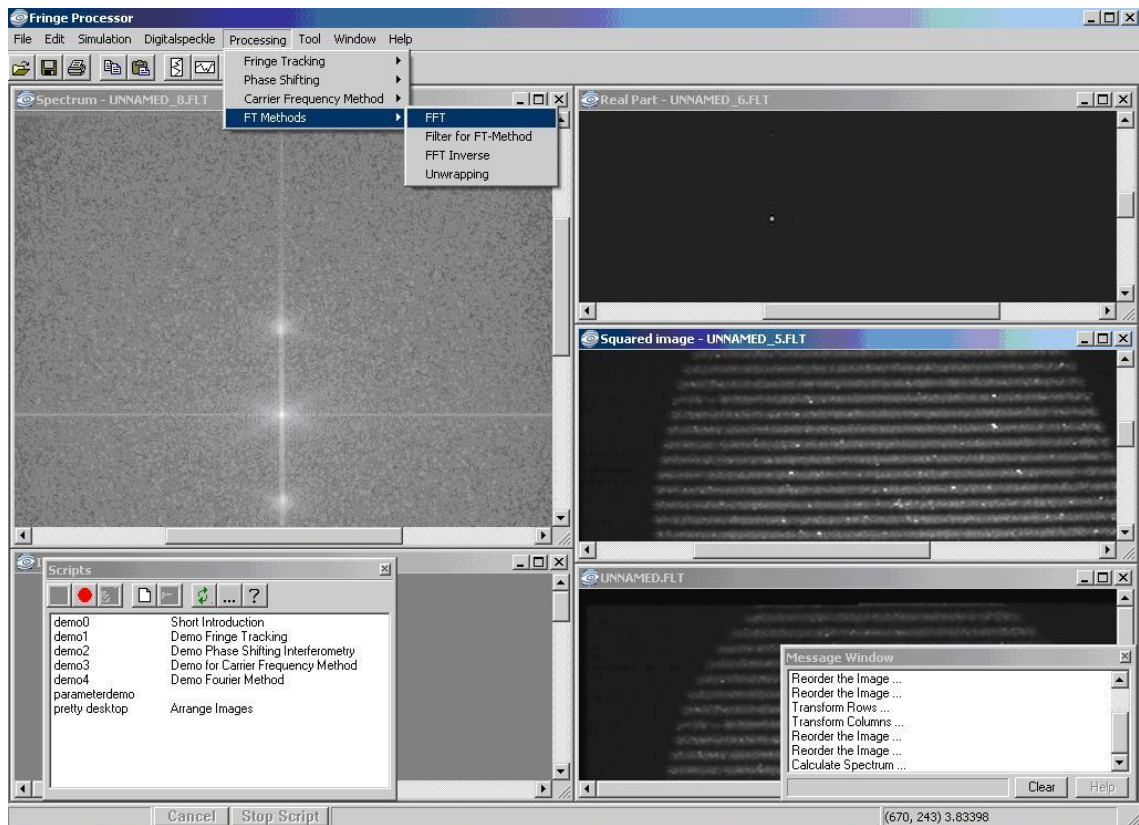


Figure 4-4: Application interface of the FringeProcessor

With respect to the processing capability, the FringeProcessor offers three ways of processing fringe patterns:

- a) Simulation: Allows the user to simulate the complete fringe formation process.
- b) Processing: Provides the most important fringe processing procedures.

c) Tool Box: Delivers typical processing tools separately.

The processing mode is the central part of the system as it contains the most known fringe evaluation procedures with their sequence of processing steps. The FringeProcessor offers the following basic fringe analysis techniques:

- 1) Fringe Tracking or Skeleton method
- 2) Phase-sampling or Phase-Shifting method
- 3) Fourier-Transform method and
- 4) Carrier-Frequency method

Further, the following two algorithms have been implemented for phase unwrapping:

- 1) Minimum phase difference spanning tree and
- 2) Maximum cross amplitude spanning tree

The difference between both the algorithms is how they define the criteria to walk through the wrapped phase map. The minimum phase difference spanning tree uses the phase difference between the central pixel and its neighbors and chooses the way with the least difference. On the other hand, the maximum cross amplitude spanning tree uses the amplitude of each pixel as the criteria to walk through the phase map. The minimum phase difference spanning tree algorithm has been recommended and implemented for Fourier transform method and is used in the fringe analysis in this research.

Chapter 5: Experimental Work and Results

5.1 Non-Fluid Experiments

In this set of experiments, three objects of known and measurable dimensions were chosen. These objects included a penny, a metallic washer and a rectangular glass slide. The specific reason for including a glass slide was that the results obtained with images of the glass block would be similar to the results expected with a water film as their refractive indices are reasonably close (refractive index of glass is 1.52 and water is 1.332). These initial experiments were done to validate the working of the system.

The first lesson learnt from these experiments was that the reflections from the copper surface added a significant amount of noise, despite the fact that the reference image was subtracted from the deformed image.

The surface of the copper block was then sandblasted to reduce the effects of speckle noise. Sandblasting is a generic term for the process of smoothing, shaping and cleaning a hard surface by forcing solid particles across that surface at high speeds. Sandblasting can occur naturally, usually as a result of the particles blown by the wind, or artificially, using compressed air.

The experiments were repeated after sandblasting and the noise in images was significantly reduced, though not eliminated. Presented below are

the captured images and illustration of one set of images through the analysis process:

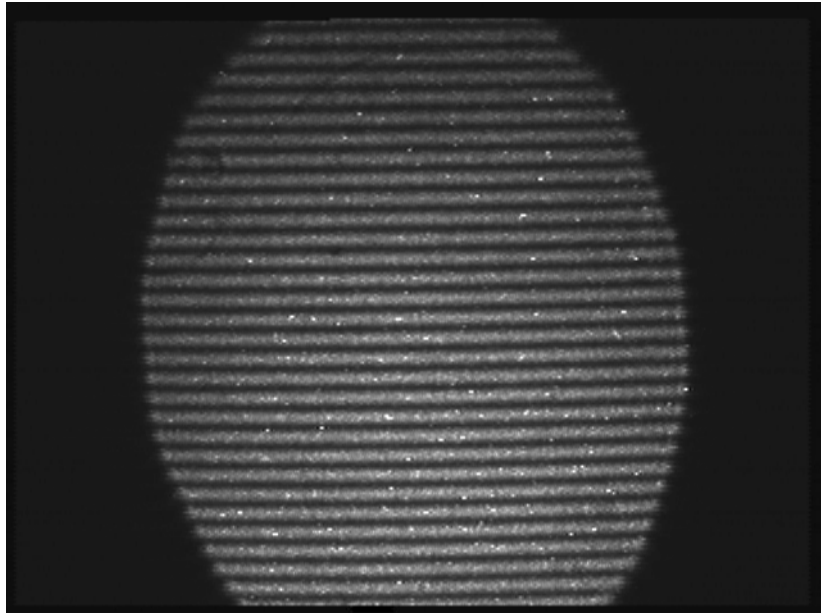


Figure 5-1: Fringe pattern on reference copper surface

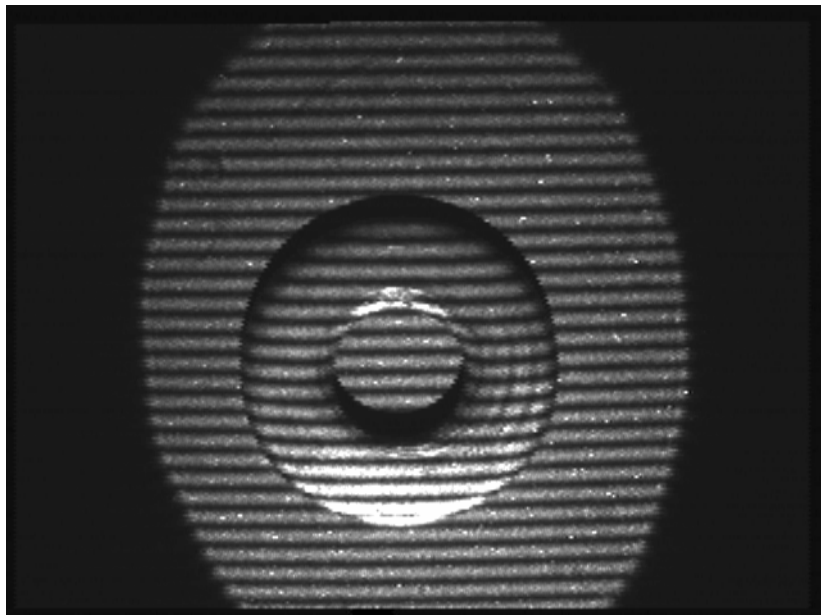


Figure 5-2: Deformed fringe pattern with a metal washer on the copper surface

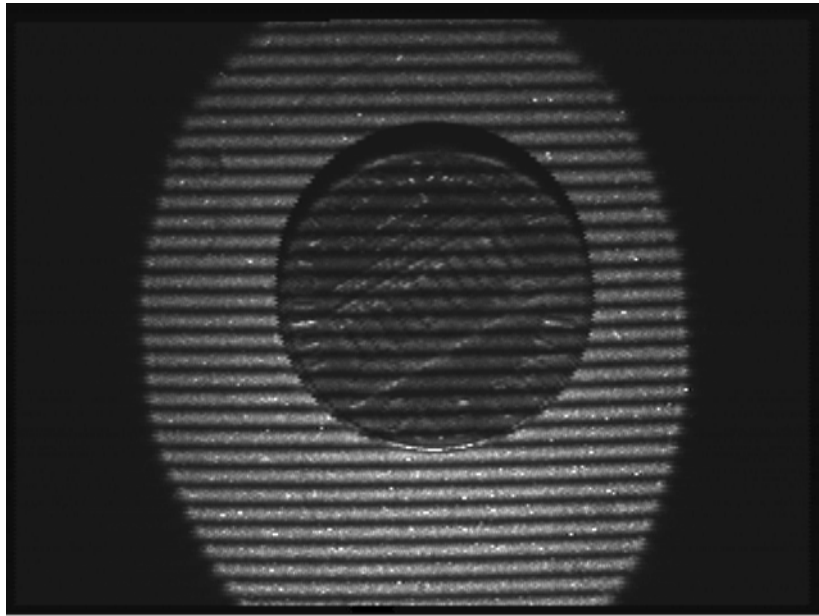


Figure 5-3: Deformed fringe pattern with a penny on the copper surface

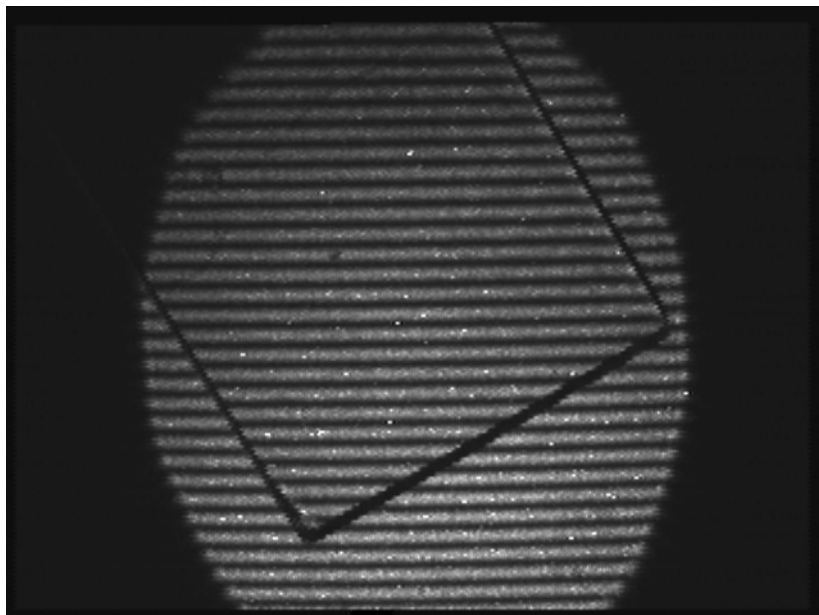


Figure 5-4: Deformed fringe pattern with a glass slide on the copper surface

As explained in the algorithm in Chapter 4, these images were then processed using Fourier transform analysis. This involved taking the Fourier transforms of these images, filtering the transform to isolate the upper side lobe,

taking the inverse Fourier transform of the filtered image and finally computing the wrapped phase information. It must be noted that the Fourier transform was taken only after resizing the original image to size 1024x1024 and hence the resultant images are much larger in size than the original images. For the same reason, the information of interest lies in the center portion of these images. The following four images show the wrapped phase for the above set of images.

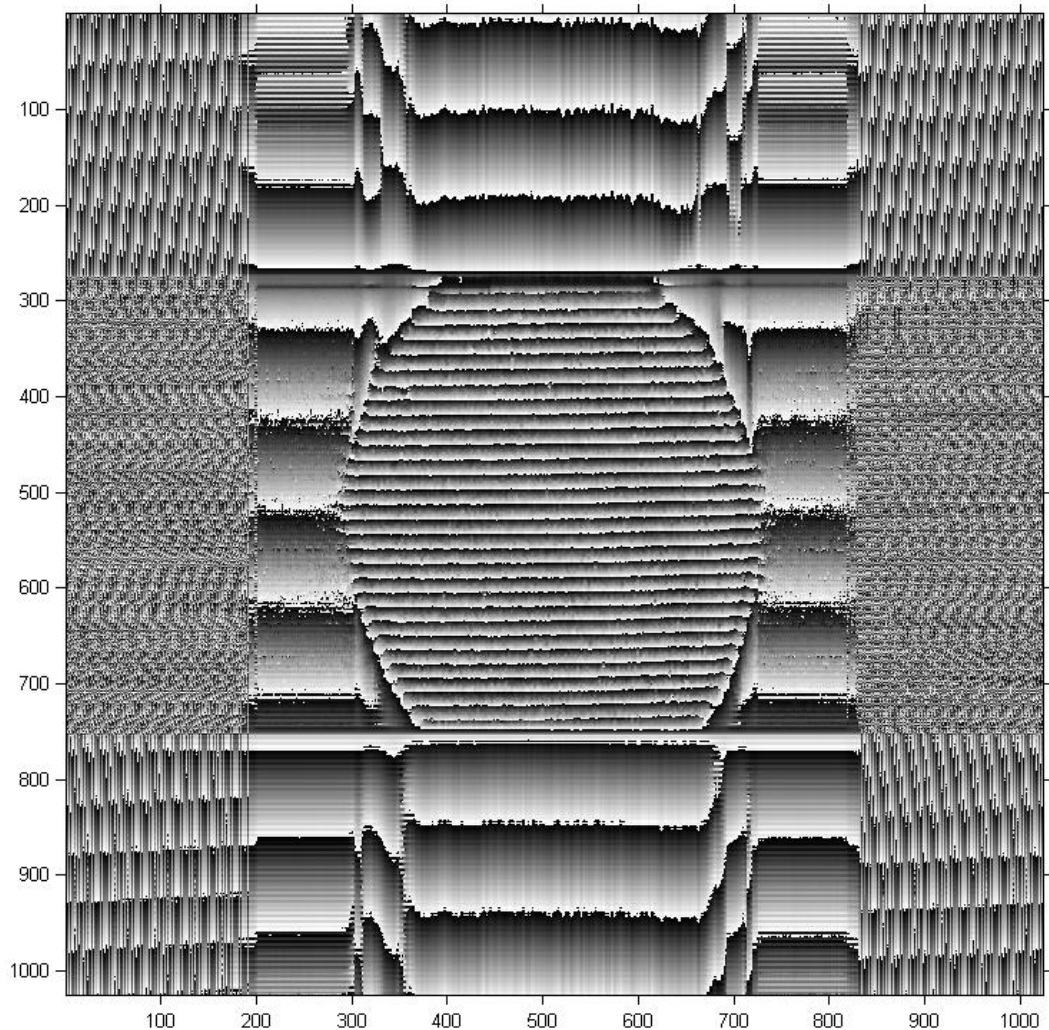


Figure 5-5: Wrapped phase for reference copper surface

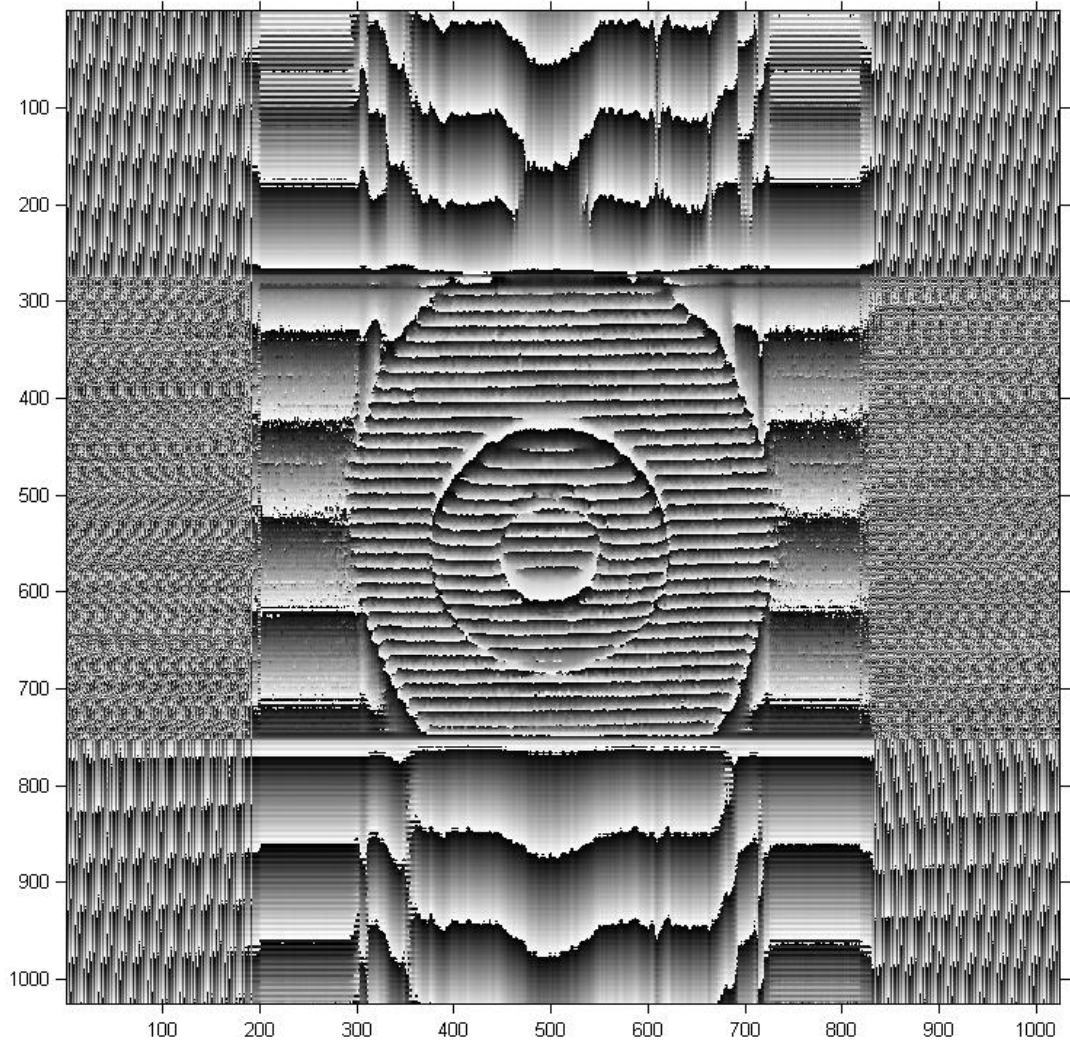


Figure 5-6: Wrapped phase for the metal washer on the copper surface

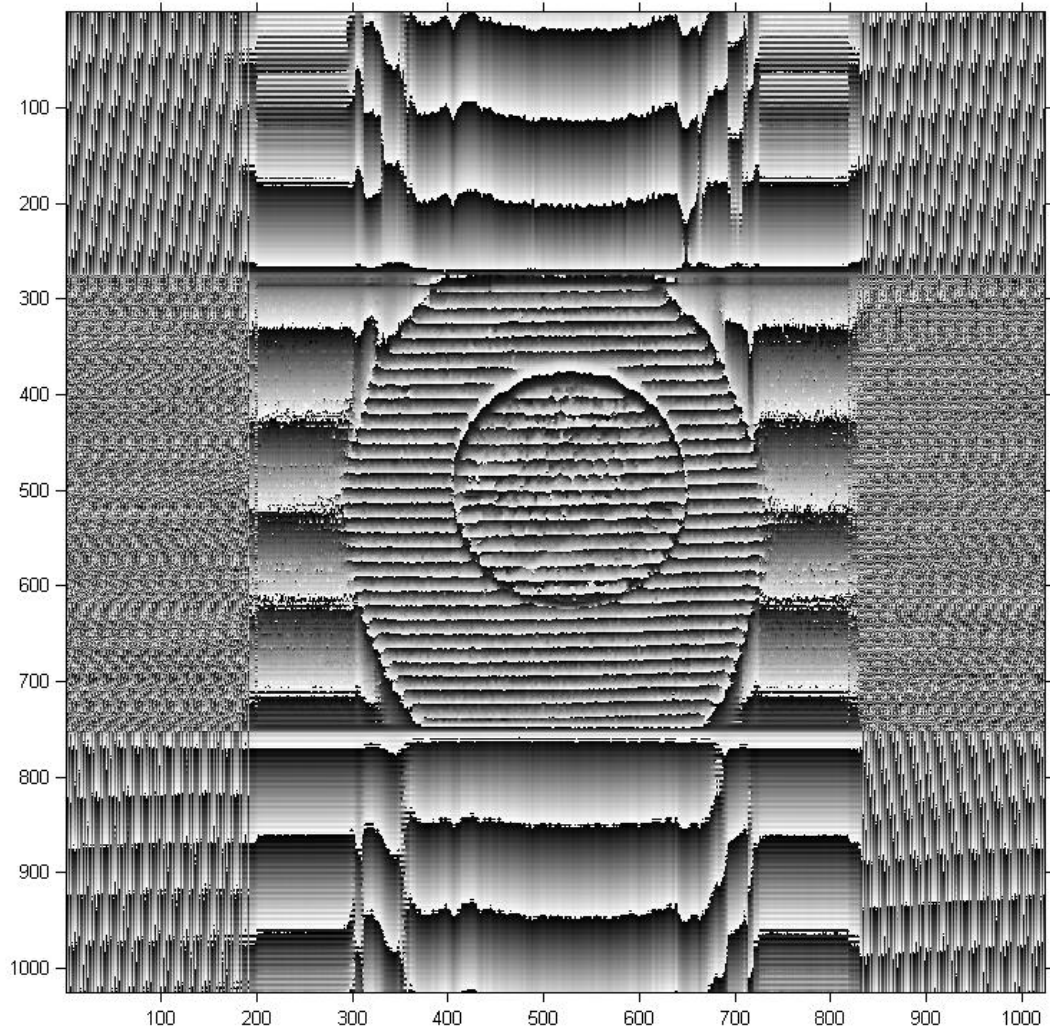


Figure 5-7: Wrapped phase for the penny on the copper surface

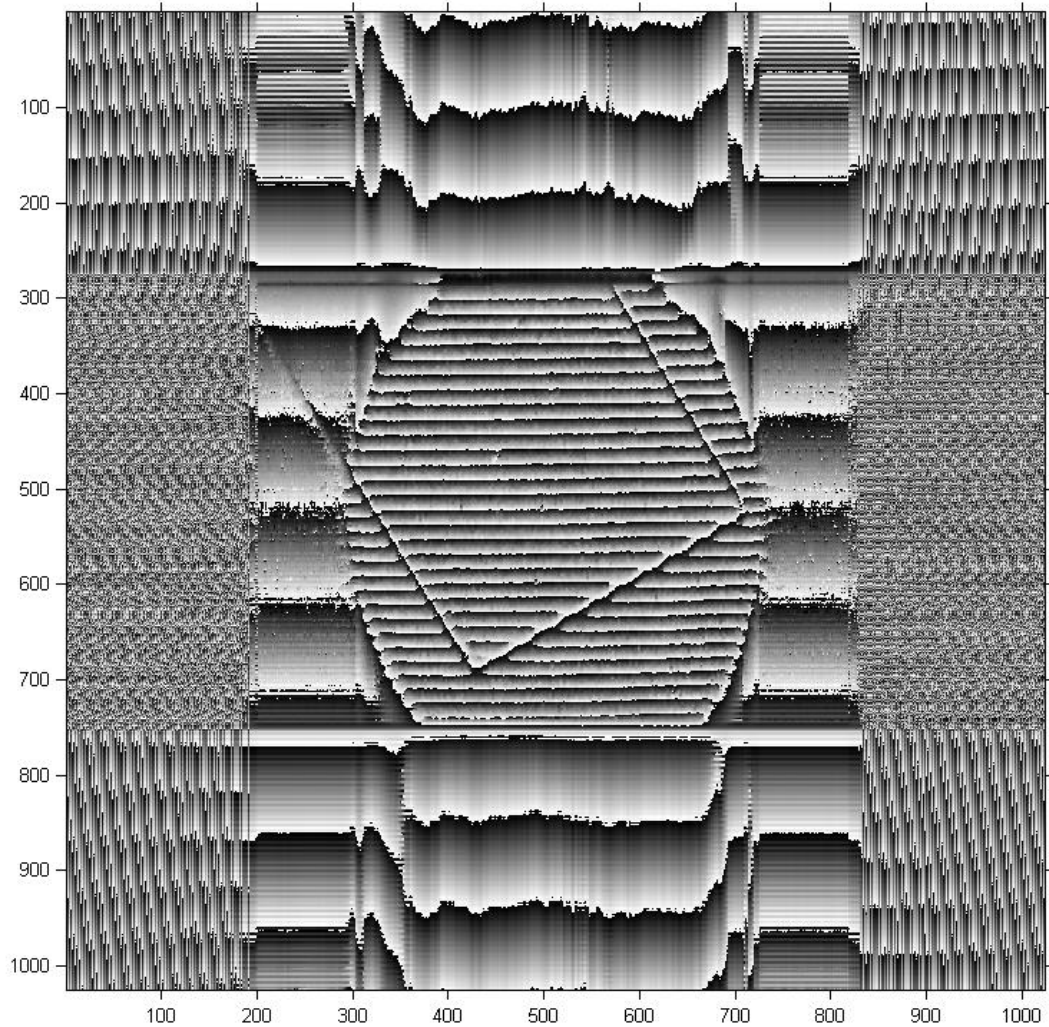


Figure 5-8: Wrapped phase for the glass slide on the copper surface

The next step in the analysis was to subtract the wrapped phase of the reference image (Figure 5-5) from the wrapped phase of the deformed fringe patterns (Figure 5-6 through 5-8) to provide an accurate representation of the shape of the object causing the deformation in the fringes. Finally the phase unwrapping of this subtracted image was done which gave the final surface topology of the object. The images below show the phase unwrapped images

for the above three deformed fringe patterns along with a three dimensional view (both high level and close-up) of the surface topology:

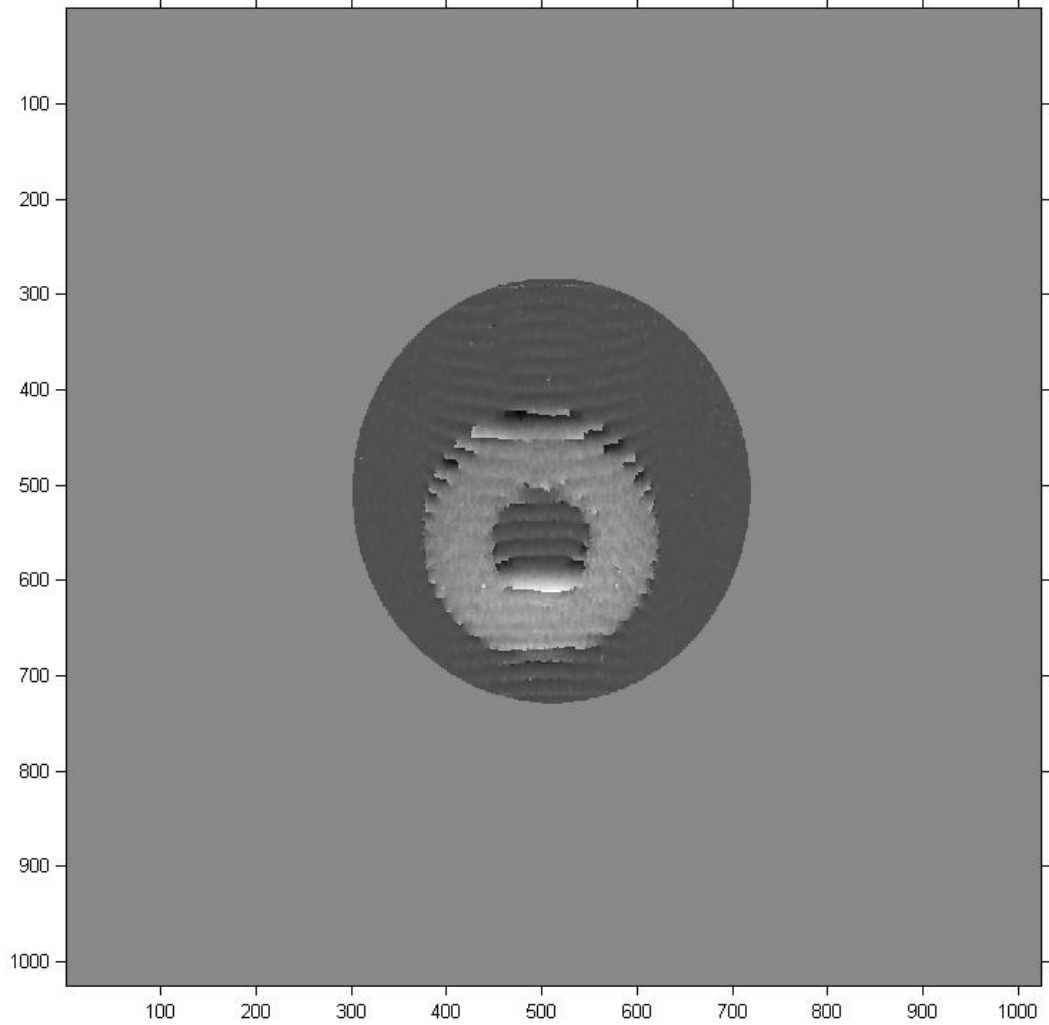


Figure 5-9: Unwrapped phase for the metal washer on the copper surface

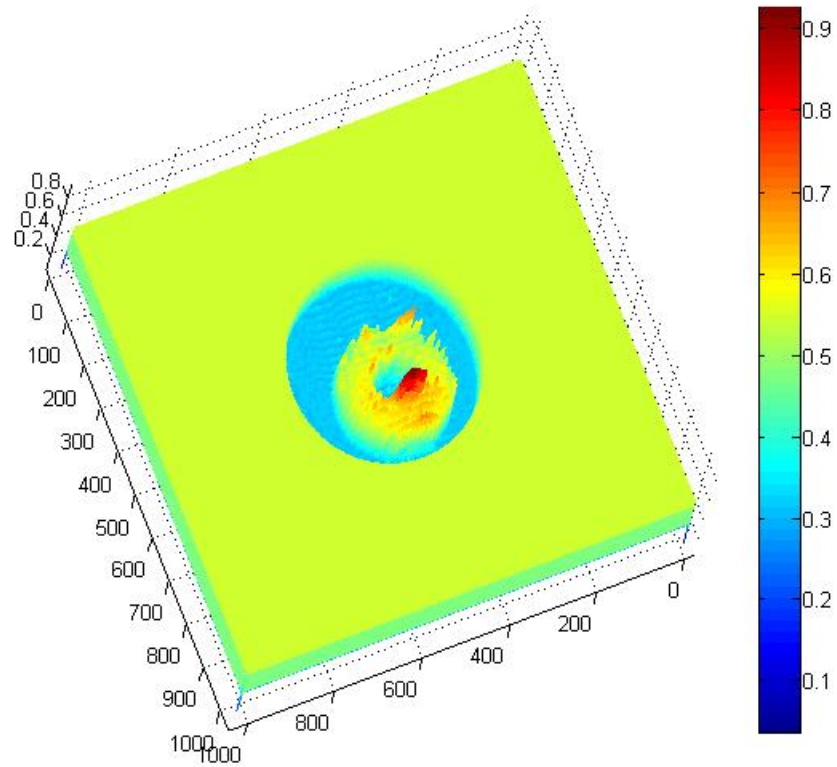


Figure 5-10: Surface topology of the metal washer on the copper surface

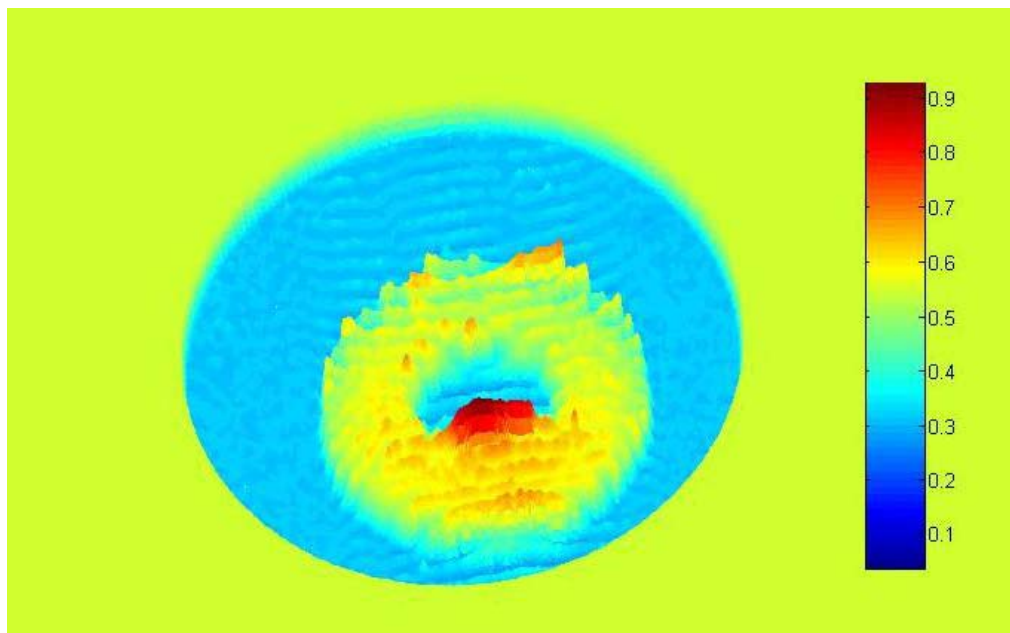


Figure 5-11: Close-up view of surface topology of the metal washer

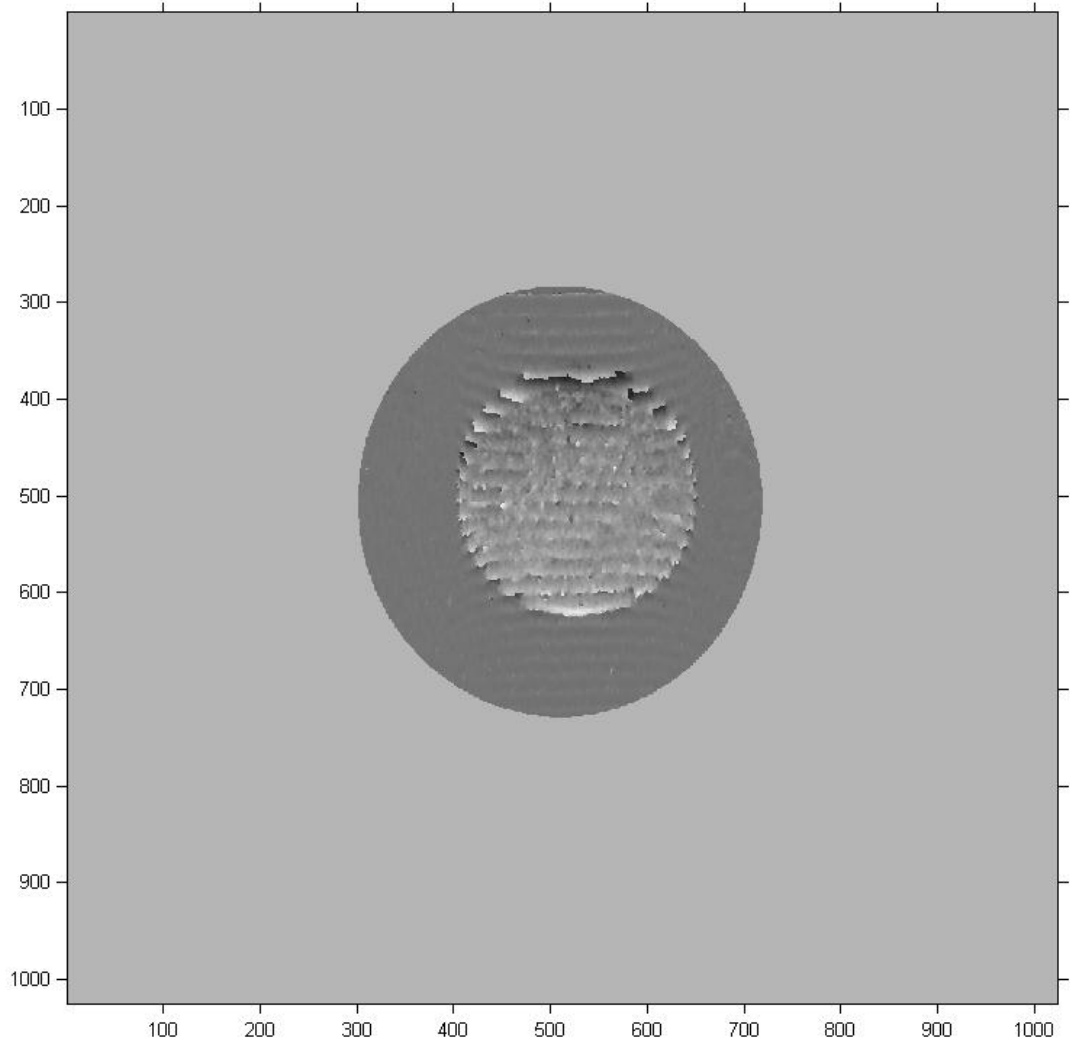


Figure 5-12: Unwrapped phase for the penny on the copper surface

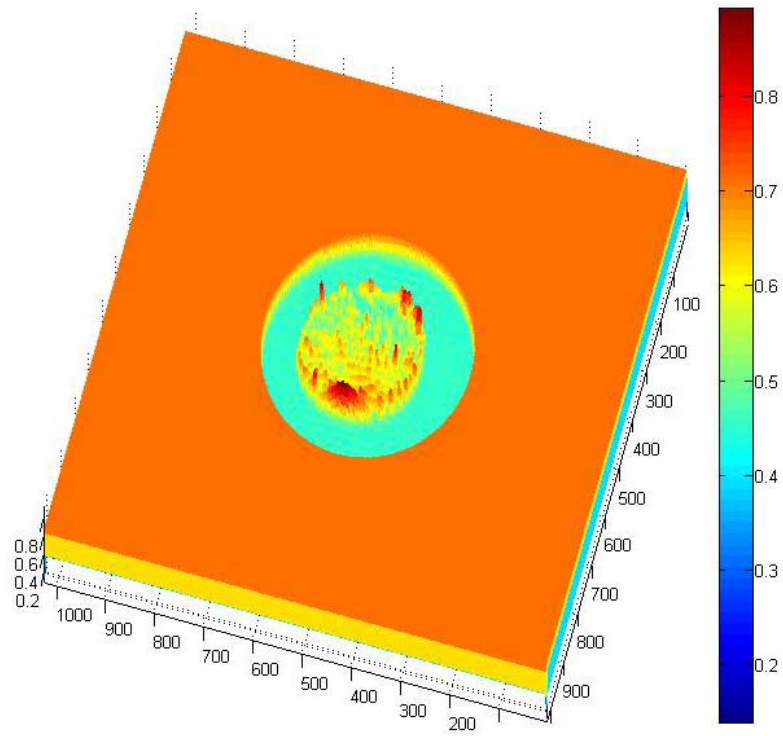


Figure 5-13: Surface topology of the penny on the copper surface

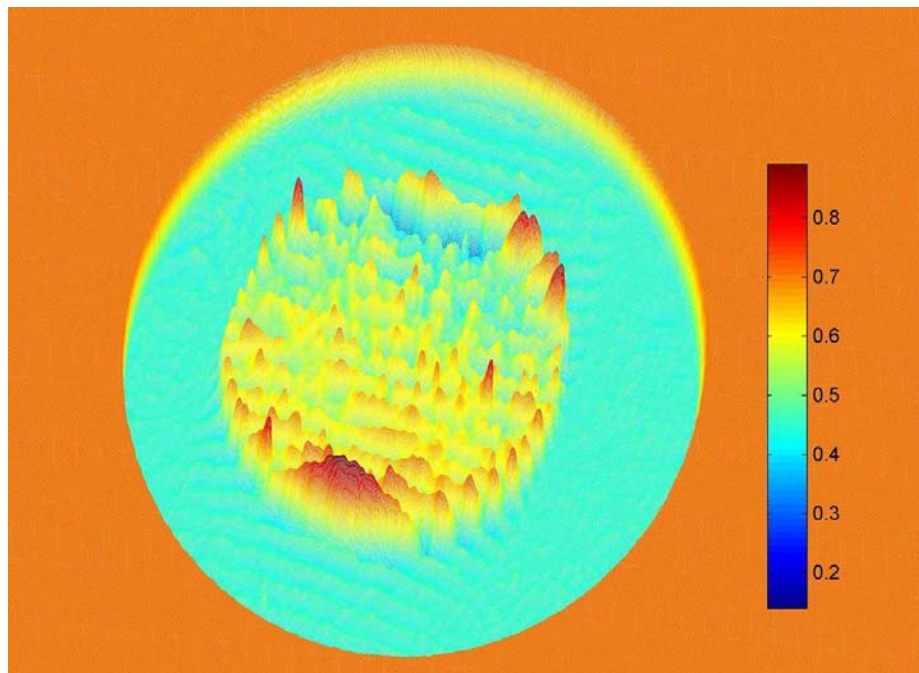


Figure 5-14: Close-up view of surface topology of the penny

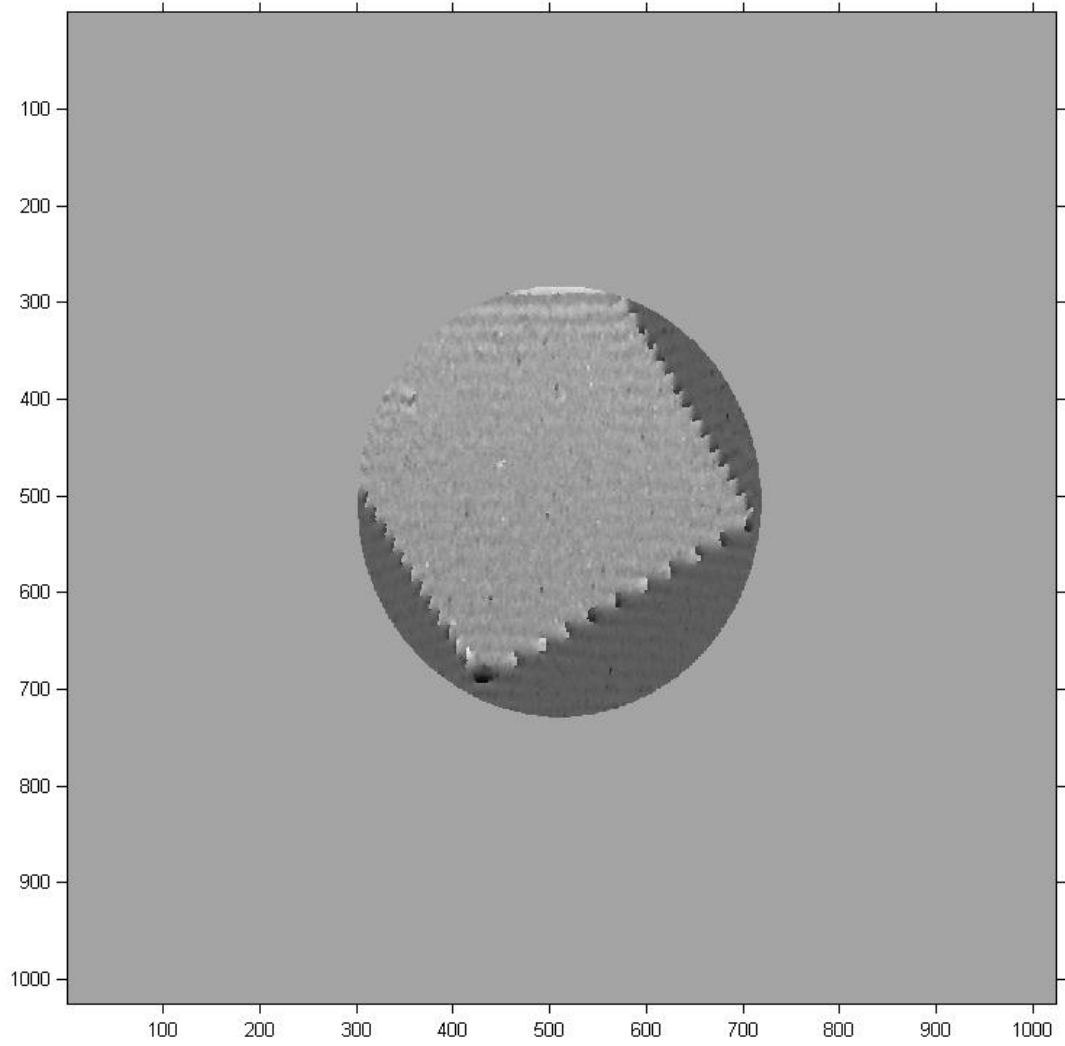


Figure 5-15: Unwrapped phase for the glass slide on the copper surface

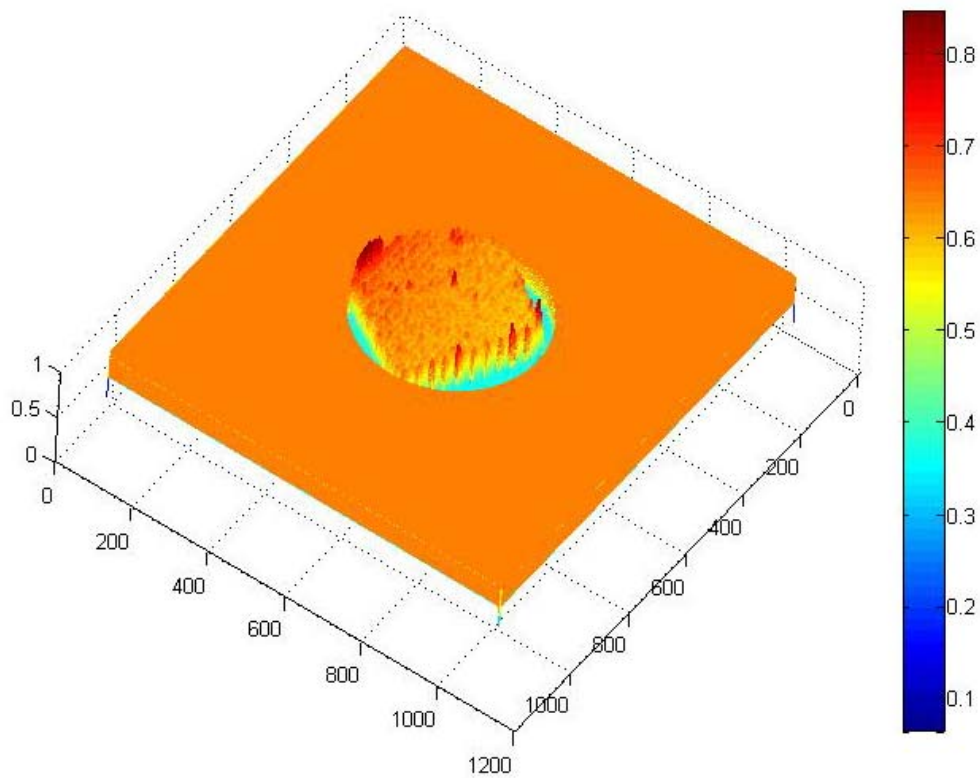


Figure 5-16: Surface topology of the glass slide on the copper surface

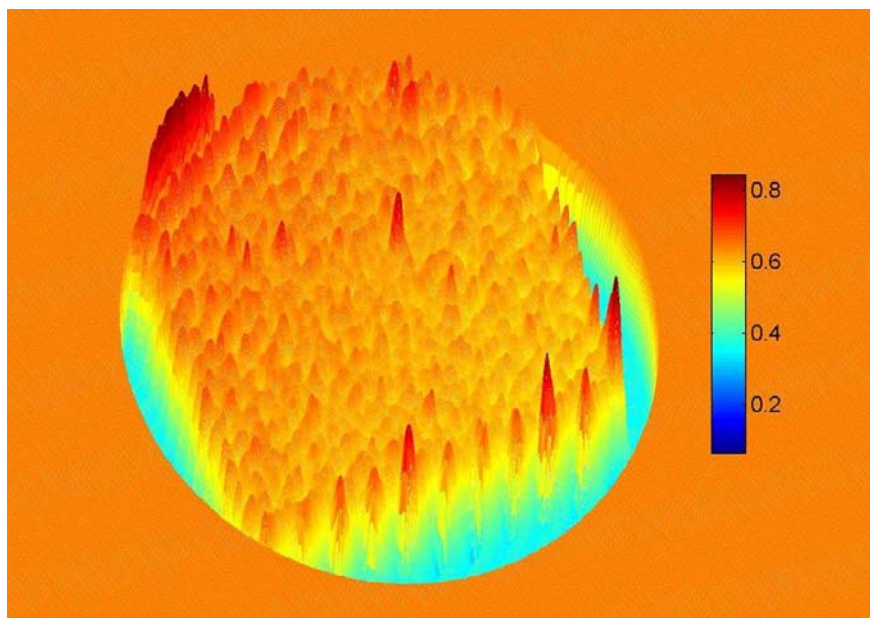


Figure 5-17: Close-up view of surface topology of the glass slide

5.2 Stationary Fluid Experiments

The same set of experiments was repeated by replacing the known objects with droplets of water. Figure 5-18 shows the fringe pattern captured on the reference copper surface. Figure 5-19 shows the fringe pattern deformed by the presence of the water droplet. It is important to capture the reference image right before the capturing the deformed image to ensure that the position of the camera, the fringe density etc. do not change causing errors in our result.

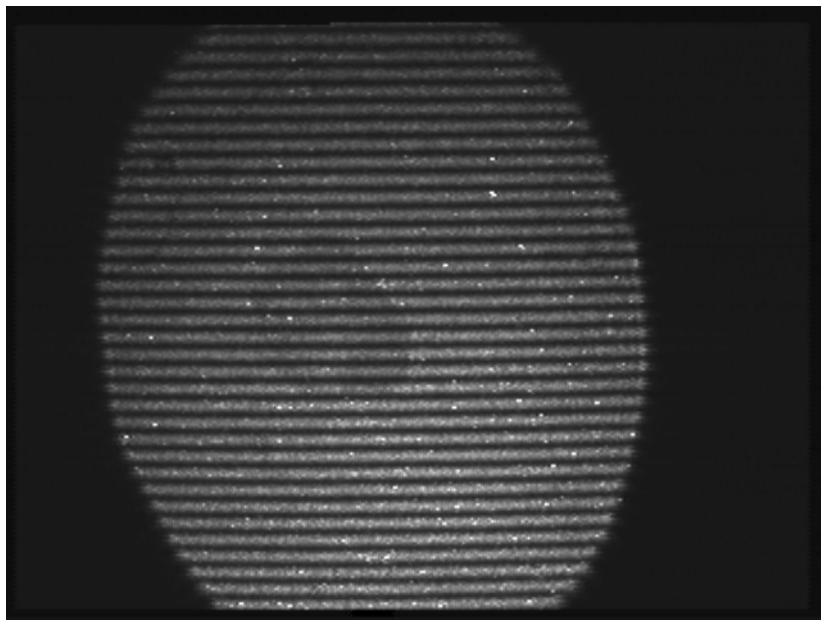


Figure 5-18: Fringe pattern on reference copper surface

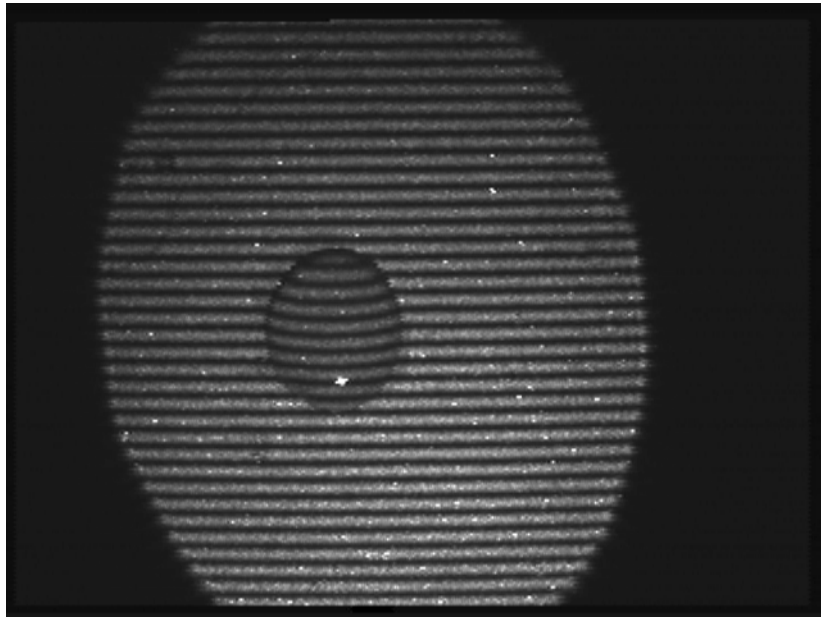


Figure 5-19: Deformed fringe pattern with a water droplet on copper surface

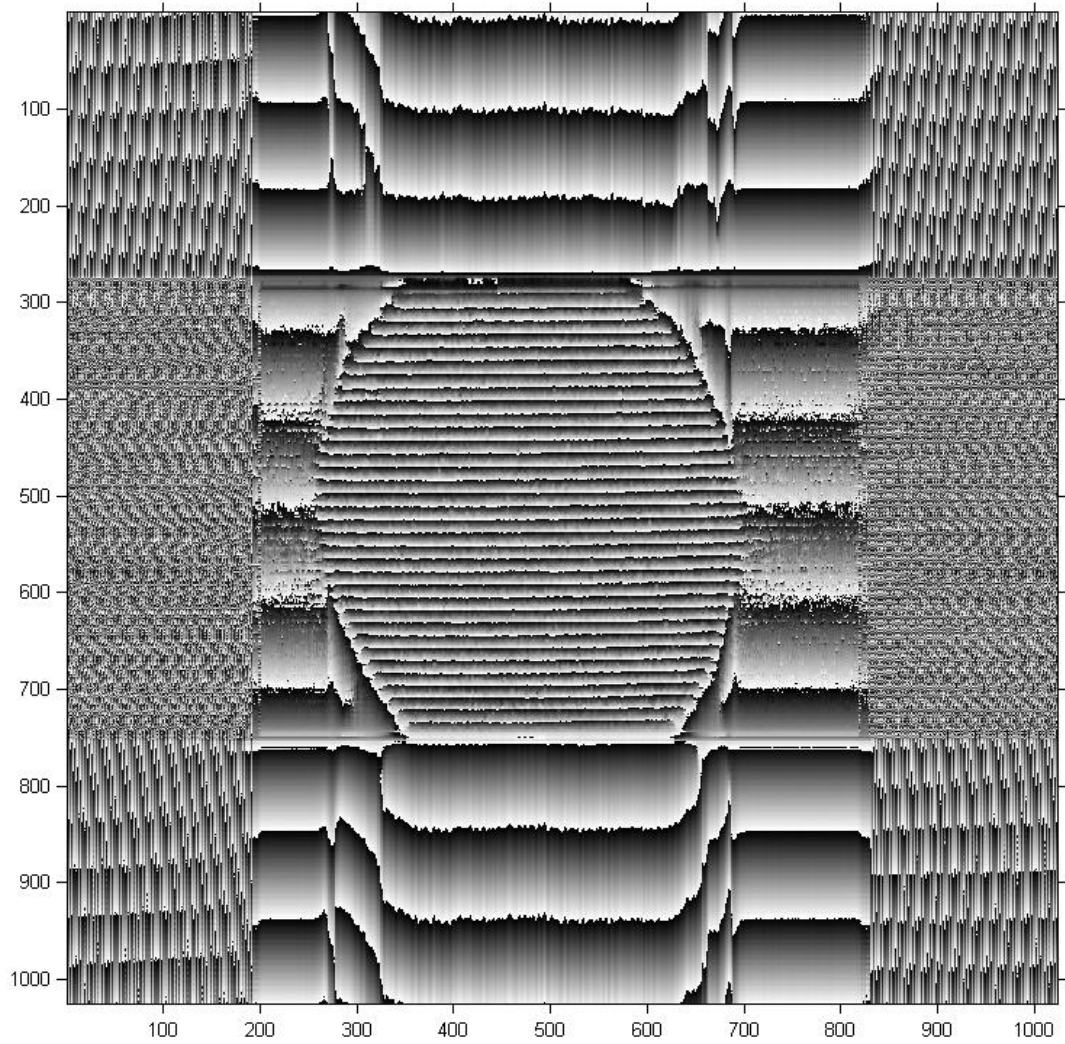


Figure 5-20: Wrapped phase for reference copper surface

Figure 5-20 shows the wrapped phase information for the reference fringe pattern on the copper surface, again generated using the algorithm explained in Chapter 4. Figure 5-21 shows the wrapped phase for the water droplet on the copper plate.

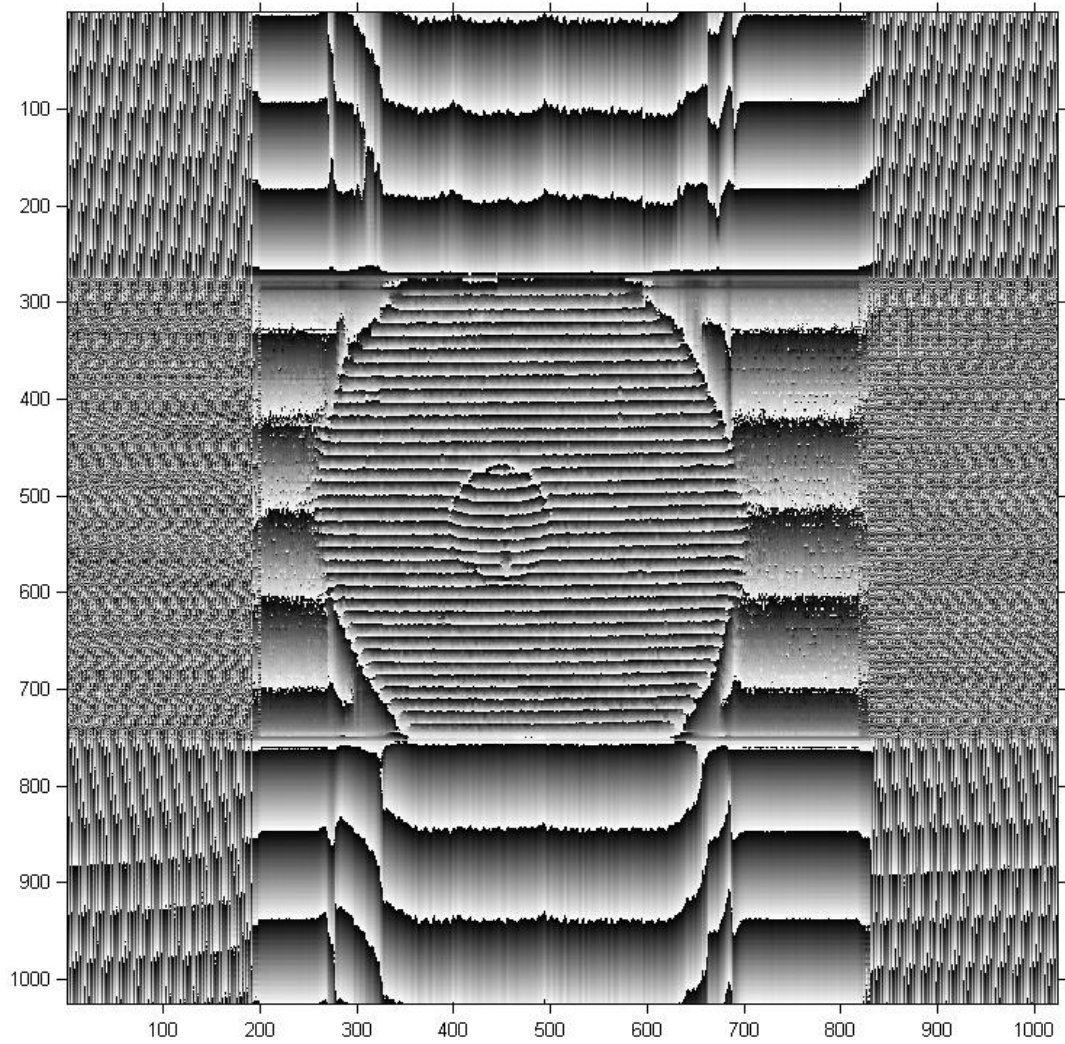


Figure 5-21: Wrapped phase for the water droplet on the copper surface

Finally, subtracting the reference wrapped phase in Figure 5-20 from the wrapped phase in Figure 5-21 with the water droplet information and unwrapping the result yields the unwrapped phase in Figure 5-22.

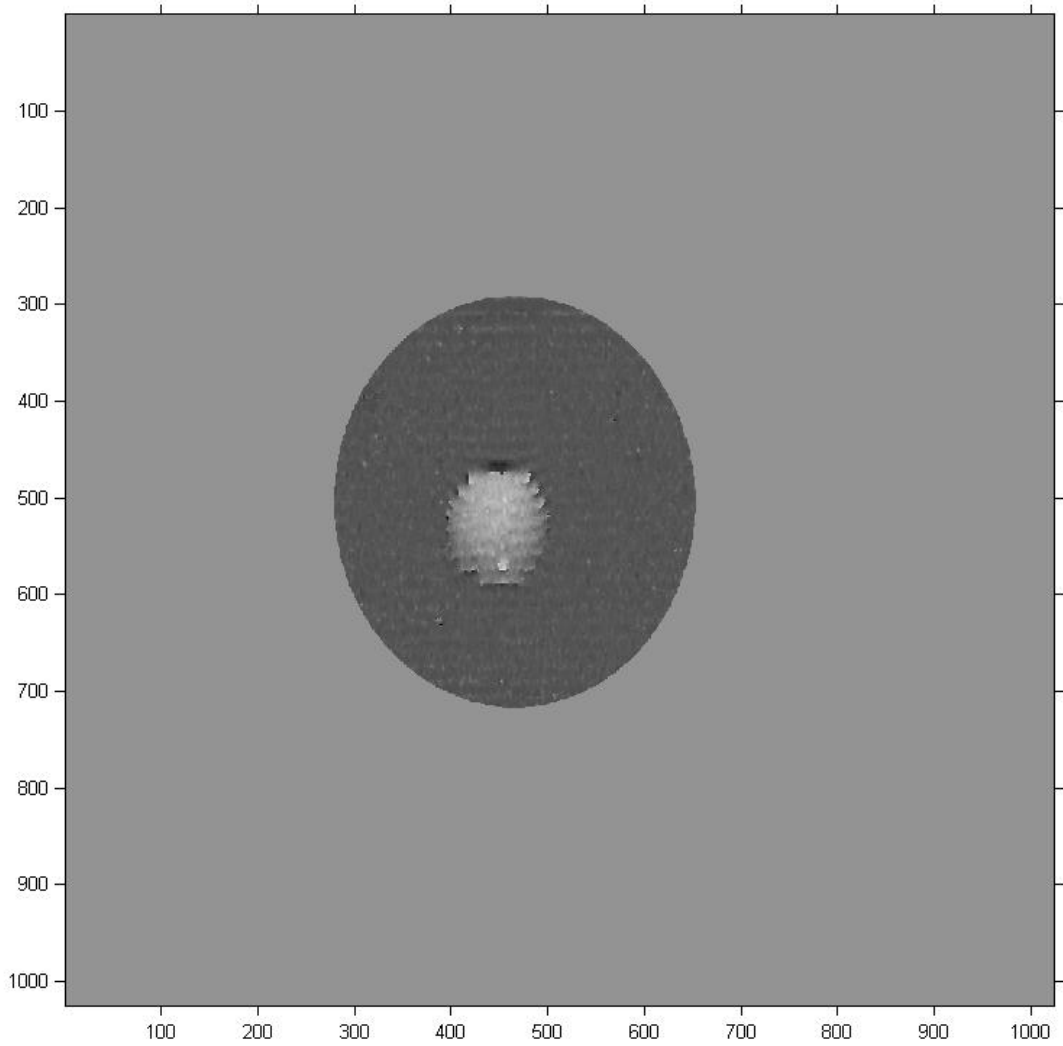


Figure 5-22: Unwrapped phase for the water droplet on the copper surface

Figures 5-23 and 5-24 present a high level and a close-up three dimensional view of the surface topology information in the unwrapped phase image respectively.

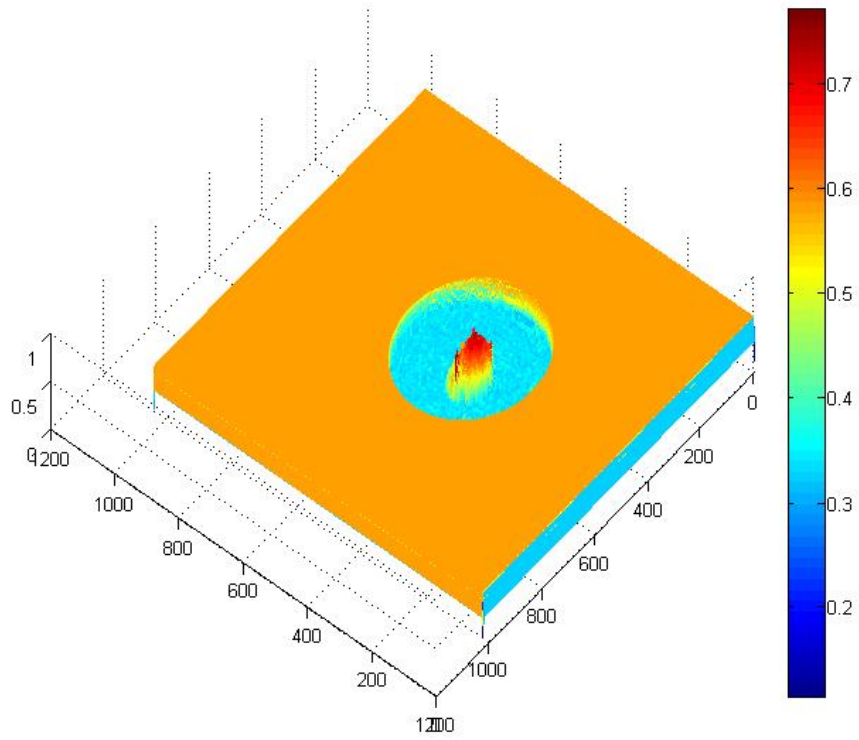


Figure 5-23: Surface topology of the water droplet on the copper surface

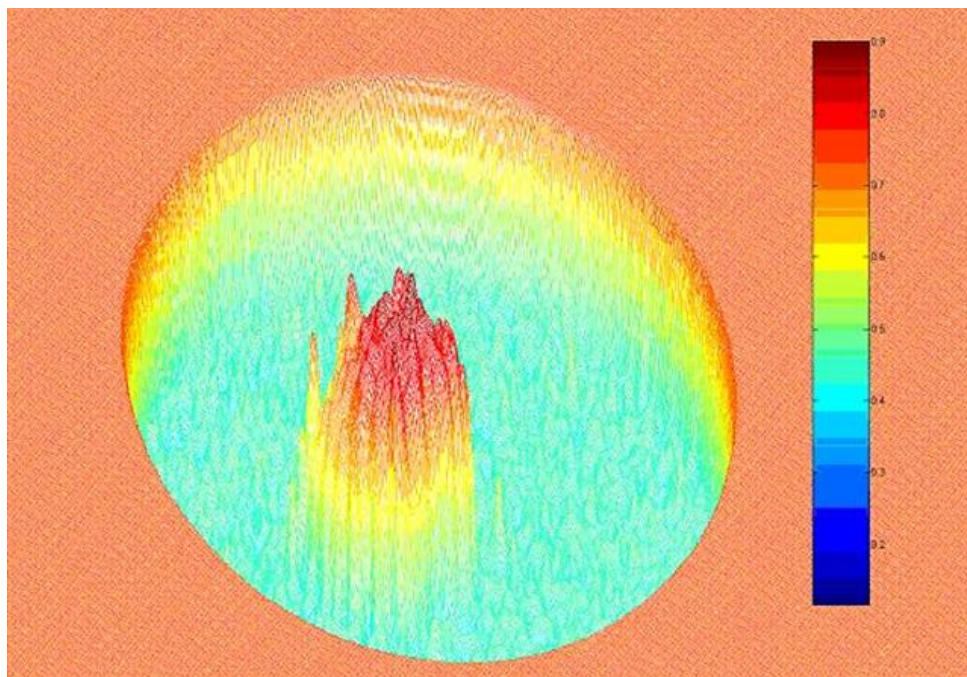


Figure 5-24: Close-up view of surface topology of the water droplet

5.3 Condensation Experiments

The condensation cell was prepared late in the development process of this system. Further, when the cell was integrated with the rest of the optical system, many issues were uncovered which prevented us from obtaining useful data with condensation in progress. There were two problems worth noting:

1. Addition of the condensation cell led to a large amount of distortion in the images.
2. The condensation in the cell led to fogging of the cell itself, blocking the optical path.

These two issues are discussed in additional detail in the following section.

Figure 5-25 below shows two images, one in the absence of the condensation cell and the other in the presence of the cell. It is clear that the presence of the condensation cell leads to distortion in the fringe pattern, most prominent being the vertical stripes.

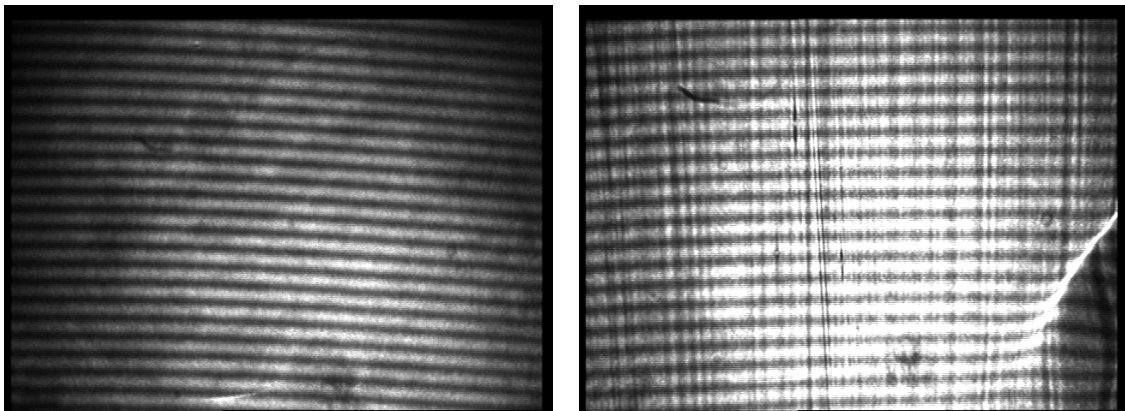


Figure 5-25: Distortion in fringe pattern due to condensation cell

It was believed that the effects of this distortion can be minimized by the use of appropriate filtering techniques. Since majority of the distortion was periodic, this would have required eliminating certain frequency components corresponding to this period. However, the second problem explained below was so significant that we did not reach the stage of testing this hypothesis.

The second significant problem mentioned above was the fogging of the condensation cell. Due to condensation occurring on the walls of the condensation chamber, the optical path was obstructed. Also, condensation on the top of the chamber prevented us from obtaining clear pictures of the condensation process. The problem of condensation on the chamber was anticipated to some extent and measures such as adding heating elements on the chamber walls were taken ahead of time to prevent this problem. However, the heating elements could only be attached so that they did not block the path of the light itself and this proved inadequate in solving this problem. Figure 5-26 provides a close-up view of the condensation chamber with the heating elements, clearly showing the condensation on the chamber walls and ceiling.



Figure 5-26: Condensation on walls and ceiling of the chamber

As a result of the above problem, the attempts at performing condensation experiments were unsuccessful. A few sample pictures acquired in the presence of the condensation cell when condensation was in progress are presented. Figure 5-27 shows a picture during the early stages of the

condensation process, where some visibility is maintained. Figure 5-28 which was obtained only a few seconds later, is barely visible due to fogging up of the cell. (Note: The two images presented below are not original; they have been brightened using image processing techniques for easy viewing)

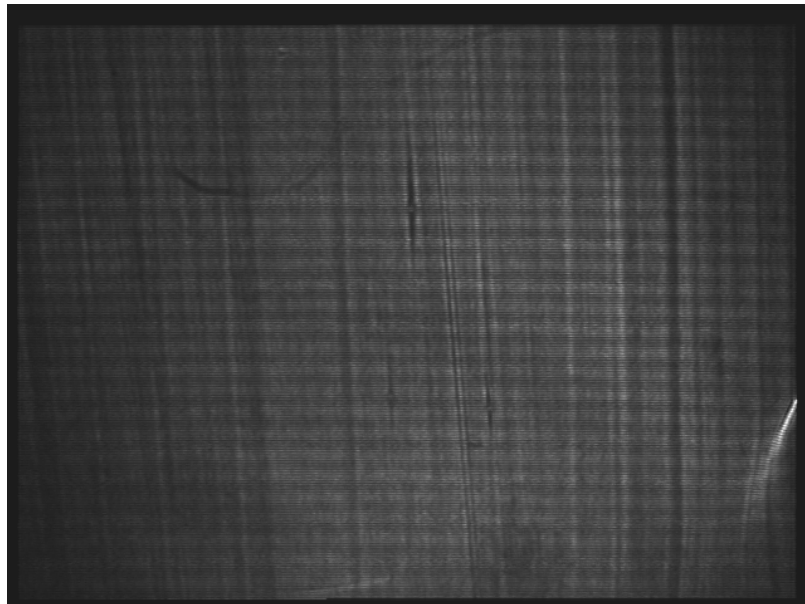


Figure 5-27: Initial snapshot of progressing condensation

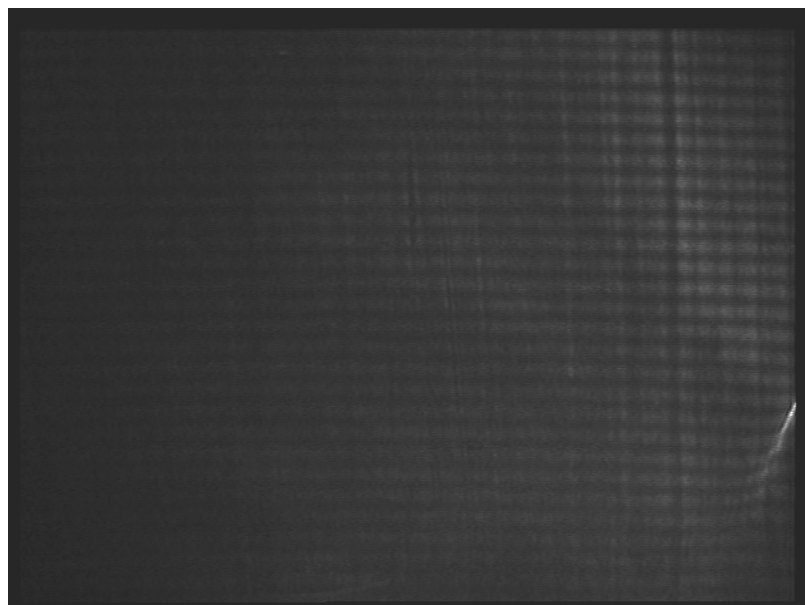


Figure 5-28: Snapshot of condensing film at a later stage

Chapter 6: Conclusion

6.1 Fringe Projection based Measurement System

This thesis has described the various stages through the development of an optical measurement system for characterizing the dynamics of condensation in reduced gravity. A coherent light fringe projection system was implemented which measures the surface topology of water droplets on the test copper surface. Experiments were conducted with this system for the obtaining the surface profile of known objects such as a penny, a metallic washer etc. A simulation of measurement of condensation was achieved by placing a droplet of water on the test surface and its surface map was reconstructed. A condensation cell was also developed and integrated with the optical measurement system. Improvements in the design of the cell which will allow characterization of the process of condensation using the fringe projection system have been proposed as further research.

6.2 Suggestions and Further Work

The optical measurement system will greatly benefit from improvements in the design of the condensation cell, which currently suffers from the problem

of fogging of the condensation cell. It may be possible to either change the material of the cell which may be more thermally conductive, while being optically flat. This will help in heating the cell uniformly to prevent condensation in crucial spots on the chamber walls and ceiling. Another suggestion provided during the thesis defense was the use of transparent electrodes to heat the cell. These would have the advantage of providing the ability to heat the cell as desired without blocking the optical path.

An attempt was made to develop an incoherent light fringe projection system. However, the white light source was found to generate fringe images of an insufficient intensity. Thus the images captured by the camera were barely visible and of very poor contrast. Attempts were made to improve the LED brightness by feeding it at its maximum voltage and current. Also, as the makers of the white light source developed an improved technique for coupling the LED light into the fiber, we sent in the light source for these further improvements. However, these efforts were not adequate in obtaining good quality fringe patterns. One possible technique of obtaining better images was envisioned and could not be implemented due to lack of time. This would require controlling the exposure time of the camera manually. A circuit could be developed which can be potentially be triggered through the laptop's serial port. This circuit in turn would send a trigger pulse to the camera. The width of the pulse would determine the exposure time of the camera. MATLAB scripts can be written to control the output on the serial port programmatically. These scripts can then be integrated with the main data capture software to ensure

that the triggers to the camera, the frame grabber and the temperature measurement system are synchronized.

References

1. Shear M., "Ultrasonic measurement of thin condensing fluid films," M.S. Thesis, Worcester Polytechnic Institute, 2002
2. Novak, J. Techniques for automatic identification and numbering of interference fringes using MATLAB, Civil engineering, CTU Prague
3. Cielo P., Optical techniques for industrial inspection, Academic press Inc., 1988
4. Reid G.T. and Robinson D.W., Interferogram analysis, Institute of Physics Publishing, 1997
5. Wyant J. C., Oreb B. F., and Hariharan P., "Testing aspherics using two-wavelength holography: application of digital electronic techniques," *Applied Optics* 23, 4020, 1984
6. Amidror I., The theory of the Moiré phenomenon, Kluwer Academic Publishers, 1999
7. Gasvik, K.J., Optical Metrology, John Wiley and Sons Ltd., 1987
8. Karaalioglu C and Skarlatos Y, "Fourier transform method for measurement of thin film thickness by speckle interferometry", *Optical Engineering*, 42, 1694-1698, 2003
9. Creath K and Wyant J C, Moiré and fringe projection techniques *Optical Shop Testing*, ed D Malacara (New York: Wiley) pp 653-685, 1992

10. Takeda M., Ina H. and Kobayashi S., "Fourier-transform method of fringe pattern analysis for computer based topography and interferometry", *J. Opt. Soc. Am.* 72 156-160, 1982
11. Saleh and Teich, *Fundamentals of Photonics*, John Wiley and Sons, Inc., New York, 1991

Bibliography

1. Hecht, Optics, Addison-Wesley Publishing Company, 1990
2. Wilson and Hawkes, Optoelectronics-An introduction (2nd edition), Prentice Hall International (UK) Ltd, 1989
3. Tolansky S., An introduction to interferometry (2nd edition), John Wiley and Sons, Inc., New York, 1962
4. Steel, W.H., Interferometry, Cambridge University Press, 1983
5. Candler C., Modern Interferometers, Hilger and Watts Ltd., 1951
6. Born M. and Wolf E., Principles of Optics, Pergamon press, 1980
7. Malacara D., Servin M. and Malacara Z., Interferogram Analysis for Optical Testing, Marcel Dekker Inc., 1998
8. Karaalioglu C. and Skarlatos Y., "Fourier transform method for measurement of thin film thickness by speckle interferometry", *Opt. Eng.* 42 1694-1698. 2003
9. Quan C. et al, "Contour measurement by fiber optic fringe projection and Fourier transform analysis", *Opt. Comm.* 119 479-483, 1995
10. Srinivasan V., Liu H.C. and Halioua M., "Automated phase measuring profilometry of 3-D diffuse objects", *App. Opt.* 23 3105-3108, 1984

11. Massig J.H. and Heppner J., "Fringe-pattern analysis with high accuracy by use of the Fourier-transform method: theory and experimental tests", *App. Opt.* 40 2081-2088, 2001
12. Pedersen P., Cakareski Z. and Hermanson J., "Ultrasonic monitoring of film condensation for applications in reduced gravity," *Ultrasonics* 38 486-490, 2000

Appendix A: Interference Equations

For a plane wave with amplitude \mathbf{U} propagating in the direction of the unit vector \vec{n} , the expression describing the field at an arbitrary point with radius vector $\vec{r} = (x, y, z)$ is given by:

$$\psi(x, y, z, t) = U \cos(k\vec{n} \cdot \vec{r} - 2\pi\nu t + \delta) \quad (\text{A.1})$$

The scalar product fulfilling the condition $\vec{n} \cdot \vec{r} = \text{constant}$ describes a plane which is perpendicular to \vec{n} . Equation A.1 can be rewritten as:

$$\psi(x, y, z, t) = \text{Re}[Ue^{j(\phi - 2\pi\nu t)}] \quad (\text{A.2})$$

where $\phi(x, y, z) = k\vec{n} \cdot \vec{r} + \delta$

In the description of wave phenomena, Eqn. A.2 is frequently used with the reference to 'Re' omitted as it is understood that the field is given by the real part. Thus, on factorizing the spatial and the temporal parts, we get:

$$\begin{aligned} \psi(x, y, z, t) &= U \cdot e^{j\phi(x, y, z)} \cdot e^{-j2\pi\nu t} \\ &= U(x, y, z) \cdot e^{-j2\pi\nu t} \end{aligned}$$

where $U(x, y, z)$ is the complex amplitude of the wave.

In optical metrology applications, one is most often interested in the spatial distribution of the field. Since the time dependent part is known for each

frequency component, we can therefore omit the term $e^{-j2\pi vt}$ of the above equation, yielding:

$$\psi = U(x, y, z) = U \cdot e^{j\phi(x, y, z)} \quad (\text{A.3})$$

Consider a plane wave falling obliquely on to a plane parallel to the x-y plane a distance z from it. The wave propagates along the unit vector \vec{n} which is lying in the xz –plane (defined as plane of incidence) and makes an angle θ to the z axis. The components of the \vec{n} and \vec{r} vectors are

$$\vec{n} = (\sin \theta, 0, \cos \theta)$$

$$\vec{r} = (x, y, z)$$

Thus,

$$\begin{aligned} \phi(x, y, z) &= k\vec{n} \cdot \vec{r} + \delta \\ &= k(x \sin(\theta) + z \cos(\theta)) + \delta \end{aligned}$$

Substituting in Eqn. A.3 (and omitting the phase difference δ), we get

$$\psi = U \cdot e^{jk(x \cdot \sin(\theta) + z \cdot \cos(\theta))} \quad (\text{A.4})$$

With the above knowledge of oblique incidence of a plane wave, we present an in-depth version of the analysis given in Chapter 2 (section 2.4.1). Consider two plane waves U_1, U_2 with propagation vectors \vec{n}_1, \vec{n}_2 that lie in xz plane making angles θ_1, θ_2 to the z axis.

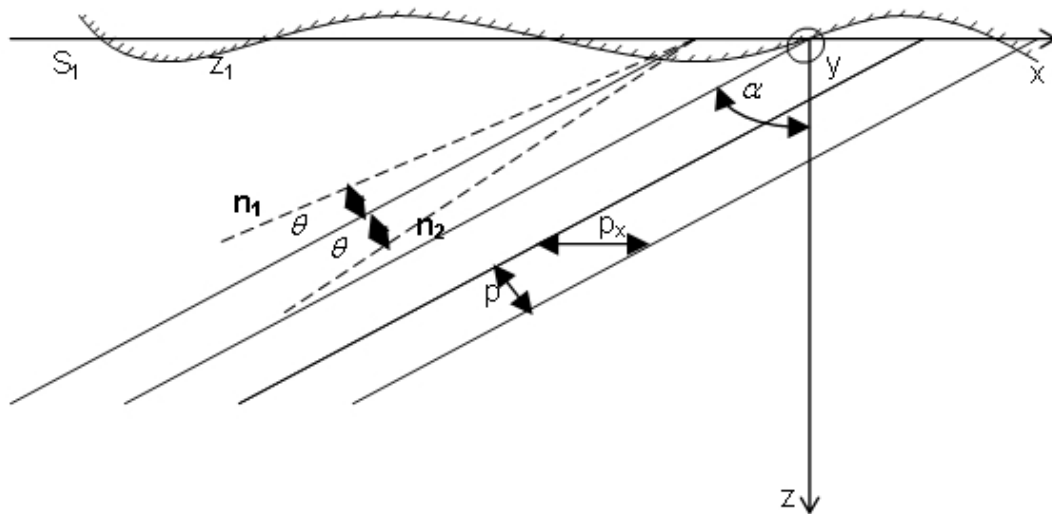


Figure A-1: Analysis of fringes with fringe spacing p projected at an angle α on the surface under test

We introduce the following quantities:

$$2\theta = \text{angle between } \vec{n}_1 \text{ and } \vec{n}_2$$

$$\alpha = \text{angle between the } z \text{ axis and the line bisecting } 2\theta$$

Thus, the two waves are described as:

$$U_1 = a_1 \cdot e^{j\phi_1}$$

$$U_2 = a_2 \cdot e^{j\phi_2}$$

where $\phi_1 = k[x \sin(\alpha - \theta) + z \cos(\alpha - \theta)]$

$$\phi_2 = k[x \sin(\alpha + \theta) + z \cos(\alpha + \theta)]$$

Now, $\Delta\phi = \phi_1 - \phi_2$

$$= 2k \sin(\theta)(-x \cos(\alpha) + z \sin(\alpha))$$

We know that the intensity of interference beam is

$$\begin{aligned}
 I &= I_1 + I_2 + 2\sqrt{I_1 I_2} \cos \Delta\phi \\
 &= I_1 + I_2 + 2\sqrt{I_1 I_2} \cos \left[2 \cdot \frac{2\pi}{\lambda} \cdot \sin \theta (z \sin(\alpha) - x \cos(\alpha)) \right]
 \end{aligned}$$

The interference term is of the form

$$\cos \left[\frac{2\pi}{p} \cdot (z \sin(\alpha) - x \cos(\alpha)) \right] \quad (A.5)$$

where $p = \frac{\lambda}{2 \sin(\theta)}$

Substituting above value of p , and assuming intensities of the two interfering beams to be equal (say I_0), we obtain Eqn. A.6 below:

$$I = I_0 \left[1 + 2 \cos \left[\frac{2\pi}{p} (z \sin(\alpha) - x \cos(\alpha)) \right] \right] \quad (A.6)$$

Comparing the interference term with the real part of Eqn A.4, we see that Eqn A.6 can be seen as representing a plane wave with its propagation direction in the xy plane making an angle α with x axis and with a wavelength p . Eqn A.6 is essentially same as the interference Eqn 2.18. Further, it should be noted that the distance between the interference fringes (i.e. the wavelength p) is only dependent on the angle between \vec{n}_1 and \vec{n}_2 . As θ increases, p decreases.

Appendix B: Assembly of the System

This appendix attempts to describe the process of assembling the system. The entire optical system is placed on an optical base plate. All the components are securely attached to this plate. This is useful in minimizing the effects of vibration on the system. By having a common base plate, vibration affects all parts of the system equally, thus having a less detrimental effect. Figure B-1 shows a picture of the base plate which has dimensions 12x12 in. and thickness 0.5 in.



Figure B-1: Optical Base Plate

The laser and the collimator are mounted on their individual mounts which in turn are mounted together on an aluminum plate held up on the base

plate with the help of posts and post holders. Figure B-2 shows a close up view of this mounting arrangement.

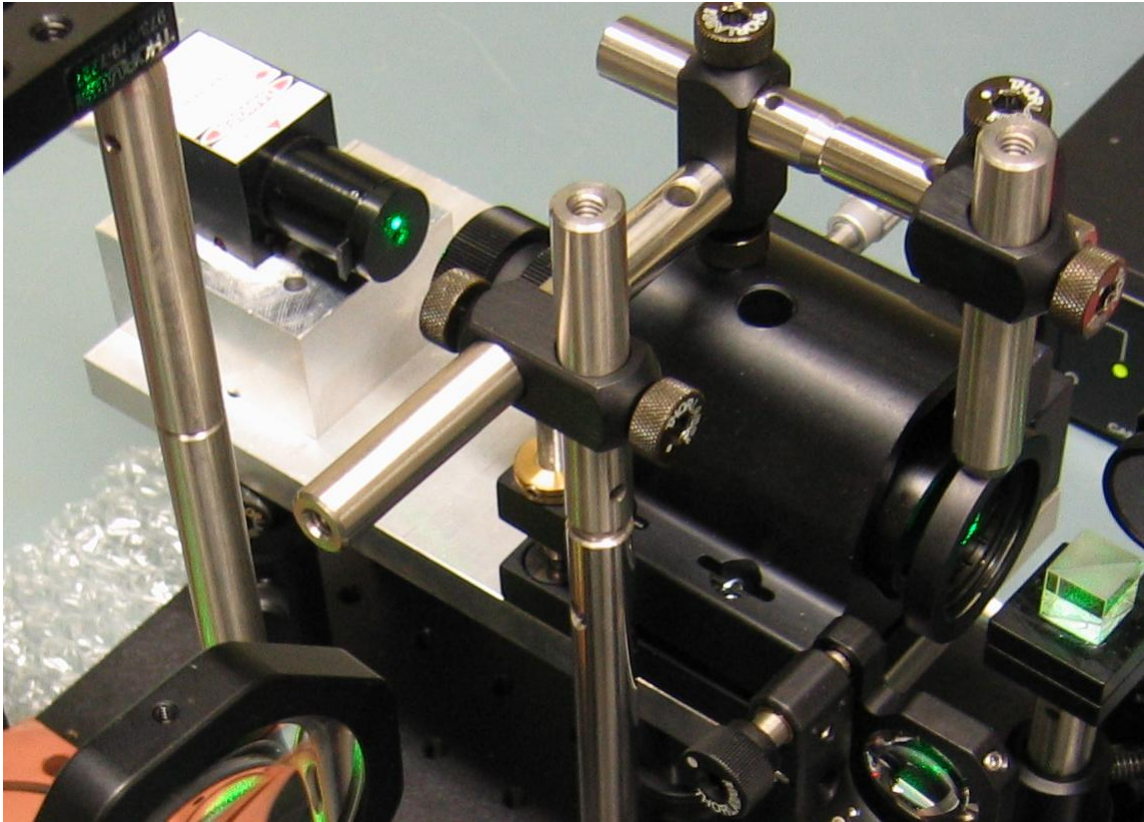


Figure B-2: Laser and Collimator Mounting Arrangement

The laser mount was a custom designed aluminum block, which takes advantage of the mounting holes provided at the bottom of the laser while simultaneously acting as a heat sink to dissipate the heat generated from the laser. A layer of thermal heat sink compound at the interface of the laser and the laser mount assists in the heat dissipation. The collimator mount is model ULM-TILT, which provides two axes of precision angular adjustment using a stable kinematic three-point design for drift-free pointing of the collimator head.

We use the mounting holes on this mount to attach it to the aluminum mounting plate for the laser and the collimator assembly. Figure B-3 shows a picture of the collimator mount:



Figure B-3: Collimator Mount

Before moving on to describe the next set of components, here are some general tips on alignment of the laser and the collimator. It is useful to first fix the laser in place and observe the beam at two points, one close to the laser and the other farther away. The two points should be at the same height from the ground to make sure that the laser is not introducing any tilt in the optical axis. At this point the collimator should not be present in the system. Then, insert an iris in the path of the beam close to the laser. Place the iris so that the beam is centered through the iris. Observe the location of the beam passing through the iris and falling at a point far away. Mark this point. Later insert the collimator and use the previously marked point as a reference for alignment.

The goal of alignment is that the collimator should add no (or minimal) tilt in the direction of the beam.

The next set of components is mounted on an optical rail. This includes the Michelson interferometer arrangement (beam splitter and two mirrors) and the first lens of the beam expander. The optical rail was chosen for placing these components as it was the best way to obtain precise placement and movement of the mirrors for alignment of the interferometer (since the optical base plate only has mounting holes on a 25mm grid). Also, it was found very useful in obtaining the right amount of expansion in the beam by movement of the beam expansion mirror. The posts holding the mirrors, beam splitter and the beam expansion lens are mounted on movable rail carriers which are then mounted on the optical rail as shown in Figure B-4.

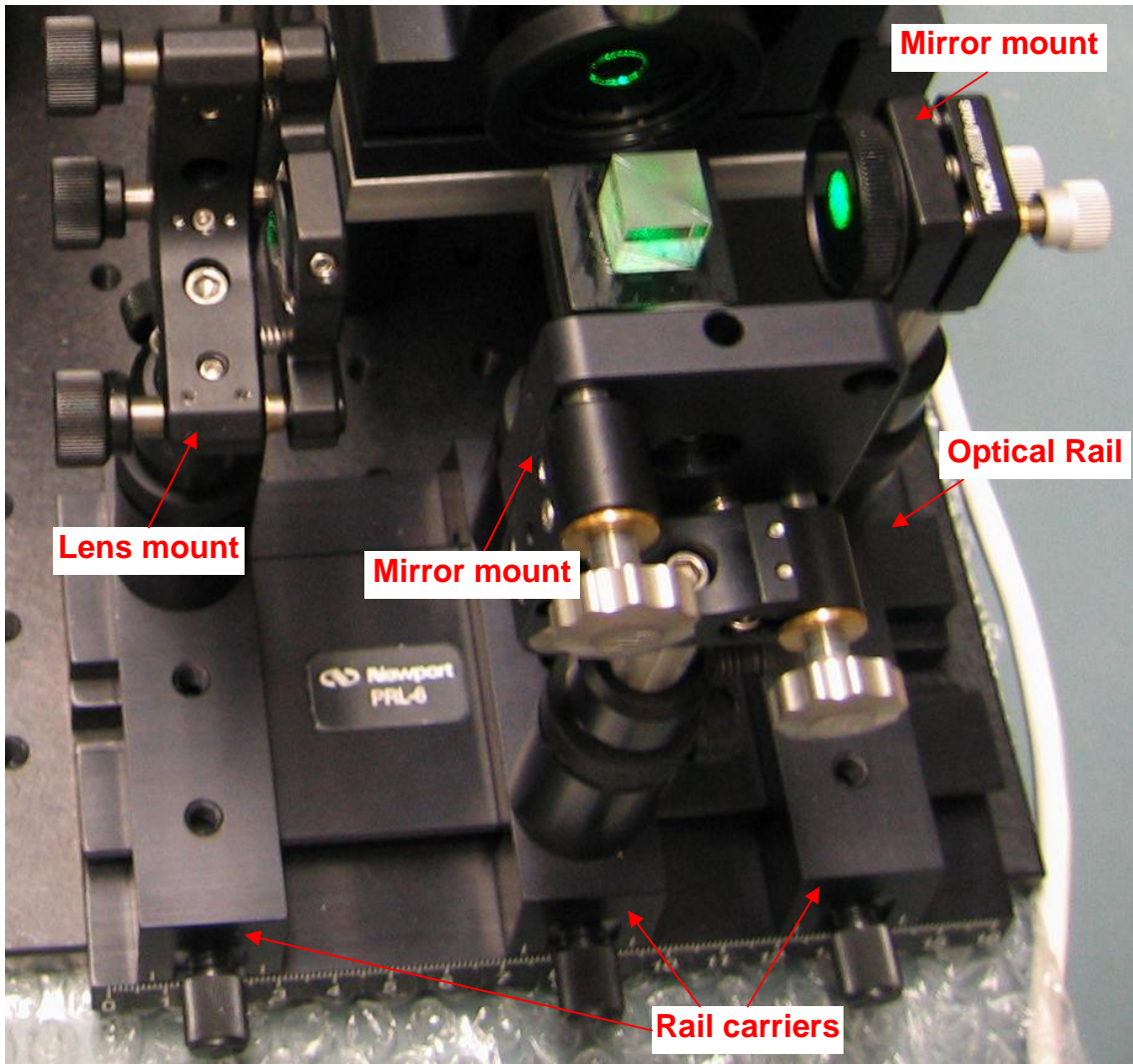


Figure B-4: Optical Rail Assembly

Following the first beam expansion mirror, mounted on the optical rail assembly, is the beam steering mirror and the second lens of the beam expansion system. The need for the beam steering mirror arose from the design decision of limiting the system to the optical base plate of dimensions 12x12 in (which was important in achieving easy portability of the system). Hence, to fit all the components on the system, while providing sufficient distance between

the two beam expansion lenses (in order to obtain the right amount of expansion), the beam steering mirror was introduced. Both the beam steering mirror and the second lens are mounted on mirror mounts, which are held on the base plate on posts in post holders. Figure B-5 shows a picture of these components.

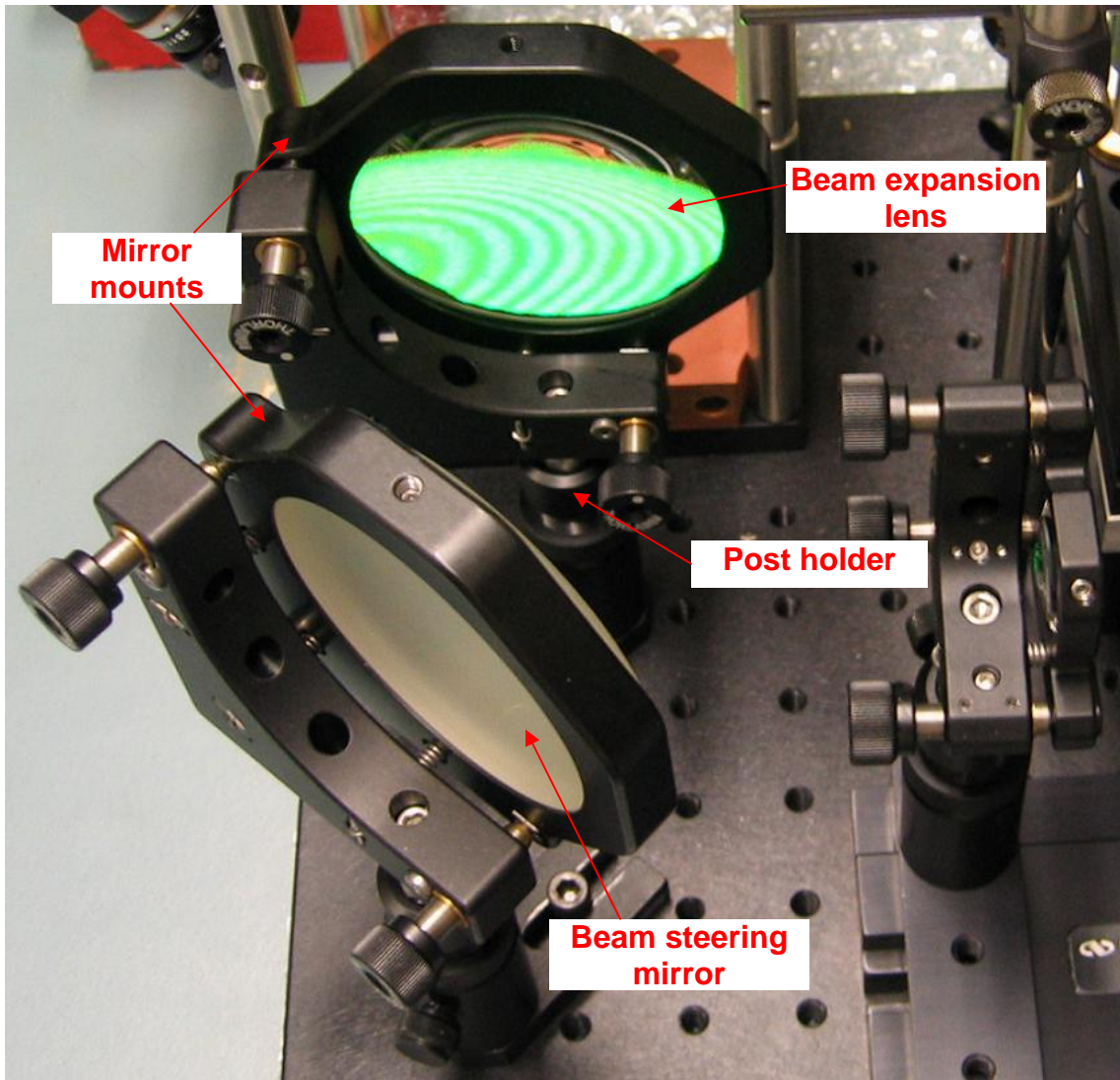


Figure B-5: Beam Steering and Expansion Optics

The beam expansion arrangement is followed by another beam steering mirror used to project the fringe pattern onto the copper block. The entire assembly of the beam steering mirror and the copper block is built on a modular riser plate of dimensions 3"x3" and height 0.5". The riser plate serves to raise the height of the arrangement while providing a way to securely mount this assembly on the optical base plate. The copper block is attached to the riser plate using screws. The condensation cell fits tightly into the groove on the copper block. On the four corners of the riser plate, four posts are attached. These posts are helpful in mounting of the angle mount which holds the beam steering mirror. The design of the angle mount allows for easy vertical movement on the posts for fine optical alignment.

These posts are also used for the mounting of the camera. Using a series of posts and angle clamps and the custom designed camera mount, the camera is mounted over the condensation cell, without blocking the path of light. Figure B-6 shows a close up view of this section of the optical system.



Figure B-6: Condensation cell assembly

The heating elements on the condensation cell are all connected in parallel and then connected to the Variac which is capable of providing variable voltage ranging from 0-140V. Typically a voltage of about 80V is applied to the heating elements.



Figure B-7: Variable Voltage Control

With all the components of the system in place, the system must be started as explained below:

- 1) Turn on the hot plate first. Increase the heating up to maximum value to get the water boiling. Do not cork it initially as it may lead to fogging up of the condensation cell. Once the water is boiling, reduce the temperature to about 300-400°C.
- 2) Turn on Variac connected to the heating elements and get the chamber heated.
- 3) Put ice and water in the white plastic box and start the water pump. Initially, it may have trouble with the flow due to air bubbles, but press the pipe near the inlet and outlet to get that going. Use the strainer near the outlet to prevent the ice from clogging up the outlet.
- 4) Finally, cork the boiling water container once the chamber has got heated up.
- 5) The vapor inlet pipe has an additional outlet to take care of the water condensed along the pipe. This outlet should stay as the lowest point of the system, so that the water flows out into the beaker placed on the ground.

Appendix C: MATLAB code

FCap.m

```
close all;
clear all;

% Create GUI figure frame
fig=figure('Units', 'pixels',...
           'Position', [200 200 1100 610]);
set(fig, 'Colormap', gray);

% Display blank placeholder image on GUI
axMain = axes('Units', 'pixels',...
              'Position', [0 0 700 610]);
imgMain = image(zeros(480,640));
set(get(imgMain, 'parent'), 'Units', 'normalized',...
     'Position', [.025, .1, .6, .88],...
     'Visible', 'off' );

xoff=20;
xact=640;
yoff=20;
yact=480;
axMain = updateMain(axMain, xoff, xact, yoff, yact, 0);

% Layout buttons on GUI
leftButton = uicontrol( 'Style', 'pushbutton',...
                        'Units', 'normalized',...
                        'Position', [.025, .025, .185, .05],...
                        'String', '<--- Left --->',...
                        'Callback', ...
                        ['xoff = xoff-15;', ...
                        'if xoff < 0 xoff=0; end;',...
                        'if xoff > 140 xoff=135; end;', ...
                        'axMain = updateMain(axMain, xoff, xact, yoff,
yact, 0);']);

updateButton = uicontrol( 'Style', 'pushbutton',...
                           'Units', 'normalized',...
                           'Position', [.22, .025, .21, .05],...
                           'String', 'Update',...
                           'Callback', ...
                           'axMain = updateMain(axMain, xoff, xact,
yoff, yact, 0);');

rightButton = uicontrol( 'Style', 'pushbutton',...
                          'Units', 'normalized',...
```

```

        'Position', [.440, .025, .185, .05],...
        'String', '---- Right ---->',...
        'Callback', ...
        ['xoff = xoff+15; ',...
        'if xoff < 0 xoff=0; end;',...
        'if xoff > 140 xoff=135; end;',...
        'axMain = updateMain(axMain, xoff, xact,
yoff, yact, 0);']]);

movieButton = uicontrol( 'Style', 'pushbutton',...
        'Units', 'normalized',...
        'Position', [.65, .025, .185, .05],...
        'String', 'Movie!',...
        'Callback', ...
        ['start(Tc); ',...
        'set(Ts, ''StartDelay'',
str2double(get(frameCount, ''String'')));',...
        'start(Tr); start(Ts);']]);

frameCount= uicontrol( 'Style', 'edit',...
        'Units', 'normalized',...
        'Position', [.845, .025, .08, .05],...
        'String', 'Duration');

% Create plot for display of temperature data

data(1,:)= [0 0 0];
data(2,:)= [0 0 0];
data(3,:)= [0 0 0];

tAx = axes('Units', 'normalized', 'Position', [.67, .5, .32, .48]);
plot(1:length(data(1,:)), data(1,:),1:length(data(1,:)),
data(2,:),1:length(data(1,:)), data(3,:));

% Initialize access codes for temperature sensors
copper_block_ID= uint16([40 203 58 105 0 0 0 67]);
vapor_out_ID = uint16([40 212 21 105 0 0 0 171]);
vapor_in_ID = uint16([40 140 80 105 0 0 0 31]);

% Frame number
t=1;

% Create 2 timer objects with timer functions that capture image and
% temperature data
Tc = timer('TimerFcn', ...
        'getTemps(0,0); updatemain(axMain,xoff, xact, yoff, yact, t);',
        ...
        'Period', 1.5, 'ExecutionMode', 'fixedrate');

Tr = timer('TimerFcn', ...
        ['copper_block(t) = getTemps(1,copper_block_ID);',...
        'vapor_out(t) = getTemps(1,vapor_out_ID); ',...
        'vapor_in(t) = getTemps(1,vapor_in_ID);',...
        'axes(tAx);',...

```

```

    'tP=plot(1:1.5:t*1.5, copper_block(1:t),1:1.5:t*1.5,
vapor_out(1:t), 1:1.5:t*1.5, vapor_in(1:t), 'LineWidth' , 2);', ...
    'axis([1 1.5*t 0 100]);',...
    'set(tP, 'Parent', tAx);',...
    't=t+1;',...
    'leg = legend('Copper Block', 'Vapor Outlet', 'Vapor
Inlet', 0); '], ...
    'Period', 1.5, ...
    'ExecutionMode', 'fixedrate', 'StartDelay', .75);

% Create third timer that stops the above two timers
Ts = timer('TimerFcn', 'stop(Tc); stop(Tr);', ...
    'Period', 0.1, 'ExecutionMode', 'singleshot');
set(tAx, 'FontSize', 8);

```

UpdateMain.m

```

function axMain = UpdateMain(axMain, xoff, xact, yoff, yact, f)

% Grab input parameters for image capture
xoffset=xoff;
yoffset=yoff;
xactive=xact;
yactive=yact;

axes(axMain);

B=mextest2(1,[xoffset,xactive,640,yoffset,yactive,480], f)';

new=zeros(3,480,640);
new(1,:,:)=(reshape(B(1:3:640*480*3),640,480))';

bitmap=squeeze(sum(new,1));
imgMain=imagesc(bitmap, [0 255]);

set(imgMain, 'Parent', axMain);
set(axMain, 'Visible', 'off');

imwrite(bitmap/255,['.\frames\frame', int2str(f), '.bmp'], 'bmp');
return

```